

AD-A266 079



2

RL-TR-93-19
Final Technical Report
March 1993



DESIGN AND ANALYSIS OF AN OPTICAL INTERFACE MESSAGE PROCESSOR

Syracuse University

Dr. Q. Wang Song

DTIC
SELECTED
JUN 23 1993
S B D

APPROVED FOR PUBLIC RELEASE; DISTRIBUTION UNLIMITED.

98 6 22 065

93-14035



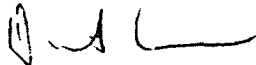
16076

Rome Laboratory
Air Force Materiel Command
Griffiss Air Force Base, New York

This report has been reviewed by the Rome Laboratory Public Affairs Office (PA) and is releasable to the National Technical Information Service (NTIS). At NTIS it will be releasable to the general public, including foreign nations.

RL-TR-93-19 has been reviewed and is approved for publication.

APPROVED:



DAVID A. CORDEIRO
Project Engineer

FOR THE COMMANDER:



JOHN A. GRANIERO
Chief Scientist
Command, Control and Communications Directorate

If your address has changed or if you wish to be removed from the Rome Laboratory mailing list, or if the addressee is no longer employed by your organization, please notify RL(C3DB) Griffiss AFB, NY 13441-4505 This will assist us in maintaining a current mailing list.

Do not return copies of this report unless contractual obligations or notices on a specific document require that it be returned.

REPORT DOCUMENTATION PAGE

Form Approved
OMB No. 0704-0188

Public reporting burden for this collection of information is estimated to average 1 hour per response, including the time for reviewing instructions, searching existing data sources, gathering and maintaining the data needed, and completing and reviewing the collection of information. Send comments regarding this burden estimate or any other aspect of this collection of information, including suggestions for reducing this burden, to Washington Headquarters Services, Directorate for Information Operations and Reports, 1215 Jefferson Davis Highway, Suite 1204, Arlington, VA 22202-4302, and to the Office of Management and Budget, Paperwork Reduction Project (0704-0188), Washington, DC 20503.

1. AGENCY USE ONLY (Leave Blank)		2. REPORT DATE March 1993		3. REPORT TYPE AND DATES COVERED Final May 91 - Aug 92	
4. TITLE AND SUBTITLE DESIGN AND ANALYSIS OF AN OPTICAL INTERFACE MESSAGE PROCESSOR			5. FUNDING NUMBERS C - F30602-91-C-0048 PE - 62702F PR - 4519 TA - 21 WU - PA		
6. AUTHOR(S) Dr. Q. Wang Song			7. PERFORMING ORGANIZATION NAME(S) AND ADDRESS(ES) Syracuse University 113 Bowne Hall Syracuse NY 13244		
8. PERFORMING ORGANIZATION REPORT NUMBER			9. SPONSORING/MONITORING AGENCY NAME(S) AND ADDRESS(ES) Rome Laboratory (C3DB) 525 Brooks Road Griffiss AFB NY 13441-4505		
10. SPONSORING/MONITORING AGENCY REPORT NUMBER RL-TR-93-19			11. SUPPLEMENTARY NOTES Rome Laboratory Project Engineer: David Cordeiro/C3DB/(315)330-4092		
12a. DISTRIBUTION/AVAILABILITY STATEMENT Approved for public release; distribution unlimited.			12b. DISTRIBUTION CODE		
13. ABSTRACT (Maximum 200 words) Optical technology has become a significant part of communications networks. This effort will design, develop, and experimentally evaluate an optical interface message processor (OPTIMP) that exploits the high bandwidth, parallelism, and high storage density offered by optics. The most time consuming operations such as switching and routing in communications networks will be performed in the optical domain. Because of this, the OPTIMP will not suffer from the electrical-optical/optical-electrical conversion bottlenecks and therefore perform switching and routing in the gigabits/sec range.					
14. SUBJECT TERMS Optical Communications Networks, Optical Interface Message Processor				15. NUMBER OF PAGES 164	
				16. PRICE CODE	
17. SECURITY CLASSIFICATION OF REPORT UNCLASSIFIED		18. SECURITY CLASSIFICATION OF THIS PAGE UNCLASSIFIED		19. SECURITY CLASSIFICATION OF ABSTRACT UNCLASSIFIED	
				20. LIMITATION OF ABSTRACT UL	

ABSTRACT

An optical interface message processor (OPTIMP) for high-speed high-bandwidth fiber optical communication networks is designed and analyzed. The goal of the OPTIMP is to exploit the inherent advantages of optics, such as parallelism, high-bandwidth, and high-speed to alleviate the optical-to-electronic, electronic-to-optic, and routing table search bottlenecks of the electronic interface message processors which are currently used in the fiber optic networks. In the OPTIMP, the source-destination code of the incoming data in the time domain is first converted to the spatial domain in a two-dimensional optical format. Then the routing table search is performed in a parallel manner by an optical table look-up processor. The output from this table look-up unit is an optical pattern to reconfigure the optical switching unit that routes the input optical data to the output optical link. The preliminary experimental results and the simulations based on the results show that the OPTIMP is capable to process and to route optical data in the Gbits/sec. range.

DTIC QUALITY INSPECTED 2

Accession For	
NTIS GRA&I	<input checked="" type="checkbox"/>
DTIC TAB	<input type="checkbox"/>
Unannounced	<input type="checkbox"/>
Justification	
By	
Distribution/	
Availability Codes	
Dist	Avail and/or Special
A-1	

CONTENTS

1	INTRODUCTION	1
	1.1 Background	1
	1.2 Objective and Results	2
	1.3 Organization of the Report	3
2	OPTICAL DEVICES	5
	2.1 Introduction	5
	2.2 Relevant Optical Devices	6
	2.2.1 Acousto-optic	6
	2.2.2 Magneto-optic	7
	2.2.3 Electro-Absorption	9
	2.2.4 Bistable Devices	10
	2.2.5 Fabry-Perot Interferometer	11
	2.2.6 Optical Logic Etalon (OLE)	11
	2.2.7 Multiple Quantum Wells (MQW)	12
	2.2.8 Self Electro-Optic Effect Devices (SEEDs)	13
	2.2.9 Quantum Well Envelope State Transition (QWEST)	14
	2.2.10 Ferro-Electric Liquid Crystals (FLC)	14
	2.2.11 Thermo-Absorption	14
	2.2.12 Liquid Crystal Light Valve (LCLV)	15
	2.2.13 Beam Coupling	15
	2.2.14 Photochromatic Device	16
	2.2.15 Microchannel Spatial Light Modulator (MSLM)	16
	2.2.16 Si/PLST Modulator	16
	2.2.17 Deformable Mirror Device (DMD)	17
	2.2.18 Charged Coupled Devices (CCD)	17
	2.2.19 Mach-Zehnder Interferometer	18
	2.2.20 Holography	18
	2.2.21 Light Sources	19
	2.2.22 Device Interconnections	20
	2.3 Summary	20
3	OPTICAL COMMUNICATION NETWORKS	48
	3.1 Introduction	48
	3.2 Classifications of Optical Switching Networks	49

3.2.1	Multiplexing	50
3.2.2	Switching	51
3.2.3	Optical Configuration	51
4	DESIGN AND ANALYSIS OF AN OPTIMP	65
4.1	Introduction	65
4.2	Design Approach	67
4.3	Architecture	69
4.3.1	Time Domain to Space Domain Conversion of SD Code	70
4.3.2	Parallel Routing Table Search	71
4.3.3	Control Pattern Generation and Signal Delay	73
4.3.4	Switching Network	74
4.4	Performance Analysis	75
4.4.1	Energy Requirements	75
4.4.2	Static Response Time of OPTIMP	76
4.4.3	Analysis of Packet Transmission Time	77
4.5	Summary	80
5	OPTICAL SWITCHING AND TRUTH TABLE LOOK UP USING PHOTOREFRACTIVE CRYSTALS	92
5.1	Binary Optical Switching with Photorefractive Polarization Holograms	92
5.1.1	Background and Motivation	93
5.1.2	Diffraction Properties of Birefringent Holograms	94
5.1.3	Output Degradation Due to Birefringent Diffraction	97
5.1.4	Two by Two Optical Directional Coupling Switch	102
5.1.5	Experimental Measurement for Optical Switching	104
5.1.6	Conclusion on Photorefractive Binary Switching	107
5.1.7	References for Section 5.1	108

5.2	Optical Table Look Up Based on Matrix Vector Multiplication	118
5.2.1	System Description	119
5.2.2	Experimental Demonstration and Discussion	122
5.2.3	Crosstalk Considerations	125
5.2.4	Concluding Remark on MVM	129
5.2.5	References for Section 5.2	130
5.3	Noise Performance of Photorefractive Holograms	136
5.3.1	The System Transfer Function of a Hologram	137
5.3.2	Output Intensities	140
5.3.3	Figures of Merits and Numerical Simulations	141
5.3.4	Conclusions on Photorefractive Noise	144
5.3.5	References for Section 5.3	146
6	CONCLUSIONS	150

1. INTRODUCTION

1.1. BACKGROUND

It is predicted that future multimedia transport networks must effectively provide a wide range of services with different throughput requirements such as voice (64 Kbits/s), data (Megabits/s), high definition television (100 Megabits/s), and human vision (10 Gigabits/s) [1]. Consequently, the designers of communication networks to support this wide range and dynamic capacity requirements will be limited by the processing capabilities of the nodes that perform the required routing and switching functions in the electronics domain. Furthermore, the low-transmission bandwidth of the electronic switches, and the Optical/Electrical and Electrical/Optical conversions present obstacles to fully exploit the large bandwidth offered by fiber optics. Currently, intensive research is focused on removing this obstacle by proposing design alternatives that attempt to achieve transmission as well as switching in optical technology.

In communication networks, the information exchange process can be divided into two parts: application related layers and communication related layers. The function of the latter is to route data packets, generated from the former, from one user to another. This is achieved by using transmission lines and intelligent switching elements, which are also called Interface Message Processors (IMPs). The IMPs examine the source-destination (SD) code in the *header* of a packet to determine the outgoing link to be used in routing the packet to its destination.

Signal processing and control based on optical technology is still in its infancy and lags behind what can be done using electronic technology. This has led to designing of

networks, such as the overlay network, in which the IMPs strip off the packet header from the message and convert the header into electrical signals. These electrical signals control the state of the photonic switches that route the packet at the input port to the required output port [2]. Others use different multiplexing techniques such as time-division and wavelength-division multiplexing to design photonic switches to route optical signals from their input ports to their corresponding output ports [3, 4, 5]. For example, in wavelength-division multiplexing, each input signal is modulated with a wavelength that corresponds to the destination port. The optical receiver at each output port is then used to select the input signal that is modulated with its commensurate wavelength. By modifying the tunable wavelength of these receivers, the output port can receive the input signal from any other input. In [6], a photonic knockout switch based on wavelength division multiplexing is proposed. Self-routing photonic switching with optically processed control is proposed in [7], where packets headers are encoded with packet destination addresses using either code-division or time-division encoding techniques.

1.2 OBJECTIVES AND RESULTS

The purpose of this project is to design and analyze an Optical Interface Message Processor (OPTIMP) that exploits high-bandwidth, parallelism, high information density offered by optics. The most time consuming operations such as switching and routing in communication networks are performed in the optical domain in the proposed system. Furthermore, the OPTIMP alleviates the optical/electrical and electrical/optical conversion bottlenecks and can perform switching and routing in the range of Gigabits/s.

As stated in the proposal, the complete building and testing of the OPTIMP would

take multi-year/manpower effort. This project is only a preliminary study. There are four tasks in the project. They are:

- (1) Survey of available and developing optical devices;
- (2) Survey of optical communication network system architectures;
- (3) Design and analysis of an optical interface processor;
- (4) Experimental evaluation of selected optical devices to be used as functional modules.

1.3. ORGANIZATION OF THE REPORT

The organization of the report is as follows: Chapter 2 summarizes the survey of optical devices and networks related to the proposed design. Chapter 3 surveys the optical communication networks. Based on the results, Chapter 4 details our design of the optical interface processor. The static time response, energy requirement, and achievable network operation are all analyzed. Because the design requires the expensive SEED device for time domain to spatial domain conversion and optically controlled switching units and the SEED is not available to us, we focused our efforts to the alternative photorefractive crystals. Chapter 5 discusses the applications of photorefractive crystals to optical switching and table look-up, which can be used in the optical interface processor. The preliminary experimental results on the characterization of liquid crystal projection TV as the programmable source-and-destination table is also included. Chapter 6 summarizes the report. The work distribution is as the following. Dr. Hariri wrote Chapter 3 and co-authored Chapter 4. Dr. Choudhary wrote Chapter 2 and co-authored Chapter 4. Dr. Song wrote Chapters 1, 5, 6, and co-authored Chapter 4. He also reviewed the whole report.

REFERENCES

- [1] Eric Nussbaum, "Communication Network Needs and Technologies-A Place for Photonic switching?" *IEEE Journal on Selected Areas in Communications*, vol.6 no.7, August 1988, pp.1036-1043.
- [2] H. Scott Hinton, "Architectural Considerations for Photonic Switching Networks," *IEEE Journal on Selected Areas in Communications*, vol.6, no.7, August 1988, pp.1209-1226.
- [3] A.S. Acampora, and M.J. Karol, "An Overview of Lightwave Packet Networks," *IEEE Network*, January 1989, pp.29-41.
- [4] A. Djupsjobacka, "Time Division Multiplexing Using Optical Switches," *IEEE Journal on Selected Areas in Communications*, vol.6, no.7, August 1988, pp.1141-1151.
- [5] R. Ian Macdonald, "Terminology for Photonic Matrix Switches," *IEEE Journal on Selected Areas in Communications*, vol.6, no.7, August 1988, pp.1227-1231.
- [6] Kay Y. Eng, "A Photonic Knockout Switch for High-Speed Packet Networks," *IEEE Journal on Selected Areas in Communications*, vol.6, no.7, August 1988, pp.1107-1116.
- [7] Paul R. Prucnal, and Philippe A. Perrier, "Self-Routing Photonic Switching with Optically Processed Control," *Optical Engineering*, vol.29, no.3, March 1990, pp.170-182, vol.25, pp.1220-1264 (1986).

2. OPTICAL DEVICES

2.1 INTRODUCTION

Photolithography for semiconductor manufacturing uses glass masks to pattern semiconductor photoresists with ultra-violet (UV) light. The wavelength of UV light, in this process, is the minimum image which can be developed. X-Ray lithography will reduce the image size to the 1000 Angstrom range. The wavelength of X-rays is the fundamental limitation to device shrinkage and hence their high speed. Other factors such as Ion Implantation targeting also characterize transistor performance, but again are limited by the exposure site size. The research and development of optical devices has displayed their high performance and applications to parallel processing. The next generation of semiconductor devices is expected to exploit the advantages of optical devices.

The differences between electronic and optical devices is inherently due to the characteristics of electrons and photons. Both electrons and photons can carry information and one can be converted to the other. The electron, with its negative charge, can influence other electric and magnetic fields. This interaction can manifest itself in system noise or crosstalk. Further, RC time constants set a limit on signal propagation and at high frequencies wire inductance will limit signal bandwidth. The photon is transferred at a higher frequency, hence has greater bandwidth available. Also, lacking any electric charge, the photon signal will not exhibit crosstalk, RC delays or inductance. Because photons can be transmitted with or without a waveguide (wire) they can be either broadcast through free-space or sent from point-to-point.

Light Modulators (LM's) are the key devices to optical information processing. Their uses include image converters, visual displays, phase correction, and as described below, components in optical computing. LM's in optical computing replace many of the circuits required in a digital computing system. Typically, LM's are manufactured into an array allowing 2-D input. An array of LM's is called a Spatial Light Modulator (SLM). By 1986 45 different types were being developed. Below are itemized the various technology principles governing many of these designs.

There are many types of SLM's to perform different optical functions. SLM's are critical as the input image generators, programmable "masks" and as processors and memory. As a processor, vector-matrix, matrix-matrix, matrix inversions and Fourier transforms, are all being developed. Holographic associative memory requires the use of SLM's for the input of partial data for pattern recognition. To "wire" a computer, SLM optical interconnections between processors and arrays as well as fanout operations can all be accomplished [1,2,3].

2.2 RELEVANT OPTICAL DEVICES

2.2.1 Acousto-optic

Acousto-optic devices are composed of a light source, spatial filter, a Bragg Cell, Fourier transform lens, and a piezoelectric transducer. When the transducer receives an electric signal a sound wave travels through the crystal. The sound waves result in a change of the index of refraction in proportion to the signal. When light is transmitted through the crystal it is diffracted into a Fourier transform which reveals the spectrum of the original input. Typically these devices are used to receive a RADAR source in a 1-D

manner. Acousto optical devices are being researched at the Naval Academy and at Carnegie-Mellon University.

2.2.2 Magneto-optic

Present devices have evolved from the "bubble-memory" technology. Magnetic lines of bubbles were created on a garnet bismuth substrate. Transmission appeared as black and white dots. Low efficiency required development of new substrates with better optical performance [4].

Magneto-optic devices are formed on a garnet lattice such as pyrope or almandine. The metals naturally occurring within a garnet can be substituted to vary magnetic and optic effect. On this substrate a magneto-optic film is deposited and etched into mesa-like regions. The mesa structures provide for stable magnetic regions with low mobility. The garnet device is then laminated with polarizing foils. Incident light passes through the first vertical polarizer. The garnet array's magnetic mesas rotate wave regions through either a positive or negative angle depending on the polarity of the mesa. The light has now been "personalized" according to the pattern of the garnet array. The next polarizer either blocks or transmits the various regions to realize the new data signal. The wave rotation is due to a Faraday effect which describes the nature of different refractive indexes for light polarized in clockwise and counterclockwise directions [4].

Orientation of the polarized axis determines the type of modulation as either amplitude or frequency. For amplitude modulation the incident wave travels through the polarized axis, for frequency modulation the wave travels parallel to the polarized axis. This principle is based on a property of wave propagation in crystals known as

birefringence. Birefringence is a consequence of the dielectric anisotropy, this is, in dielectrics the wave properties are different in the x and y axis. The phase of an optical beam passing through the crystal depends on the polarization of its electric field vector [2,29].

To reverse the polarity of a mesa cell two methods can be used. Thermal magnetic switching employs the dipole sensitivity to heat. At a certain temperature the magnetic field drops to zero. At this temperature a new field can be applied. Heat is generated by a resistor, formed with standard semiconductor methods, adjacent to the cell. Addressing is accomplished by a two sets of orthogonal wires. A write cycle would include heating the cell then transmitting an electric pulse. This write cycle takes about 25 μ S [4].

An enhanced version known as Light-Mod improves the access time. To achieve this the thermal cycle is eliminated. Instead, Boron is implanted under the X,Y addressing array, being sensitive to the magnetic field at the array intersections, induces the cell to switch states. The switching time for Light-Mod is reduced to 1 μ S [3].

Semetex's Sight-Mod is a commercially available magneto-optic SLM. Sight-Mod uses a bismuth doped iron epitaxial layer which is etched to form the mesa cells. Gold is deposited and etched to form the crossed array of address wires. The field at the gold intersections is weak and another current pulse from a separate wiring array moves the magnetic domain wall across the cell at switching speeds of 1 μ S. The device is manufactured in 48 x 48, 128 x 128, 1 x 576 and, under test, a 256 x 256 array [1,3].

PRITZ from the USSR uses Bismuth SiO₂ to optically address in .1 μ S. The device uses a thin slice of BSO coated with insulators and tapped with electrodes. When operated

in the reflection mode red light is reflected and blue-green light is transmitted. Its storage time is about 1-2 hours [29].

PROM(Pockets Readout Optical Modulator) developed by Itek, the University of California and Sumitomo is commercially available with performance and composition similar to PRITZ.

Limitations to efficiency of the garnet-based SLM are due to reflection and absorption losses. Ohmic loss in the magnetic selection array and crosstalk in the addressing array are due to there electronic nature. Manufacturing the garnet substrate is a trade-off of parameters effecting optical properties and switching speeds. For example, Bismuth can substituted into the crystal to Improve optical properties. This in turn, increases the anistrophy field and switching times. The light source is also a factor. Optical efficiencies are improved with infrared laser light rather than visible. The complication is producing the required thicker crystal. Material researchers continue to experiment with these parameters to create a versatile substrate with optimum properties [4].

2.2.3 Electro-Absorption

The operation electro-absorption devices is governed by the Franz-Keldysh effect. This is based on the variation of optical absorption with electric field. By altering an electrical input an optical beam is either absorbed or transmitted. The effect can be observed in GaAs and in fact all semiconductors, but it is negligible in Silicon. Electro-optics has been joined with CCD to form a SLM (see CCDs below) [28].

2.2.4 Bistable Devices

Most analogous to active electronic devices are the optical bistable devices. They have a binary function of either transmitting light or blocking the transmission. Bistable devices can be stand alone components or built as a SLM array. Bistable devices operate in the picosecond range at low power levels while allowing high density and parallelism. Several bistable devices technologies have been developed. These include the Fabry-Perot etalon, SEEDs and multi-valued logic devices. These devices require the material properties of nonlinearity and optical feedback [4]. Feedback is a function of change in optical properties which influence the device reaction to incident photons. Bistable devices can exhibit either internal feedback known as optical bistability from absorption, or external feedback from a resonant cavity, or electric field. Nonlinearity is the property of an optical material to change its index of refraction in relation to incident photon energy near the material bandgap. When the input beam contacts the nonlinear material it imparts energy on any loosely coupled electrons. This creates a charge separation which results in the refraction change. Bistable devices are characterized by having a read and recovery period. The recovery period is required to allow the device to stabilize before a valid access to the device can be done. A variety of nonlinear materials are under development. These range from inorganic insulators with millisecond response, to large organic molecules with rapid response but naturally have environmental oxidation problems . Superlattices, layers of AlGaAs, HgTe, or Cd and others, are showing the advantages of both organics and inorganics. These layers can create a sequence of quantum wells and are classified as MQW's, Multiple Quantum Wells [1, 3, 4, 27].

2.2.5 Fabry-Perot Interferometer

The Fabry-Perot device consists of three layers. A center resonant cavity of nonlinear material is capped on either end with semi-transparent mirrors. The device is classified as refractive optically bistable with external cavity. These are named etalons. When an incident input beam strikes the device its frequency and intensity control the bistability. A high intensity bias beam is either transmitted or blocked. A low intensity detuned input will allow only a partial bias beam to pass. A higher intensity input, although relatively low compared to the bias beam, will create a resonance of laser wavelength. This is due to a change in the index of refraction which results in an optical path allowing constructive interference within the cavity. The high bias intensity then appears through the output mirror. This is comparable to electronic three terminal devices in that a gate or base of low current switches a current of greater magnitude. Both Zinc Sulfide and GaAs devices have been developed. The faster is GaAs with a 50/50ps read/recovery time [1, 21, 28].

2.2.6 Optical Logic Etalon (OLE)

An OLE is similar to the bistable etalons except that bistable operations are not used. A probe pulse at one wavelength is controlled by an input pulse at another wavelength to change the materials' transmission. The GaAs material is insensitive to the probe pulse, but absorbs the input pulse. The absorbed light changes the index of refraction allowing the etalon to resonate and transmit at the probe frequency. The OLE is a three terminal device in that the input beam controls the probe beam. By shifting the frequency of the input, logic functions result i.e., NOR, NAND, XOR, OR, or AND. In

electronic three terminal devices the output can be used to switch the input ie. cascaded logic. The OLE cannot yet achieve cascading because the wavelengths for the probe are longer than the high frequency input. But being a three terminal device the input signal is sensitive to noise. The device operation has a fast 40ps recovery time after a 1ps read [4, 3, 6].

2.2.7 Multiple Quantum Wells (MQW)

A MQW is hundreds of alternating layers of GaAs/AlGaAs or InAs/GaAs. Each 10nm layer of GaAs is known as a quantum well because the adjacent layers of AlGaAs have a larger bandgap which confines the electrons within the GaAs. The MQW is capped with 1um of AlGaAs. Its function depends on the potential across its upper and lower layers. This voltage varies the excitation peak at the band-edge and hence the absorption properties, known as the Stark effect. The Stark effect is similar to the Franz-Keldysh effect, but much stronger. MQWS are very sensitive to the electric field perpendicular to the semiconductor layers which makes them ideal for 2-D arrays. The result of this structure is a device which modulates wavelengths on the order of 1.5 um using an external source of from 2 to 20 volts. The processing of MQW's became possible with the advent of molecular-beam epitaxy (MBE). Epitaxy is a single crystal deposition process to insure that all semiconductor devices are created within a common crystal lattice. The problem in the past is that thicker (1um) epi layers required that the lattice of the deposited material and the substrate were to match. This limited the variety of materials which could be deposited. Announced in 1986 was strained-layered superlattice (SLS). This technique by Dawson of Sandia National Labs uses the MBE method to

deposit thinner material layers. The technique allows the interface strain between the materials to be absorbed by elastic deformation to form these viscoelastic layers [6, 9, 27].

Researchers J. Maserjian and Sverre T. Eng of JPL Lab used MBE to produce a MQW integrated with a photo diode, shown below. A writing beam requires an energy greater than the GaAs bandgap, while the reading beam would be of less energy than the MQW excitation level. The writing signal would charge the upper N+/P+ diode increasing the voltage across the MQW. The reading signal is modulated by the MQW. The diode can be reset using the external V supply. In the lower portion of the Figure 2.11 are shown details of the MQW and associated energy conduction band [34].

2.2.8 Self Electro-Optic Effect Devices (SEEDs)

SEEDs are essentially photodetectors combined with MQWs to give an optically controlled device with optical outputs. The SEED was patented in 1986 by D. Miller of AT&T Labs. In this case the absorption of incident light increases the absorptivity of light creating a positive feedback which lowers transmissivity. The MQW within the SEED has its absorption changed by the electric field across the MQW, as described previously. The electric field can be varied by voltage changes caused by the presence of light in the photodetector. The photocurrent produced is used as feed-back to cause the device to act as a gate. The manufacture of SEEDs is so similar to semiconductors that integration with them certainly is possible. The SEED structure in general is mechanically quite durable so exploiting its properties in a real computing system is likely. The recovery time after a 30ns read, is another 30ns [7].

The S-SEED is a device that uses two Symmetrical MQWs in series. The S-SEED is a 3-terminal device which can reduce circuit complexity. M-SEEDS have Multiple (N) MQW's in series to obtain 2^N states for N light beams. The integration of SEEDs with standard semiconductor devices has produced B-SEEDs and F-SEEDs; for Bipolar and FET transistor integration [22].

2.2.9 Quantum Well Envelope State Transition (QWEST)

A MQW known as QWEST, Quantum-Well Envelope State Transition, was developed by L. West of AT&T [31]. The MQW is designed so electrons can make transitions only between the two lowest energy levels of the conduction band. QWEST has an extremely strong nonlinearity. MIT has verified a switching speed under 5ps and a recovery time under 2ps. [27].

2.2.10 Ferro-Electric liquid Crystal (FLC)

Announced in January 1991 by STC Technology of London is a bistable optical addressed SLM (BOASLM). The FLC is in the form of a thin slab placed between conductive plates. A voltage applied across the plates causes light's polarization axis to rotate. Hence, the input light is changed according to a controlling voltage. The FLC is reported to have a higher resolution than a SEED or MQW device. In addition to memory, numerous logic gates, flipflops, and accumulator functions can be performed [10].

2.2.11 Thermo-Absorption

Heat absorption devices are created by depositing an oil film on a plastic substrate. Incoming light heats the plastic causing local deformations. The oil film conforms to the

deformations and deflects an incoming light signal. Many companies are researching this technology due to its low cost combined with 10ms write time, high resolution and storage time of over a year [3].

One heat-sensitive plastic PVK:TNF, poly-n-vinylcarbazole 2, 4, 7 trinitrofluorenon, is being developed and marketed by Newport Research Corp, along with Harris, CBS Research, the Environmental Research Institute of Michigan, Fujinon, Honeywell and Kalle-Hoechst [3].

Librascope is a Hewlett-Packard and Singer development. This uses a heat-sensitive liquid crystal. Its write time of 5 μ s is offset by a storage time of about a month and low resolution [3].

2.2.12 Liquid Crystal Light Valve (LCLV)

The LCLV was developed by Hughs for light pattern input. The device is made of several layers, primarily a liquid crystal coated with cadmium sulphide. An AC voltage is applied across the device. Variations of light on the Cadmium Sulphite (Cds) surface cause charge variations in the crystal. To read the modulation a laser is directed into the liquid crystal and reflected back with a rotation of its polarization. LCLV can read and write with any spectral composition, but can be tuned to coherent light wavelengths. Manufacturing is expensive due to the high tolerance required to maintain uniform thickness. Its 10ms write time and 15ms storage require real-time data processing rather than use as memory [1, 3].

2.2.13 Beam Coupling

In July 1989 NASA's Jet Propulsion Laboratory described light modulation via

beam-coupling in GaAs. Their technique relies on cross-polarized beam coupling. The crystal is oriented so the components of the electric fields of the two beams that lie in the plane of the two electro-optic axes bisect the angle between the two axes. Because of changes to the index of refraction the resultant diffracted beam is rotated 90 degrees from the incident beam. In this way a wave is modulated from its original form using all optical inputs [39].

2.2.14 Photochromatic Device

A SLM proposed by David Beratan and Joseph Perry of Caltech and published November 1989 is known as a Photochromatic SLM. Their concept is based on the transfer of electrons and acceptor molecules randomly distributed in a "glassy-polymer". The charge transfer would cause changes in the transmission characteristics and therefore could modulate light entering the polymer. The writing beam would scan the polymer creating a mask of varying transmission rates to provide spatial modulation. Polymer processing was accomplished using oblique ion beam exposure to pattern etched grating surfaces [40].

2.2.15 Microchannel Spatial Light Modulator (MSLM)

MSLM has a photocathode to capture an input signal by creating an electron image of the optical amplitude. The image is amplified by the micro-channel plates and cast on a dielectric mirror. The deposited charge alters the refraction index and modulates the output laser [6].

2.2.16 Si/PLZT Modulator

The Si/PLZT modulator is manufactured from a base of electro-optic ceramic

(PLZT) which has a large optical nonlinearity. On the same substrate is a photodetector and silicon drive and load transistors. A write signal on the phototransistor Area varies the capacitive charge and then the index of refraction in the PLZT. The projected speed is 100kHz coupled with a million cells in parallel [6].

2.2.17 Deformable Mirror Device (DMD)

A DMD is a 2-D array of MOS transistors with a reflecting layer deposited over the surface. The layer is etched to form a cantilever reflector over each transistor. When the device is active the cantilever is statically pulled toward the device. This deforms the surface and an input beam will have its phase delayed accordingly [6, 9, 19].

2.2.18 Charged Coupled Devices (CCD)

Charged coupled devices were developed in the early 1970's. Their operation is described completely by Sequin and Tompsett (1975). The standard CCD is based on two adjacent MOS capacitors. The potential wells are designed to merge (couple) so any mobile charge will accumulate in the well with the highest potential. The transfer of charge is controlled by the electrodes. GaAs CCD technology is compatible with GaAs FET's and MQW technology. The optical detection properties of CCDs and this technology compatibility allows an interface to be made between optical and electrical components. For example in 1984 a CCD was used as a detector array from a LiNbO3 electro-optic D/A converter. In 1982 an acousto-optic spectrum analyzer incorporated CCDs to receive the angled acoustic output. The angle corresponding the signal frequency is translated by the CCD into a spatial variation, thus giving an instant Fourier transform of the input [36].

Introduced by W . Goodhue in 1985 are the integrated CCD and SLM . The SLM/CCD design is composed of a semi-insulating GaAs substrate layered with an n-type "buried-layer" under a schottky gate [4].

CCD-Addressed MQWs have the advantage of a light detector integrated onto a SLM [9, p.99]. With integrated manufacturing the need for separate interconnects is reduced and performance is improved [4].

2.2.19 Mach-Zehnder Interferometer

The typical application of a wave guide is to direct a light beam along a fiber with a high index of refraction compared to its shield. This restricts the beam to within the waveguide. A different technique allows this technology to be used as a logic device. The simplest structure is a slab waveguide of LiNbO₃. A thin film of high index of refraction is deposited to form a wave guide which splits the beam to pass through an electric field then rejoins the beam. Variations of voltage produce different functions. The Mach-Zehnder interferometer uses this principle to realize a variety of logic gates [11,15].

2.2.20 Holography

Holography was invented by Dennis Gabor in 1948. It remained a curiosity until lasers were invented in 1962. Holography is a technique which allows a whole ("holos" from Greek) image to be recorded. Hence, the hologram is used for storage technologies in optical systems. Originally a photographic material was exposed with a reference beam. Split from the reference, a beam reflected off an object to be recorded and impinged on the same photomaterial. The two beams interfered and formed a pattern which could be reconstructed with the reference beam. This is now known as hoiographic interferometry.

By 1989 the photomaterial was changed to photorefractive crystals. The crystals can be formed into thicker layers offering good selectivity. The image is re-usable and can be overlaid for continuous "learning" [5, 20].

Alan Johnston's team at Jet Propulsion Labs have developed a 2-D relief hologram in silicon. The hologram converts a diverging beam from a laser array to converging beams on a row of detectors. The laser array is an addressing circuit for a RAM. The hologram takes the laser address and clocking signals and redirects them to address certain RAM cells. The hologram is re-programmable in that the address mapping can be dynamically changed [25].

Page-oriented Holographic Memories (POHMs) were developed to store many adjacent holograms on one substrate. The holograms are made so they have a common 2D output plane. By deflecting a laser at any one hologram the corresponding "page" appears at the output [17, 41].

2.2.21 Light Sources

For optical computing, arrays of 1 and 2 dimensional light sources are required. The research into laser diodes offers several solutions. Among various types of surface-emitting lasers, grating-coupled surfaces using the first order diffraction of second order grating have various advantages. The grating is etched onto the laser surface to produce the diffraction. They deliver high power efficiently with only a small beam divergence. Chip surface Laser diodes offer coherent beam control as well as device integration. Its beam emits normal to the chip surface permitting alignment to other optical devices. The surface mount laser is constructed from an 45 degree overetched MQW. This overetched

angle directs light to the chip surface. Other laser diodes are available with edge emitting beams. These could be useful for transmission to chips mounted flat, adjacent to one another [6, 28].

2.2.22 Device Interconnections

Optical interconnects are not necessarily devices, but certainly are required to connect devices. The typical application of a wave guide is to direct a light beam along a fiber with a high index of refraction compared to its shield. This restricts the beam to within the waveguide. Optical fiber technologies are well established and described in available literature. Thin film wave guides for high density applications are being developed from TaO₅, Al₂O₃, and ZnO₂. These waveguides can carry optical signals directly to transceiver circuits [15, 28].

Free-Space interconnection refers to the use of optical transmitters and receivers to bridge space without the use of any material wave guide. NASA's Jet propulsion Lab has developed a 2-level relief hologram . A laser diode array transmits a decoded address through space to the holographic element. The holographic element redirects the light to the required RAM row/column select photodetector. The addressing and clocking of the RAM can be received as a single frequency laser address and fanned-out to many cells simultaneously. In general all optics-based computing systems have a higher degree of connectivity. The achievable data rates and the number of parallel channels is beyond the capability of electronic systems [20, 21].

2.3 SUMMARY

The above devices are the basis of optical processing. In all cases modulation can

vary in each device throughout the array. The location of the modulation across the array is equally important to the amplitude of modulation. The output of a SLM is a wavefront which has been modulated corresponding to the input of each device in the array. With SLM technology it is possible to update every pixel of an image in parallel, and perform complex operations such as pattern recognition and image manipulations [1]. Optical devices will lend themselves either to analog or digital processing. An analog device generally has properties of high speed, moderate resolution and low accuracy. Their use extends to areas where high bit accuracy is not necessary. Analog devices excel in functions of pattern recognition, correlation, and Fourier transforms. The digital optical devices achieve high accuracy, flexibility in function and are logically similar to their three-terminal Bipolar and FET devices. The individual speeds for optical devices have not yet equaled electron device speeds, but given the parallelism of 2-D arrays, the throughput of optical technologies will be much greater [3].

References

- [1] Efron, Uzi, "Spatial Light Modulators for Optical Information Processing," *SPIE*, ICOCC 1986, vol.700, pp.132-144.
- [2] Gibson, D.G., "Progress in Spatial Light Modulator Performance: a status Report," *Optics and Laser Technology*, November 1987, pp.25-28.
- [3] Feitelson, Dror, *Optical Computing*, The MIT Press, Massachusetts, 1988.
- [4] Bell, Trudy E., "Optical Computing: A Field in Flux," *IEEE Spectrum*, August 1986, pp.34-57.
- [5] Arrathoon, R., *Optical Computing, Digital and Symbolic*, Marcel Dekker Inc., 1989.
- [6] Casasent, D., *Optical Data Processing*, Springer-Verlag Pub., vol.23, 1978.
- [7] Neff, John, "Major Initiatives for Optical Computing," *Optical Engineering*, January 1987, vol.28, no.1, pp.2-9.
- [8] Miller, David A.B., "Quantum Well Devices for Optical Computing and Switching," AT&T Labs, WAA2-1, January 1989, pp.413-415.
- [9] Murdocca, M.J., Sugla, B., "Design of a Symbolic Substitution Based Optical Random Access Memory," *Optical Society of America*, 1989 Technical Digest Series, Optical Computing, paper MH1- 1, pp.92-95.
- [10] McAulay, A.D., "Spatial-Light-Modulated Interconnected Computers," *Computer*, October 1987, pp.45-57.
- [11] de Bougrenet de la Tocnaye, J.L., Brocklehurst, J.R., "Parallel Access Memory Using an Optically Addressed Ferroelectric SLM," *Applied Optics*, 10 January 1991, vol.30, no.2, pp.179-180.
- [12] Mirsalehi, M.M., Abushagur, M.A.G., "Optical and Optoelectronic Computing," *Advances in Computers*, vol.28, Academic Press Inc., pp.193-219.
- [13] Huang, K-T, Huang, K-S, "Parallel Architectures for Digital Optical Computing and Their Design Principles," *SPIE*, ICOSE 1990, vol.1230, pp.714-720.
- [14] Johnson, K.M., Handschy, M.A., Pagano-Stauffer, L.A., "Optical Computing and Image Processing with Ferroelectric Liquid Crystals," *Optical Engineering*, May 1987, vol.26, no.5, pp.385-390.

- [15] Murdocca, M.J., Huang, A.J., Jahns, and Streibl, N., "Optical Design of Programmable Logic Arrays," *Applied Optics*, vol.27, no.9, pp.1651-1660, May 1, 1988.
- [16] Sueta, T., Izutsu, M., "Guided-Wave Light Modulators," *Optical Computing in Japan*, 1989, pp.383-392.
- [17] Kyuma, K., Kojima, K., Ohta, J., "Optical Neural Networks System and Device Technologies," January 1990, pp.159-172.
- [18] Caulifield, H., John, Jason Kinser and Steven K. Rogers, "Optical Neural Networks," *Proceedings of the IEEE* 77(10), pp.1573-1583.
- [19] Egorov, V.M., Kostsov, E.G., "Optical Integrated Computing Devices," *SPIE, ICOSE* 1990, vol.1230, pp.734-742.
- [20] McAulay, A.D., "Optical Crossbar Interconnected Digital Signal Processor with Basic Algorithms," *Optical Engineering*, January 1986, vol.25, pp.82-85.
- [21] Hutcheson, Lynn D., "Optical Interconnects Replace Hardware," *IEEE Spectrum*, March 1987, pp.30-35.
- [22] Berra, P. Bruce, Arif Ghafoor, Mohsen Guizani, Slawomir J. Marcinkowski and Pericles A. Mitkas, "Optics and Supercomputing," *Proceedings of the IEEE* 77(12), December 1989, pp.1797-1815.
- [23] Streibel, Norbert, Karl-Heinz Brenner, Alan Huang, Jurgen Jahns, Jack Jewell, Adolf W. Lohmann, David A.B. Miller, Miles Murdocca, Michael E. Prise, and Theodore Sizer, "Digital Optics," *Proceedings of the IEEE* 77(12), December 1989, pp.1954-1968.
- [24] Cathey, W. Thomas, Kelvin Wagner and William J. Miceli, "Digital Computing with Optics," *Proceedings of the IEEE* 77(10), October 1989, pp.1558-1572.
- [25] Hecht-Nielsen, Robert, "Neurocomputing: picking the human brain," *IEEE Spectrum*, March 1988, pp.36-41.
- [26] Johnsten, A., "Optical RAM," *NASA Tech Brief*, May 1989, vol.13, no.5, pp.32-35.
- [27] Cheng, L-G., "Integrated Semiconductor/Optical Information Processor," *NASA Tech Brief*, October 1989, vol.13, no.10, pp.22-24.
- [28] West, Lawrence C., "Picosecond Integrated Optical Computing" *Computing*,

December 1987, pp.34-42.

- [29] Sluss, J.J., Veasey, D.L., Batchman, T.E., "An Introduction to Integrated Optics for Computing," *Computer*, December 1987, pp.9-23.
- [30] Huignard, J.P., "Spatial Light Modulators and Their Applications," *SPIE*, vol. 702, ITM-IDAQ 1986, pp.291-301.
- [31] Dolson, Mark, "Machine Tongues XII: Neural Networks," *Computer Music Journal*, 13(3), Fall 1989, pp.28-40.
- [32] Ishihara, S., "Optical Information Processing," *Science and Technology in Japan*, July 1989, pp.12-14.
- [33] Conference on Lasers and Electro-optics, Technical Digest 1986, pp.366-372.
- [34] Aull, B., and Burk, B., International Soc. Opt. Engineers 1988, vol.825, pp.121-127.
- [35] Maserjian, J., Eng, S.T., "Photo-Diode Coupled Light Modulator," NASA Tech Brief, February 1989, vol.13, no.2, pp.22-23.
- [36] Neff John, "Parallel Computing and Photonics," *Photonics*, August 1989, pp.135-142.
- [37] Sequin, C.H., Tompsett, M.F., "Charge Transfer Devices," *Academic Press*, 1975.
- [38] Sage, Jay P., "Electronics vs. Optical Implementations of Neural Networks," *Optical Computing*, 1989, vol.9, pp.5-8.
- [39] Water, T., "Optical Computer," *Discover*, January 1991.
- [40] Cheng, L-J., "Spatial Modulation In GaAs," NASA Tech Brief, July 1989, vol.13, no.7, pp.46-48.
- [41] Beraten, D.N., "All-Optical Photochromic Spatial Light Modulator," NASA Tech Brief, November 1989, vol.13, no.11, pp.41.
- [42] Alphonse, G.A., "Parallel Optical Random Access Memory (PORAM)," NASA contractor report 4241, David Sarnoff Research Center, Princeton N.J., 1989.
- [43] Flynn M.J., "Some Computer Organizations and Their Effectiveness," *IEEE Transactions*, C-21:948, 1972.

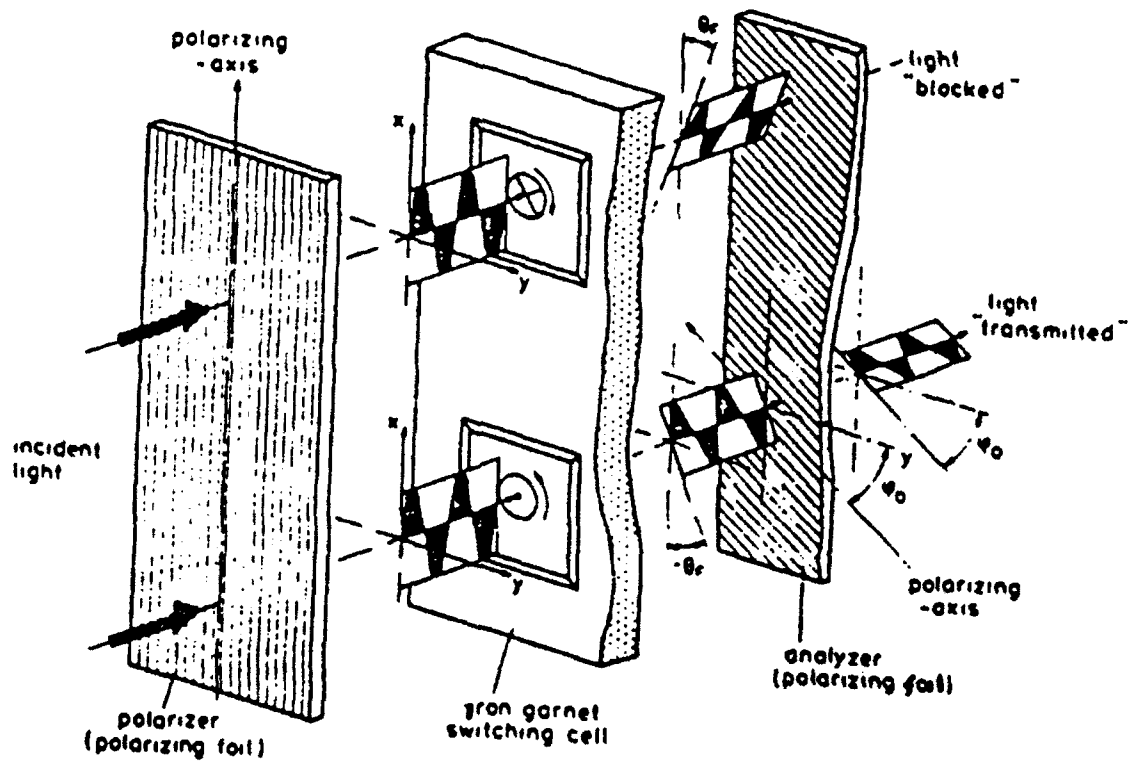
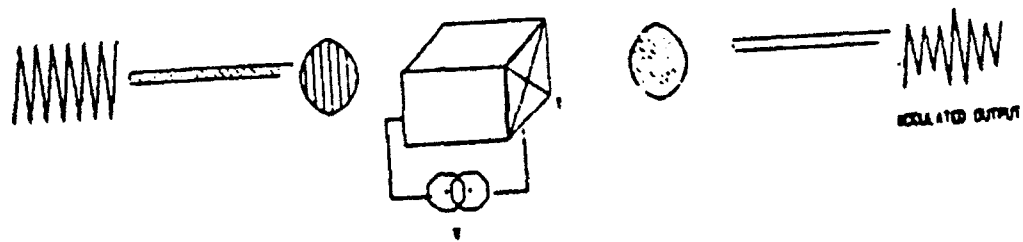


Figure 2.1 Magneto-Optic SLM

AMPLITUDE MODULATION



FREOLENCY MODULATION

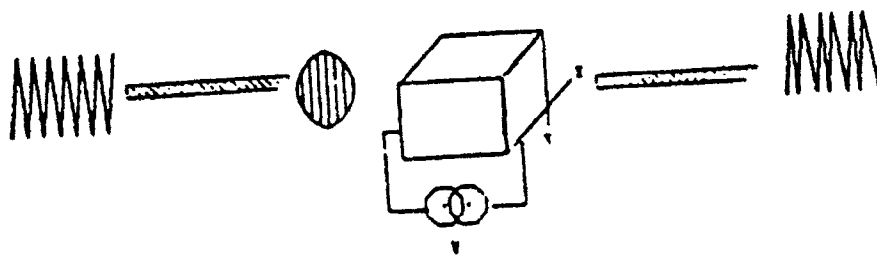
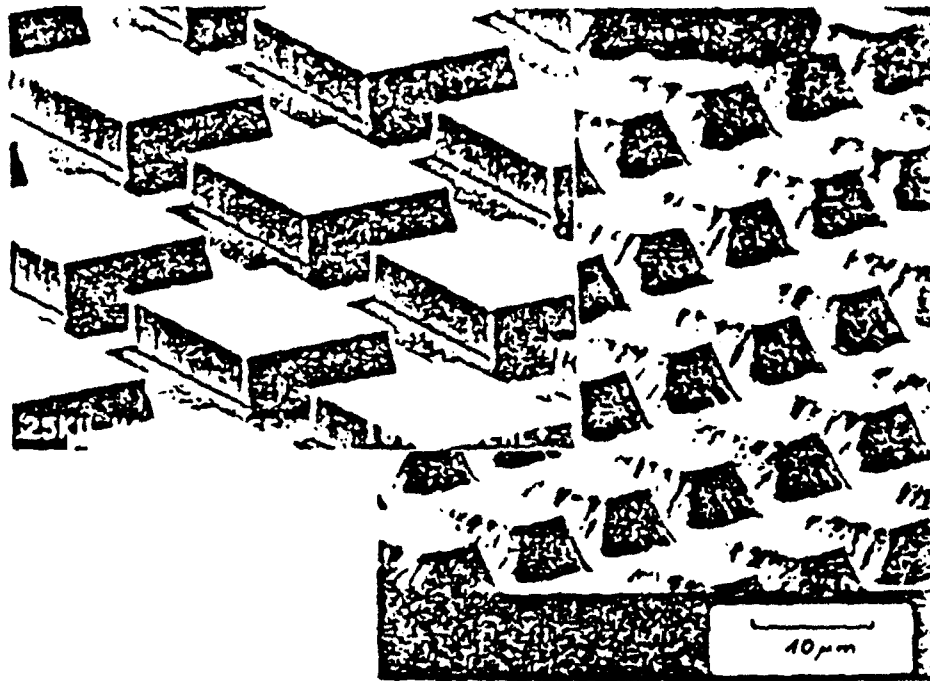
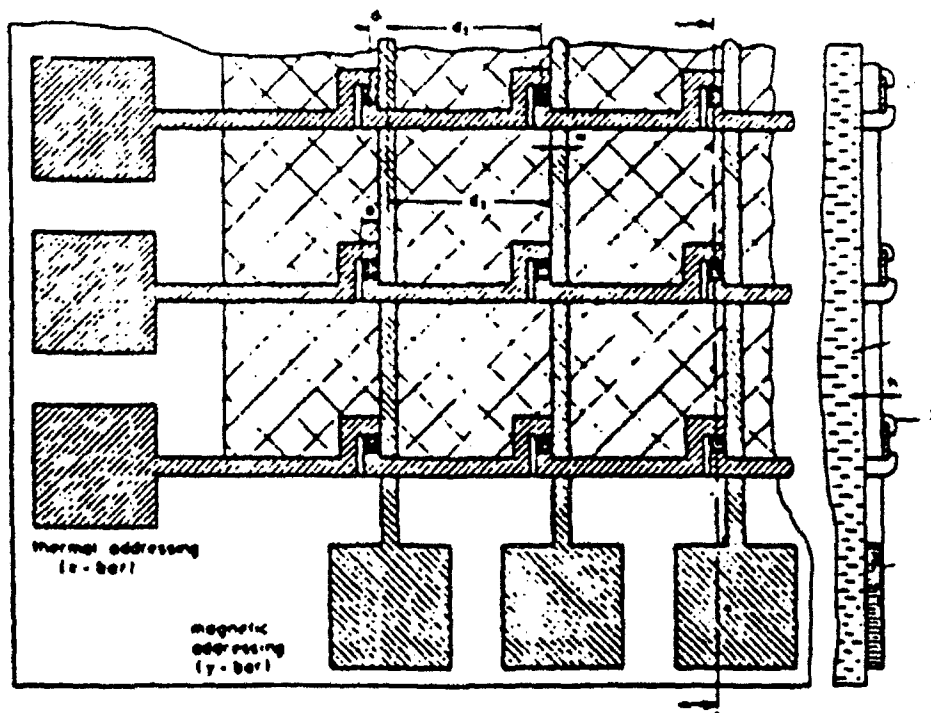


Figure 2.2 Types of Modulation



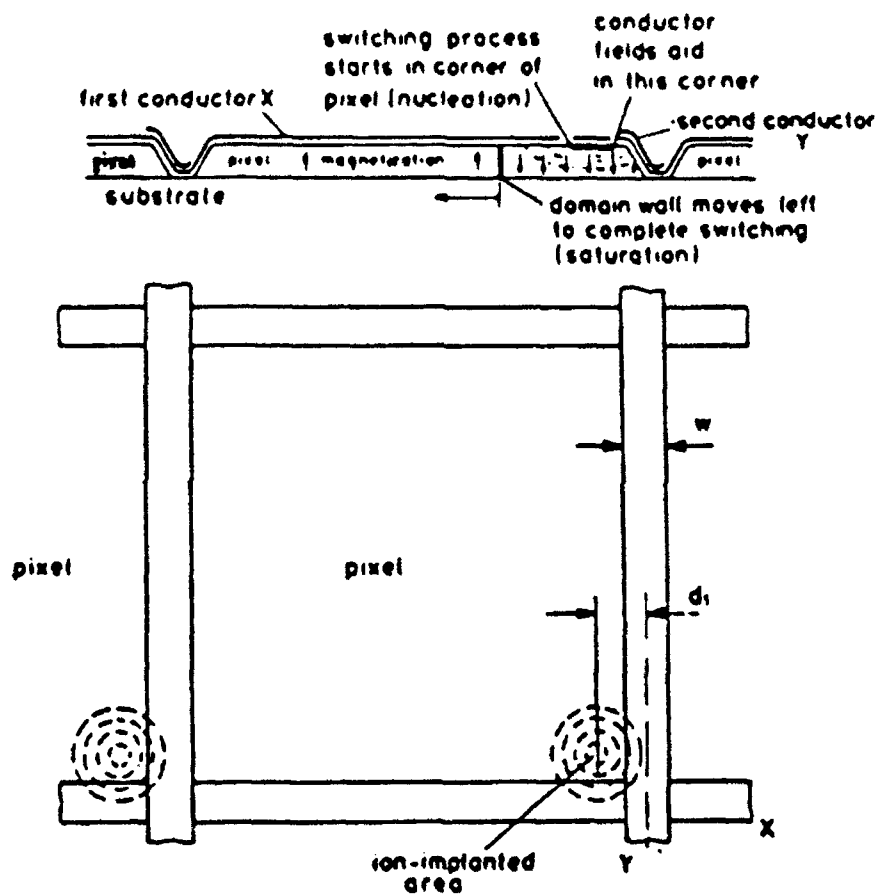
Structuring of the magneto-optic film. The magneto-optic film deposited on a substrate is etched into separate light switching cells by a photolithographic etching process. Each cell is 10 to 100 μm^2 .

Figure 2.3 Structure of Magneto-Optic Film



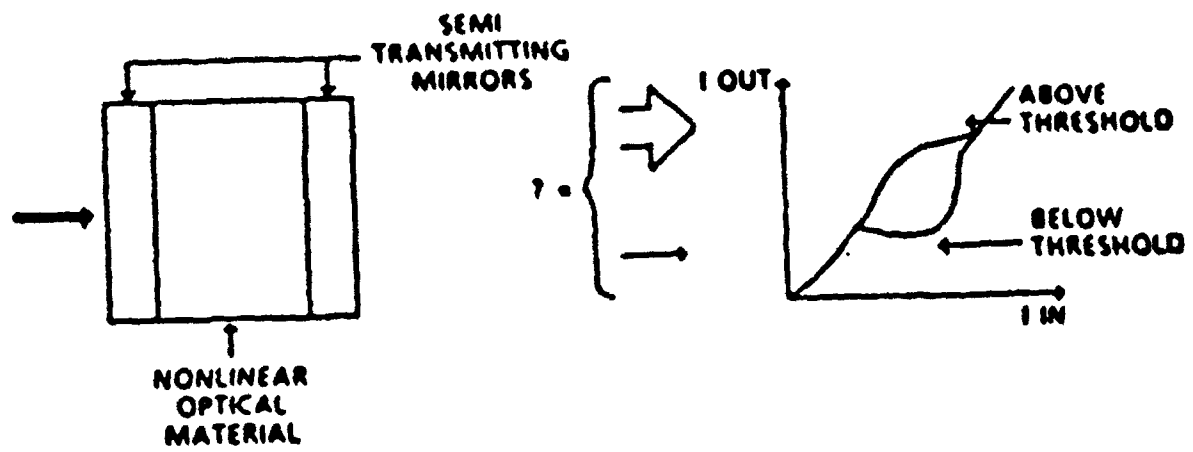
Schematic of a thermally addressed magneto-optic modulator. A heating element covers part of a magnetic-optic island. The heating elements of the islands of a line are connected in series and addressed via the z -bar. Column addressing is performed by the magnetic y -selection bars. At the cross points, an insulating layer is placed between the z - and y -bars (not shown in the sketch).

Figure 2.4 A Thermally Addressed Magneto-Optic Modulator



Design of the light-mod with x- and y-addressing bars and ion-implanted areas close to the cross points of x- and y-bars.

Figure 2.5 Design of the Light-Mod with x- and y-addressing Bars



Bistable optical device (BOD).

Figure 2.6 Bistable Optical Device

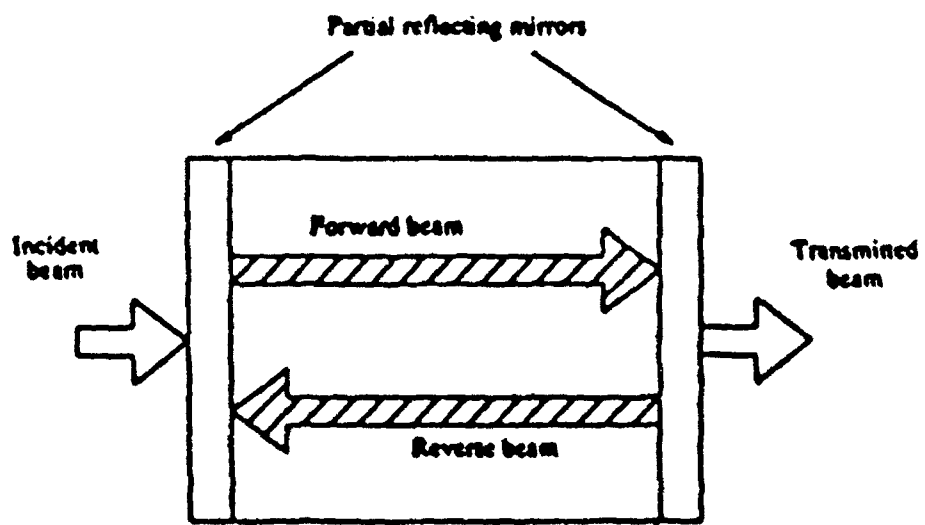


Figure 2.7 Fabry-Perot Cavity

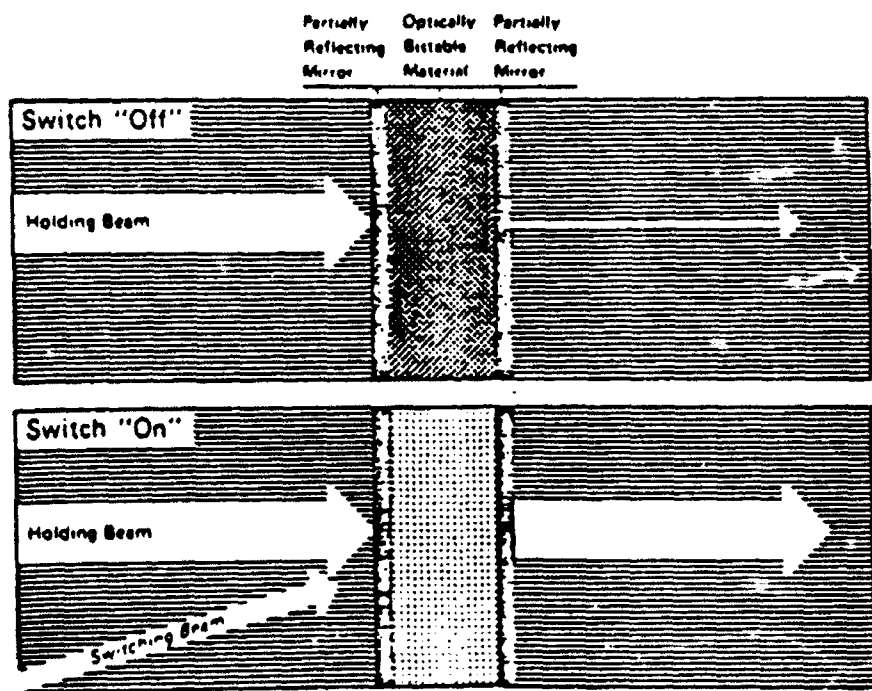


Figure 2.8 Two Beams Switching in a Nonlinear Etalon

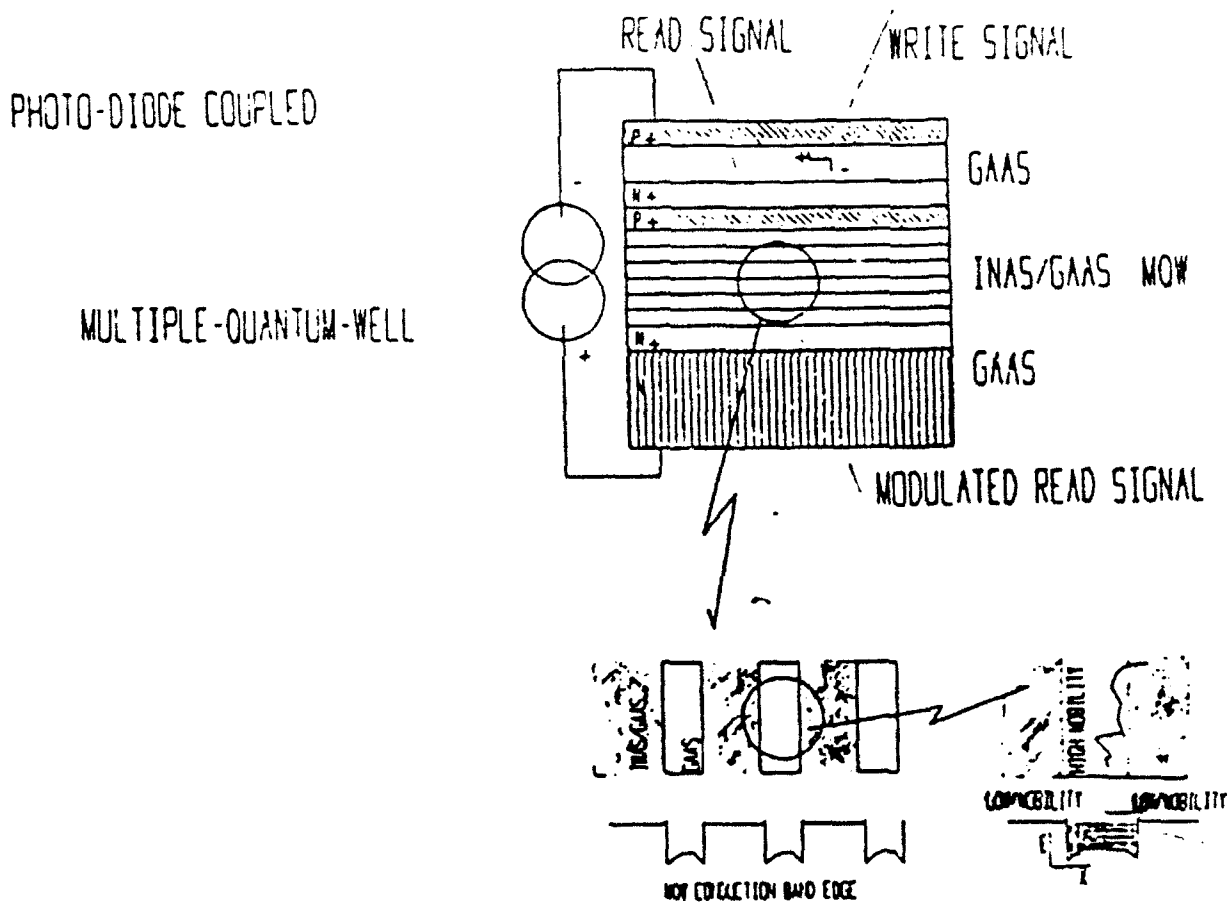


Figure 2.10 Multiple Quantum Well

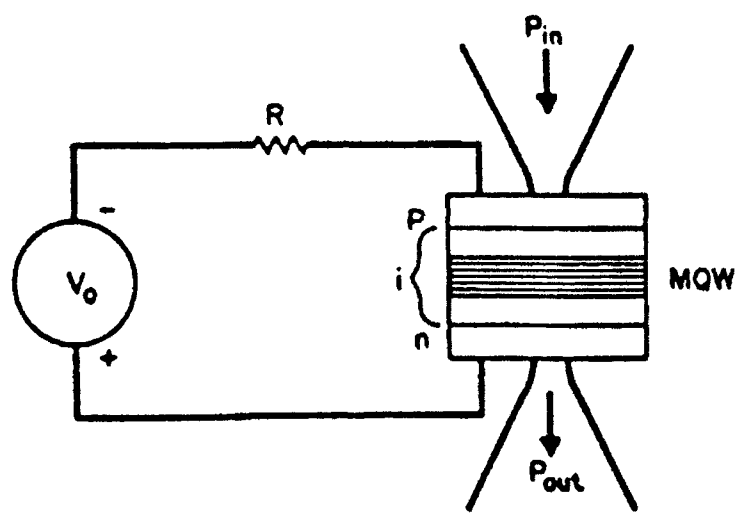
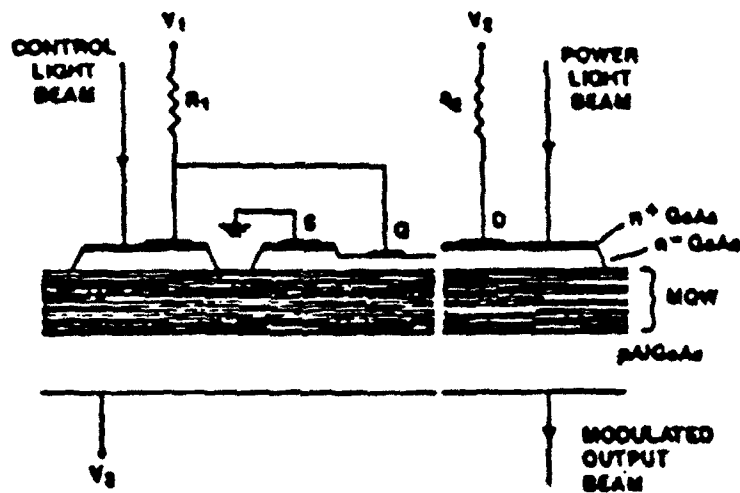


Figure 2.11 Generalized Schematic of the SEED



Schematic of field effect transistor SEFD (F-SEED) showing MESFET fabricated in top layer of quantum well modulator/detector diode.

2.12 Field Effect Transistor SEED (F. SEED)

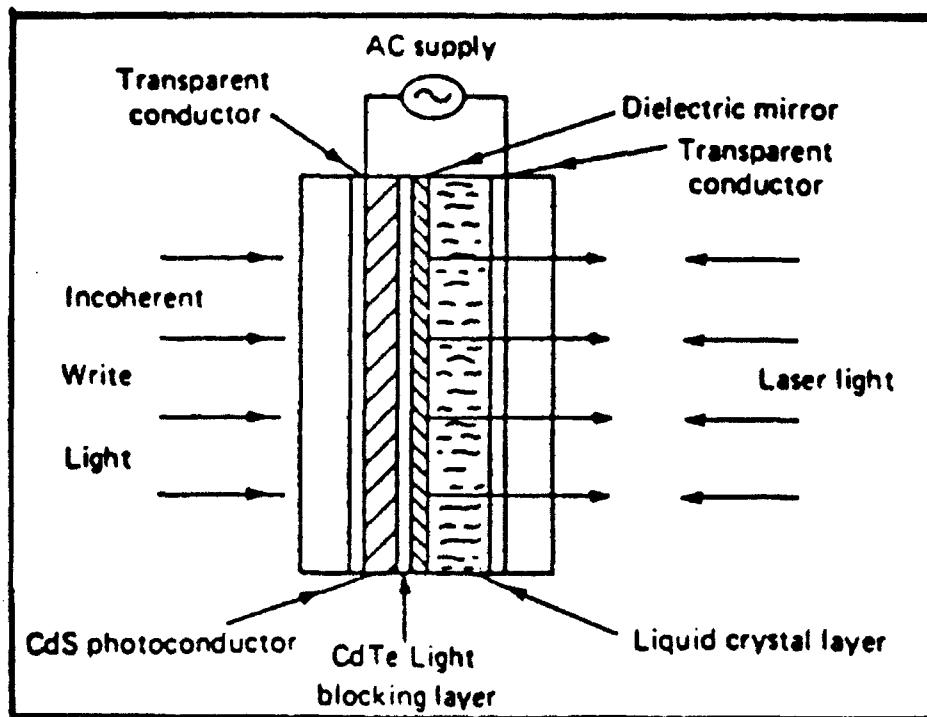


Figure 2.14 Schematic of LCLV

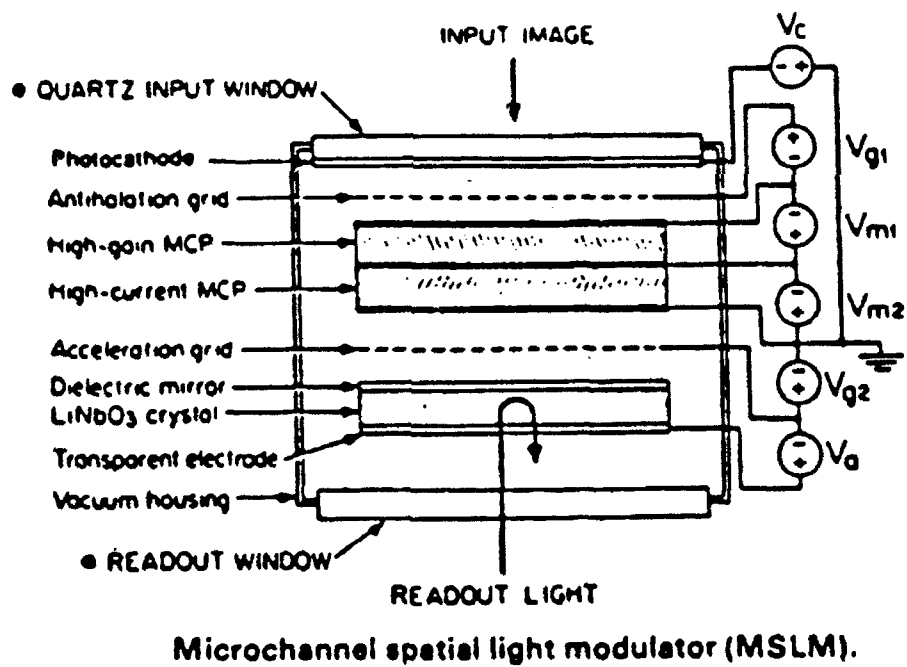
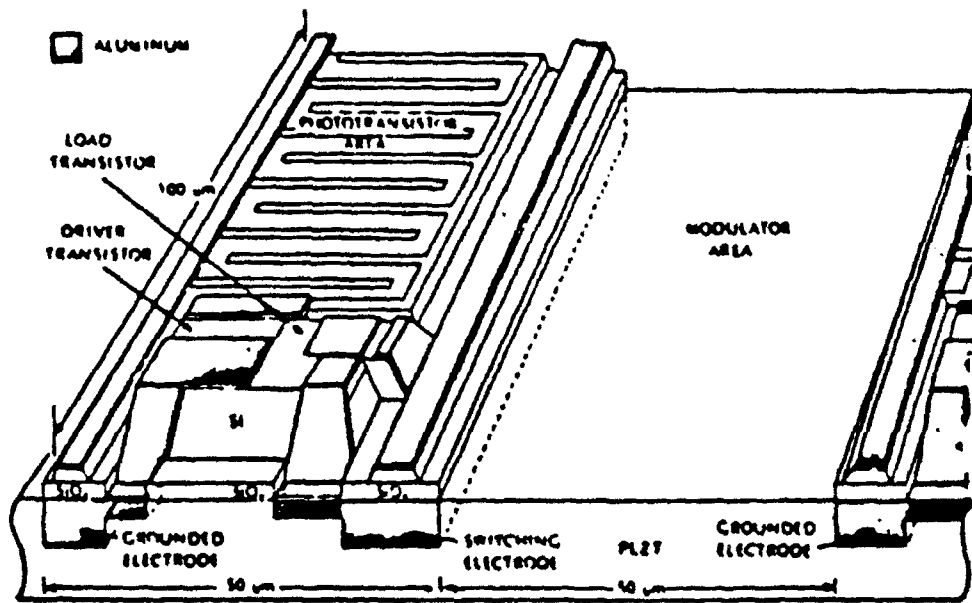


Figure 2.15 Microchannel Spatial Light Modulator (MSLM)



Silicon on PLZT light modulator (Si/PLZT).

Figure 2.16 Silicon on PLZT Light Modulator

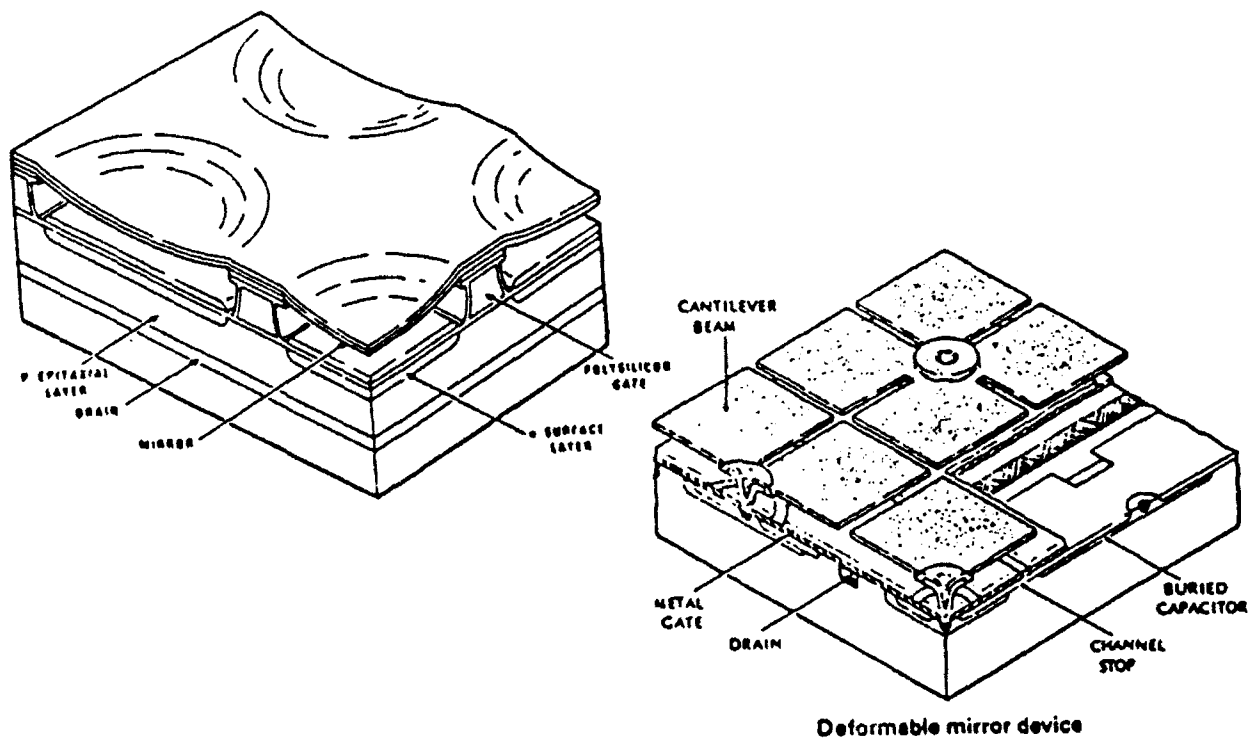


Figure 2.17 Deformable Mirror Device (DMD)

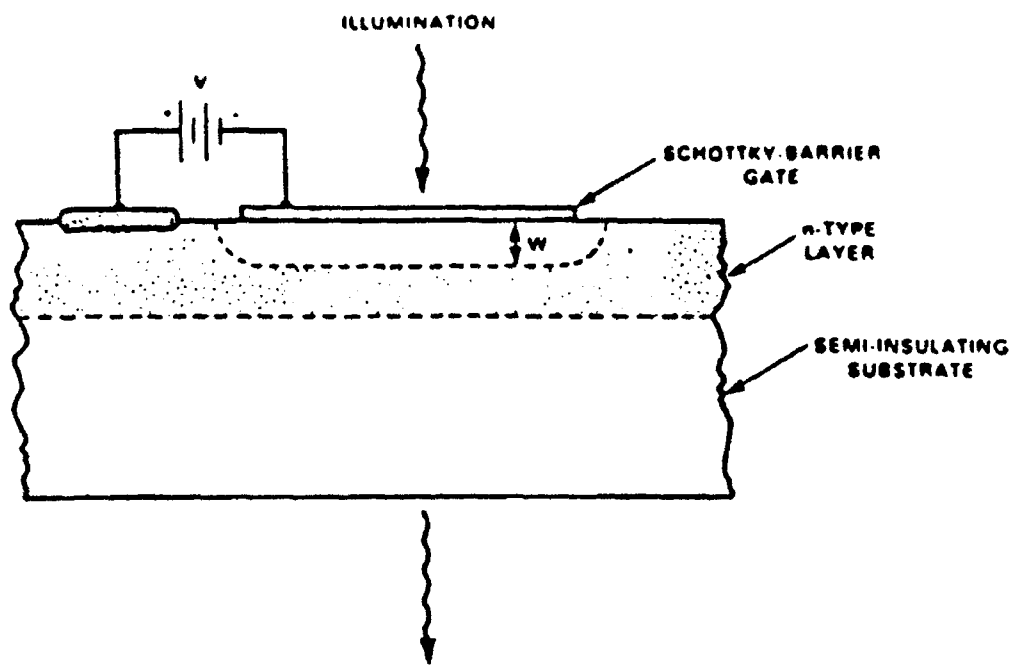


Figure 2.18 Charged Couple Device

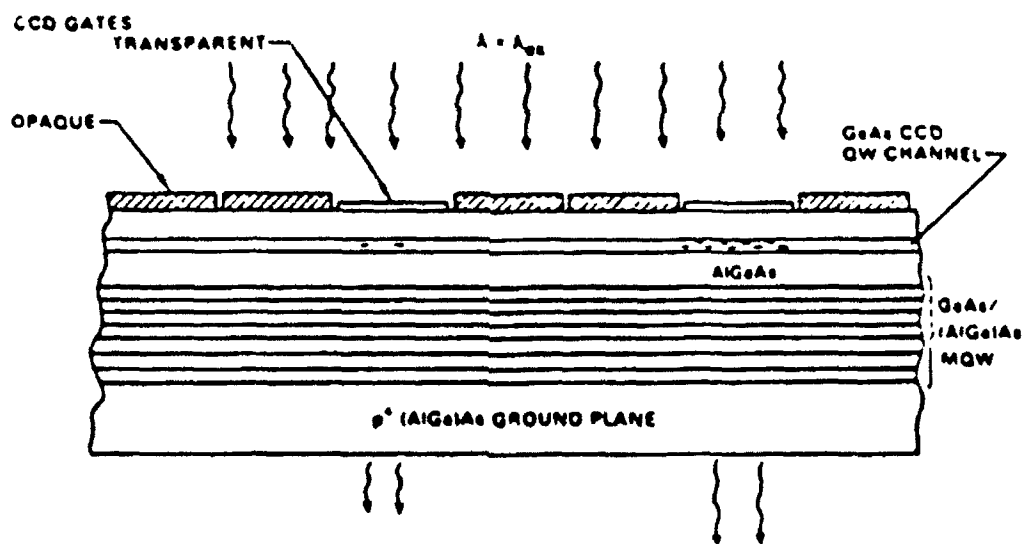


Figure 2.19 Cross Section of a CCD SLM Using a Quantum Well CCD Channel and an MQW Optical Modulator

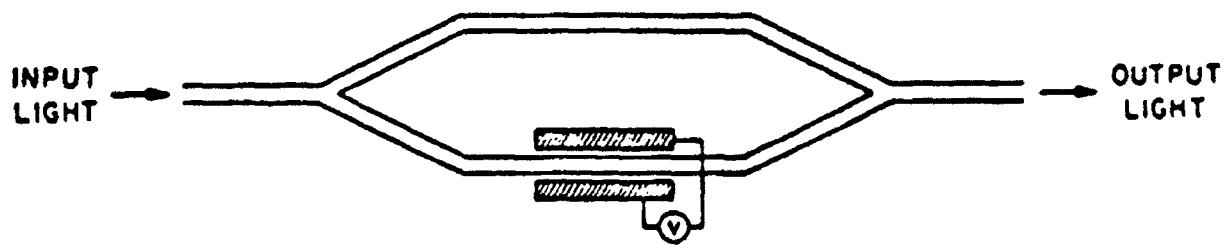


Figure 2.20 The Integrated Optical Implementation of the Mach-Zehnder Interferometer

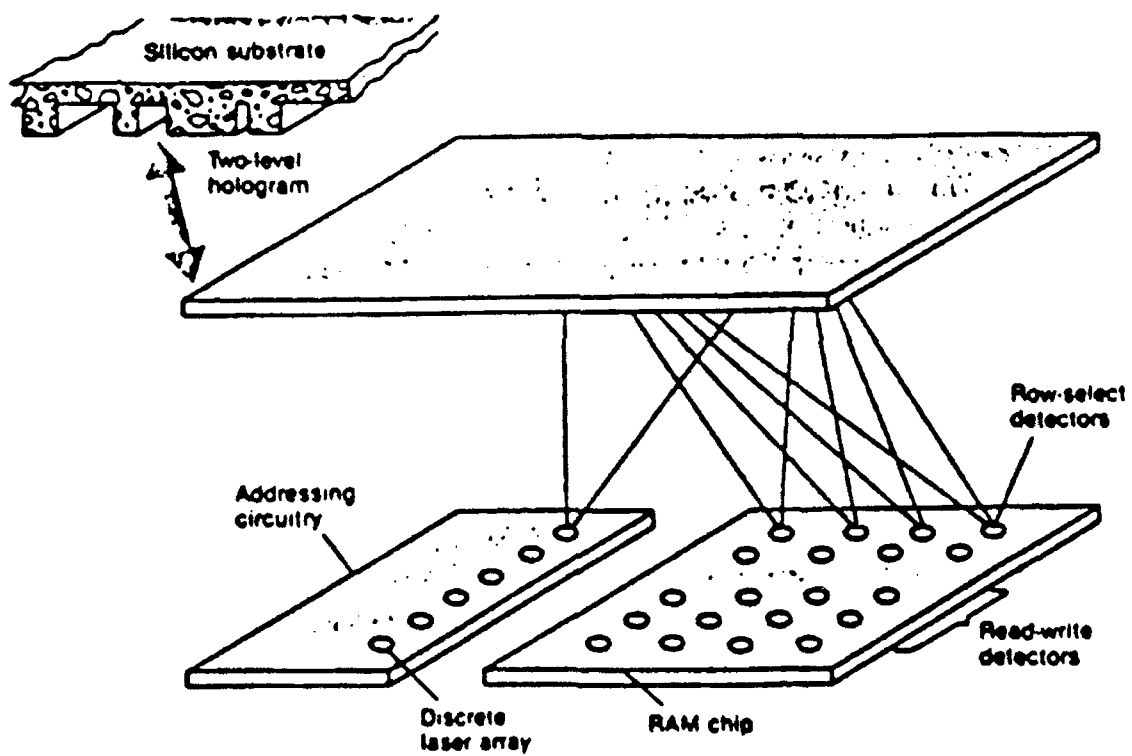


Figure 2.21 Hologram

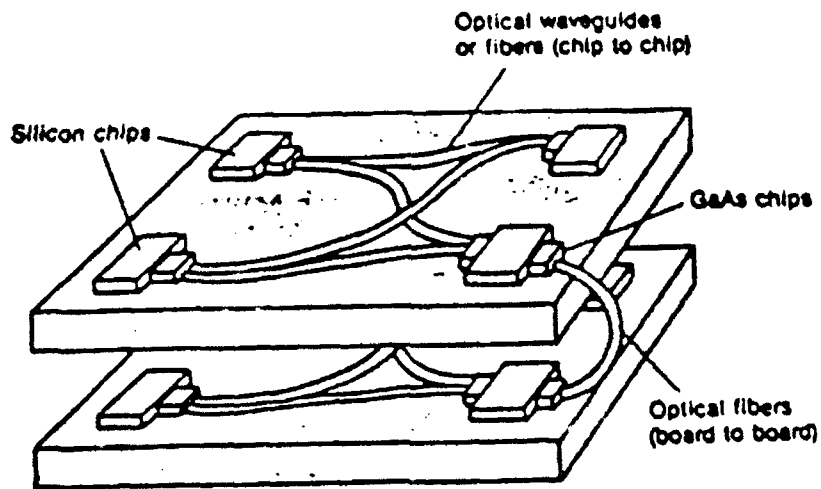


Figure 2.23 Device Interconnect

3. OPTICAL COMMUNICATION NETWORKS

3.1 INTRODUCTION

A significant increase in the use of personal computers, workstations, graphics workstations, mainframe computers, supercomputers, and a variety of data peripherals in recent years has prompted new challenging needs for communications among these devices. The services provided by the network that connects them vary from services that need slow bit rates (telemetry, modems, etc.) to those that need very high data rates (high definition television, human vision, etc.) as shown in Figure 3.1 [1]. It is clear from this figure that future communication networks require several order of magnitude increase in switching capability and provided throughput. In addition to the the high bandwidth requirement, future networks should support different types of connections (e.g., extensive point-to-multipoint, and data broadcasting) and should also be able to deal with various forms of multimedia messaging including data, facsimile, image. etc [2]. For example, The bit mapped multiwindow display on a 1000 x 1000 pixel workstation CRT shows a combination of full color pictures and alphanumeric text (shown in Figure 3.2). Such a display in bit mapping requires about 10^7 bits and in a compressed form can be done with perhaps 10^6 bits. Consequently, manipulation and refreshing of such pages require several megabits per second to accommodate only one user and this requirements will increase linearly with the number of users accessing the network to read/write material in this format.

Communications network topologies can be described in terms of several key generic elements as shown in Figure 3.3. In this figure, the end user denotes an

information source or sink that could be a terminal, a computer, a facsimile, or a TV set. The access channel connects the end user to the first routing or switching point. The paths after the switching points aggregate traffic from multiple end users to be routed and distributed using high speed transmission lines. Also, users send control signals so that particular communications session or call can be routed, prioritized or handled in a proper manner. Also, this figure shows the bandwidth requirements for each component to meet the network applications in the 1990's. Therefore, the operating speed of each key network component must be increased in several orders of magnitudes to meet the bandwidth requirements of the applications listed in Figure 3.1.

Network designers are increasingly limited by the switching capability of the network rather than the transmission capacity and this has generated an intense research interest to design networks that can route and switch messages at very high data rates (e.g. Gigabit or even Terabit rate). Optical switching systems are expected to play a key role in realizing future communication systems. From a functional point of view, a switching system is generally composed of switching networks and control circuits. There has been a steady progress in the development of optical devices for switching networks. The realization of optical control circuits is slower and needs further development in optical logic devices and optical memories. Figure 3.4 shows the main components of optical switching networks [7]. The characteristics of optical devices used in building the switching systems are discussed previously in section II.

3.2 CLASSIFICATIONS OF OPTICAL SWITCHING NETWORKS

The classification of optical systems presented in this section is based on that

proposed in Macdonal's paper [3]. This classification shown in Figure 3.5 is organized according to three different aspects: 1) the type of multiplexing; 2) the physical basis for the switching mechanism; and 3) the optical configuration.

3.2.1 Multiplexing

There are three types of multiplexing: space division, modulation division and carrier division.

Space Division. In this type of system, no common paths are used in routing the input signals to the output ports. They use switching elements that route optical carrier along a selectable path. Figure 3.6 shows a non-blocking Benes network that uses exchange-bypass switching elements. Small scale integrated optical switch networks have been demonstrated [10]. Current research addresses the design of *large networks that minimize loss and crosstalk* in larger integrated optical exchange-bypass networks [11].

Figure 3.7 shows a crossbar-based network that uses optical power divider and recombiner devices [12, 13]. The advantage of the crossbar architecture over the exchange-bypass architectures that the connection paths go through only one switching element. Consequently, loss and crosstalk do not accumulate with an increase in network dimension. Another advantage is that crossbar networks can provide multibroadcast and broadcast capabilities.

Modulation Division. In this method, the signals that modulate the optical carriers are multiplexed [8]. Time division multiplexing can be implemented using fast optical switching elements.

Figure 3.8 (a) shows a bus-based network that uses time division multiplexing in which one switching element is needed for each line. However, the input signal could pass through all the switching elements on the bus and that could lead to significant loss and reduction in reliability. A star-based network is shown in Figure 3.8 (b). In this type of network, broadcast capability can be supported and no more than two switching elements are traversed in sequence.

Carrier Division. In this method, the optical carriers are multiplexed such as frequency/wavelength multiplexing [9]. The carrier division-based networks require either wavelength division multiplex or tunable taps or filters, plus a distribution system that is not wavelength dependent. Figure 3.9 shows the basic configurations for bus and star-based networks with carrier division.

3.2.2 Switching

Signals can be carried out through the network in optical form for all or only part of the network. Consequently, the switching mechanism depends on the type of signal (optical or electrical). The switching mechanism can therefore be in three forms: 1) Optical switching: it accepts optical signals and yields optical signals; 2) Optoelectronic switching: it accepts optical signals and yields electrical signals or vice versa; and 3) Electronic switching: it accepts electrical signals and produces electrical signals. These types of switching devices are shown in Figure 3.10.

3.2.3 Optical Configuration

Since switching networks use optical power dividers and optoelectronic transducers, the location of the conversions of signal between optical and electrical forms

is important for network operation. Based on the location property, three configurations can be identified [3]: 1) Central configuration: in this configuration, the terminals are connected to the network electrically while optical inputs and outputs originate at the network; 2) Optically extended configuration: in this case, either the optical inputs to the network originate at remote sites, or optical outputs are sent directly to remote sites, or both; and 3) Distributed Systems: in this case, several terminals are connected to multiple access optical networks. These configurations are shown in Figure 3.11.

REFERENCES

- [1] Eric Nussbaum, "Communication Network Needs and Technologies--A Place for Photonic Switching?," *IEEE Journal on Selected Areas in Communications*, vol. 6, no.7, August 1988, pp.1036-1043.
- [2] S.B. Weinstein, "Telecommunications in the Coming Decades," *IEEE Spectrum*, pp.62-67, Nov. 1987.
- [3] D.L. Carney, J.I. Cochrane, L.J. Gitten, E.M. Press, and R.E. Staehler, "The SESS Switching System Architecture Overview," *AT&T Tech. Journal*, vol.64, part 2, pp.1339-1356, July-Aug., 1985.
- [4] A.S. Acampora, and M.J. Karol, "An Overview of Lightwave Packet Networks," *IEEE Network*, January 1989, pp.29-41.
- [5] A. Djupsjobacka, "Time Division Multiplexing Using Optical Switches," *IEEE Journal on Selected Areas in Communications*, vol.6, no.7, August 1988, pp.1141-1151.
- [6] R. Ian Macdonald, "Terminology for Photonic Matrix Switches," *IEEE Journal on Selected Areas in Communications*, vol.6, no.7, August 1988, pp.1227-1231.
- [7] M. Sakaguchi and K. Kaede, "Optical Switching Device Technologies," *IEEE Communications Magazine*, vol.25, no.5, May 1987, pp.27-32.
- [8] T.E. Darcie, "Subcarrier Multiplexing for Lightwave Multiple Access Networks," *Proc. Opt. Fibre Commun. Conf. (OFC)*, Reno, NV, 1987.
- [9] N.A. Olsson and W.T. Tsang, "An Optical Switching and Routing System Using Frequency Tunable Cleaved Coupled-Cavity Lasers," *IEEE J. Quantum Electron.*, vol.QE-20, 1984, pp.332-334.
- [10] P. Granstrand, et al, "Strictly Nonblocking 8 X 8 Integrated Optics Switch Matrix," *Electron. Lett.*, 1986, pp.816-817.
- [11] R.A. Spanke, "Architectures for Large Nonblocking Optical Space Switches," *IEEE J. Quantum Electron.*, vol.QE-22, 1986, pp.964-970.
- [12] A. Himeno, H. Terui, and M. Kobayashi, "Guided Wave Optical Gate Matrix Switch," *J. Lightwave Technol.*, vol.6, 1988, pp.3-35.
- [13] A. Ajisawa, et al, "Monolithically Integrated Optical Gate 2 X 2 Matrix Switch Using GaAs/AlGaAs Multiple Quantum Well Structure," *Electron. Lett.*, 1987,

pp.1121-1122.

- [14] Kay Y. Eng, "A Photonic Knockout Switch for High-Speed Packet Networks," *IEEE Journal on Selected Areas in Communications*, vol.6, no.7, August 1988, pp.1107-1116.
- [15] Paul R. Prucnal, and Philippe A. Perrier, "Self-Routing Photonic Switching with Optically Processed Control," *Optical Engineering*, vol.29, no.3, March 1990, pp.170-182.
- [16] F.B. McCormick et al., "All-Optical Shift Register Using Symmetric Self-Electro-Optical Effect Devices," Topical meeting on photonic switching, paper Thc5, Washington DC, 1989.
- [17] D. Miller, "Optoelectronic Applications of Quantum Wells," *Optics and Electronics News*, February 1990.
- [18] S.D. Smith, "Optical Bistability, Photonic Logic, and Optical Computing," *Appl.Opt.*
- [19] M. Schwartz, "Telecommunication Networks: Protocols, Modeling and Analysis," *Addison-Wesley*, 1987.

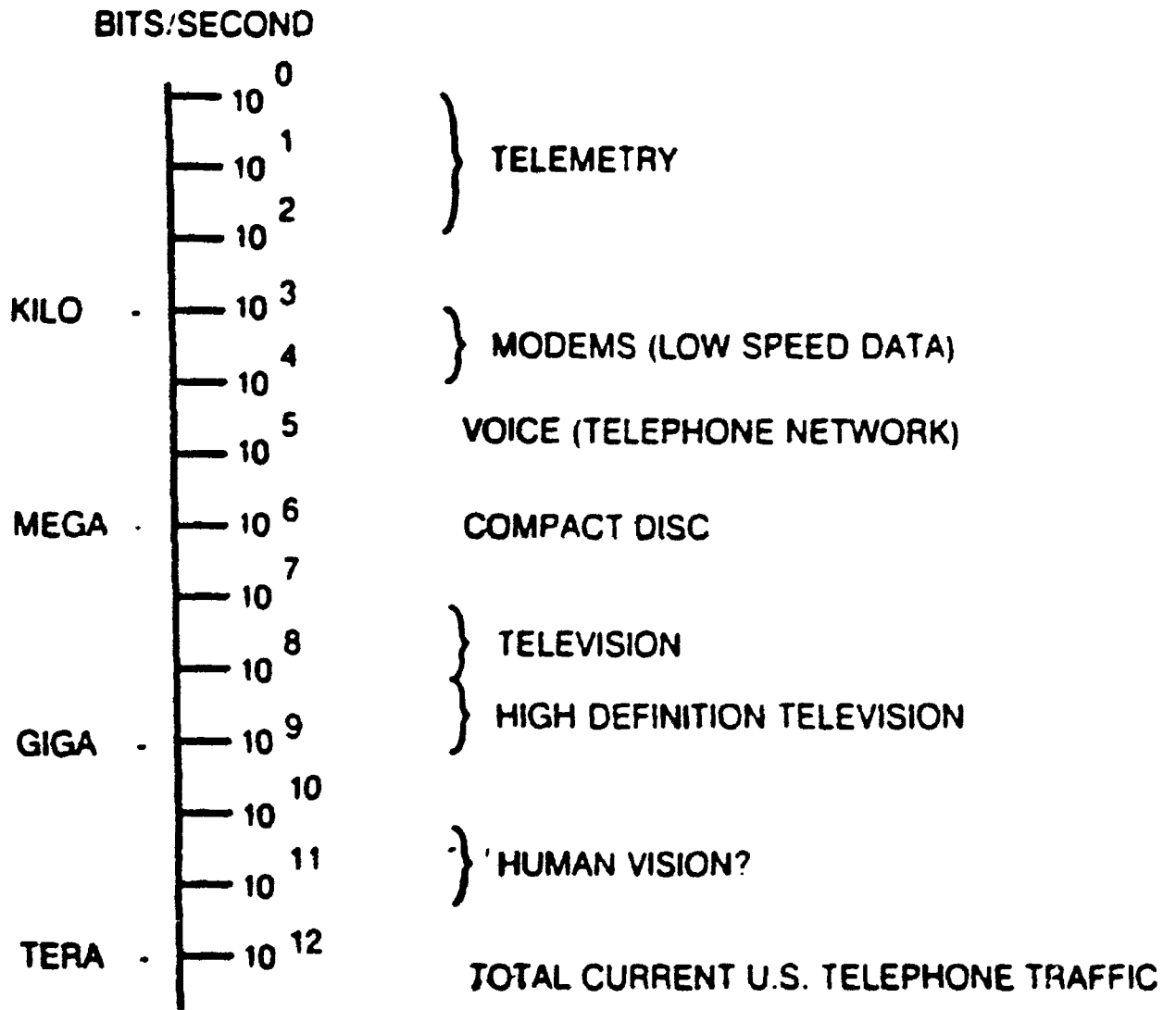


Figure 3.1 Information

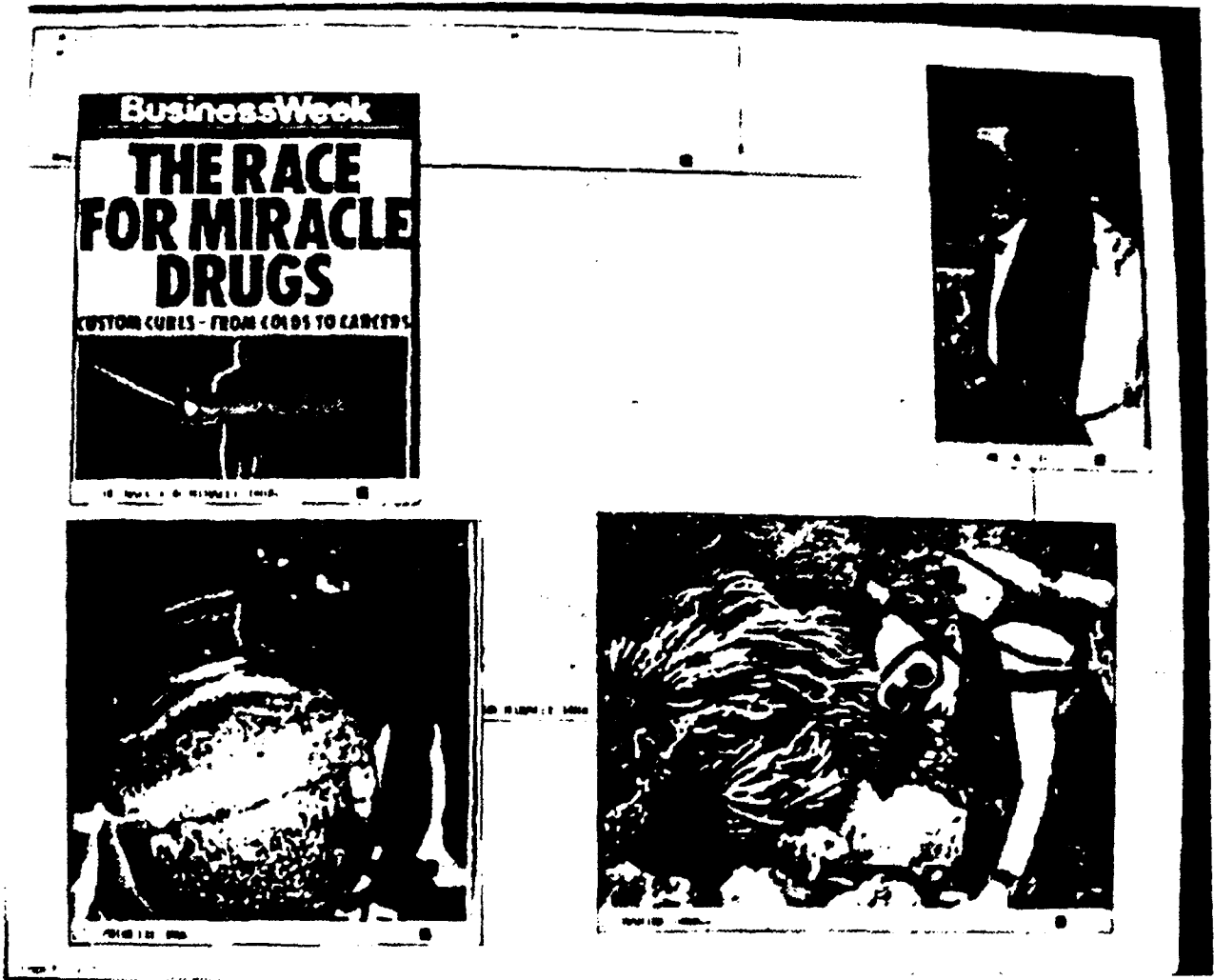


Figure 3.2 Bit mapped multiwindow terminal display.

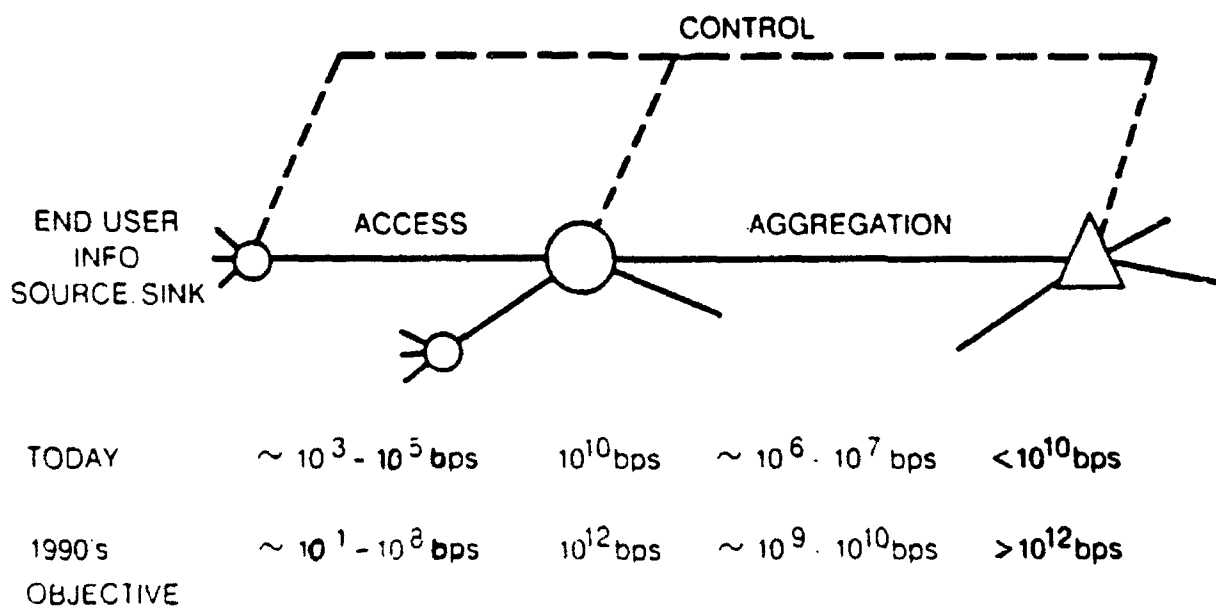


Figure 3.3 Key elements of a communication network.

OPTICAL DEVICES FOR OPTICAL SWITCHING SYSTEMS

Switching System	Optical Devices
Space Division System	Matrix Switches
Time Division System	Matrix Switches Optical Memories
Wavelength Division System	Wavelength Converters Wavelength Multi/Demultiplexers Tunable Optical Filters
Common for all the systems	Optical Amplifiers LDs/LEDs, PDs/APDs

Figure 3.4 Main components of optical switching networks.

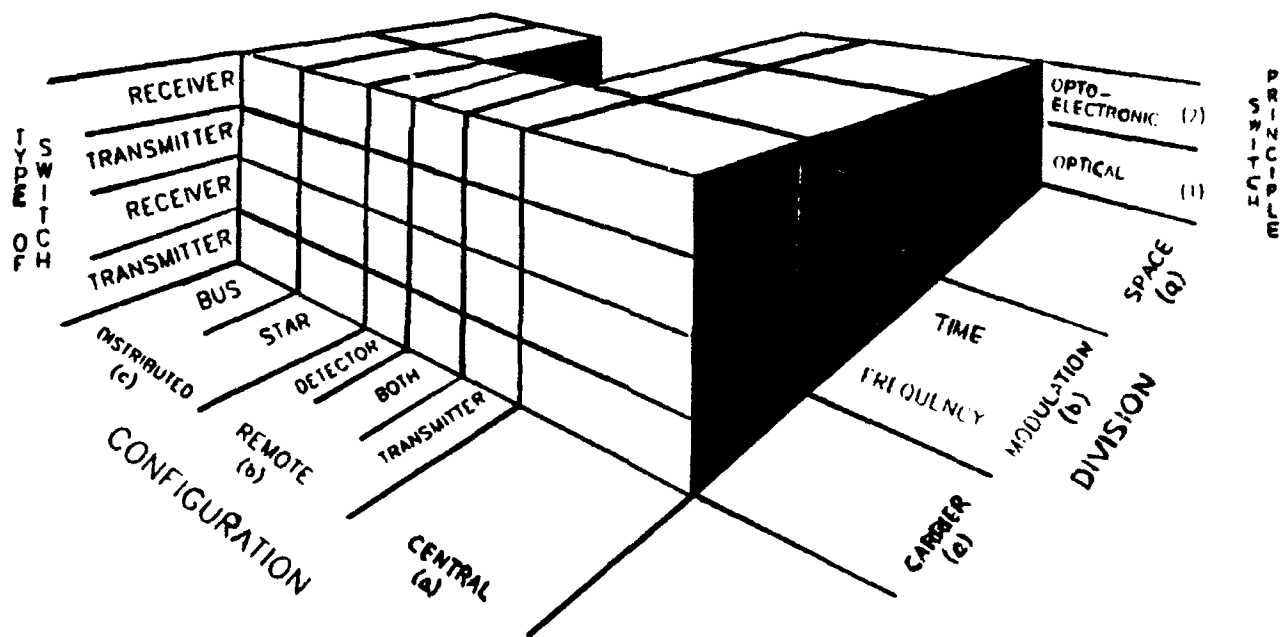


Figure 3.5 The classification considers three independent properties of photonic matrices, thus spanning a "volume." The physical basis of the switching mechanism is either "optical" or "optoelectronic." The internal multiplexing is in the "carrier," the "modulation," or in "space," and the placing of the electronic elements of the system provides the categories "central," "distributed," and "remote."

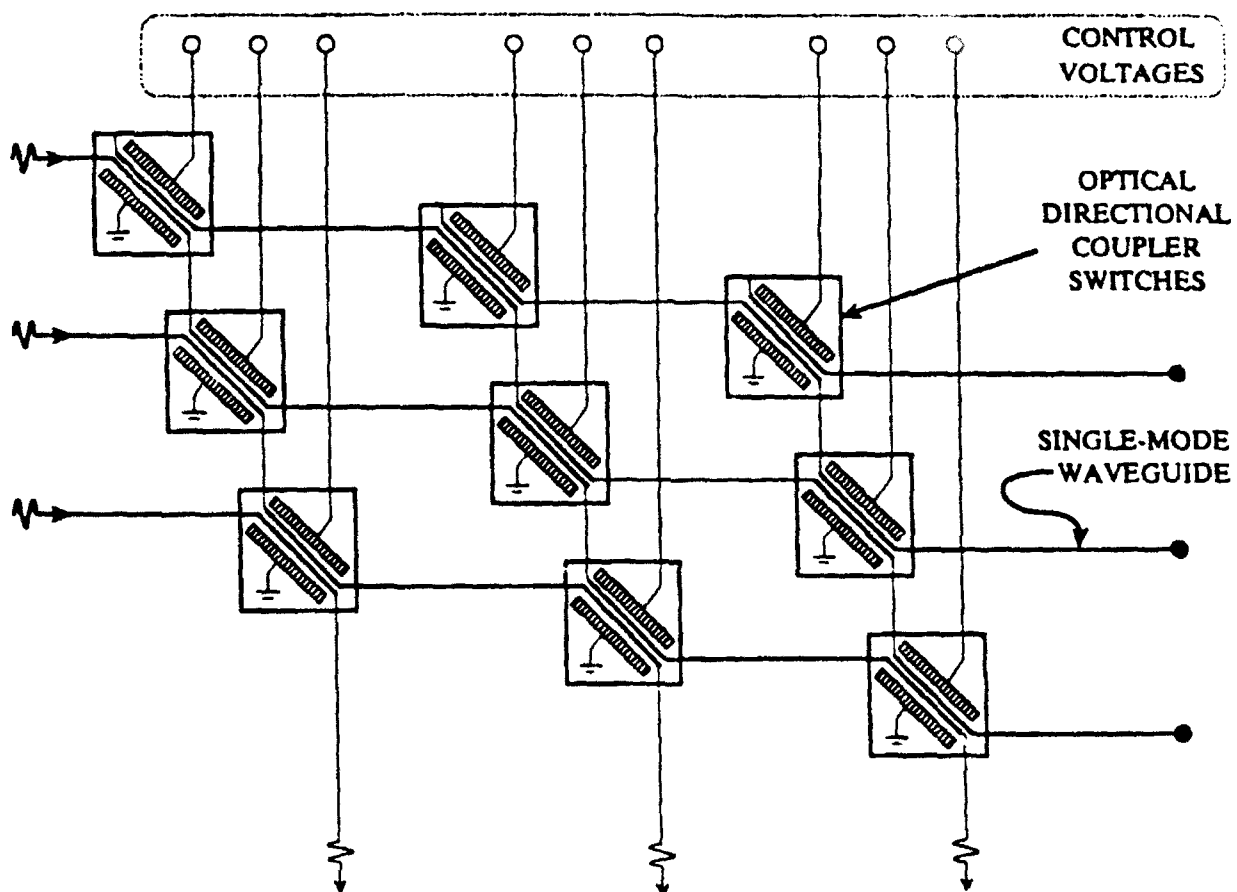


Figure 3.6 An optical exchange-bypass-based network.

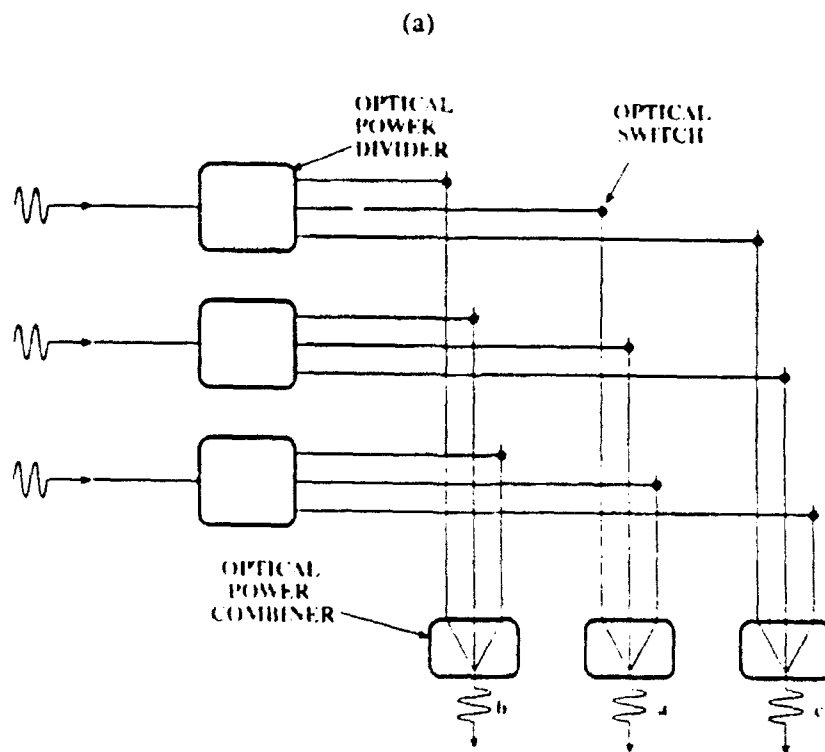


Figure 3.7 An optical cross-bar network.

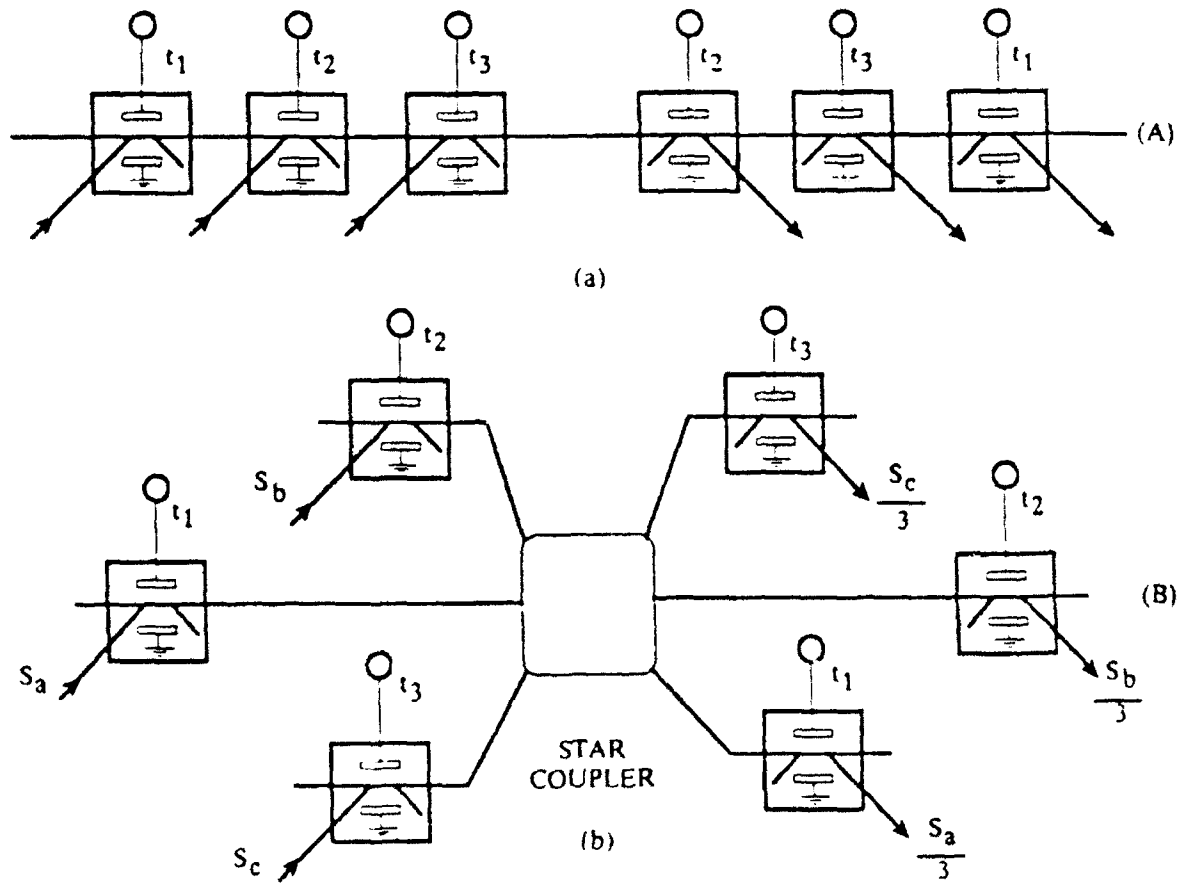


Figure 3.8 Modulation division. Optical time division networks: (a) Bus. (b) Star

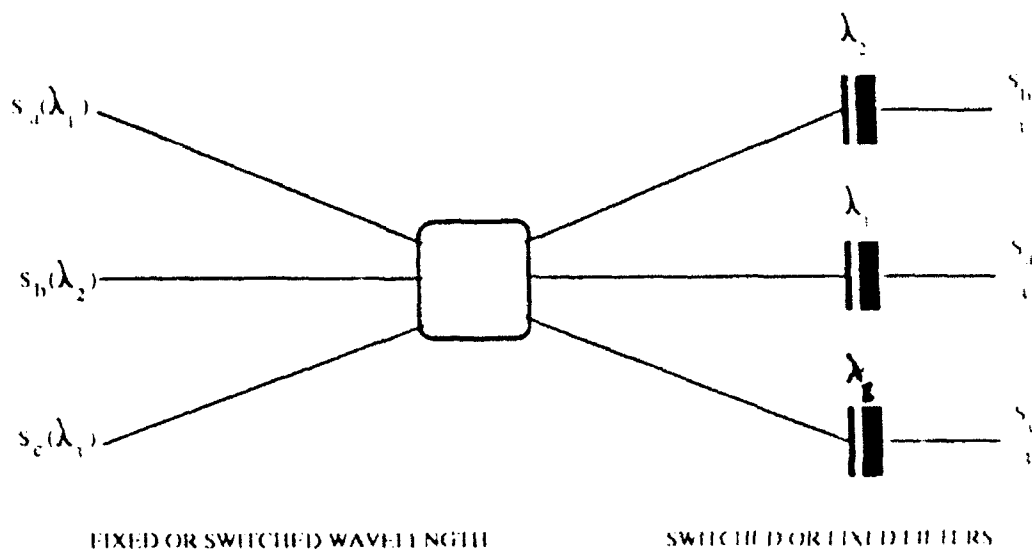


Figure 3.9 Carrier division networks:
Optical wavelength division-bus and star networks.

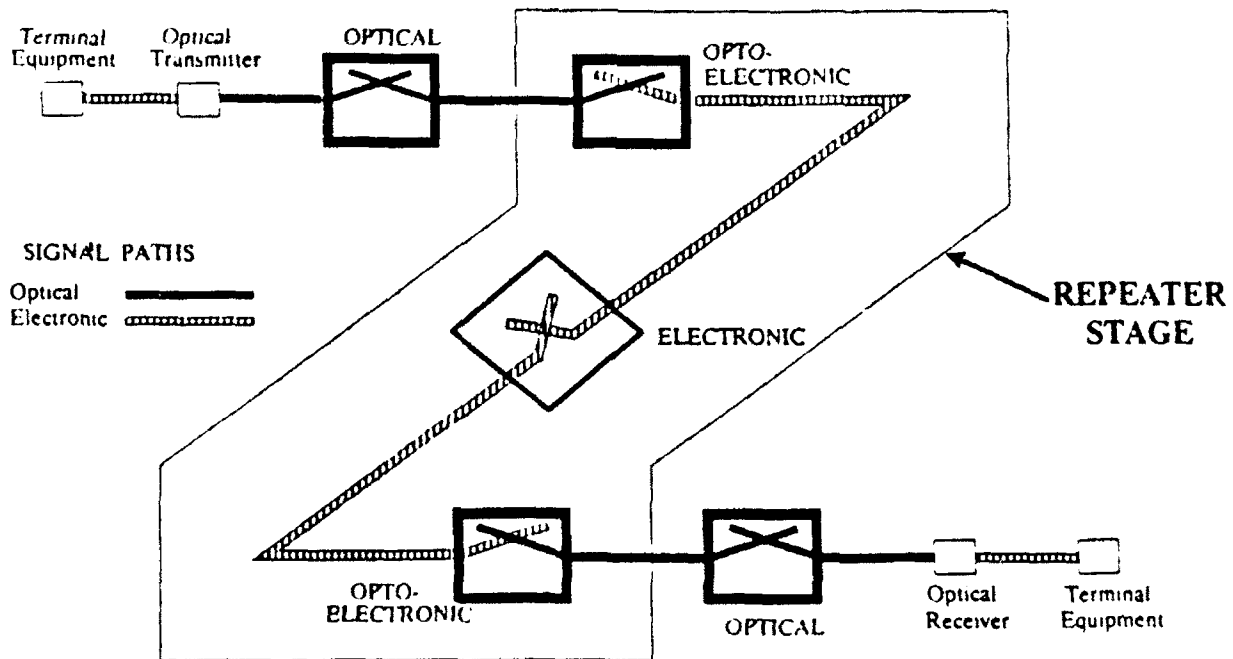


Figure 3.10 Switching principle: both optical and electronic signals are present in photonic systems, and signals can be switched in either form, or switching may occur in the optoelectronic conversion between the two forms. Electronic switching is not considered here.

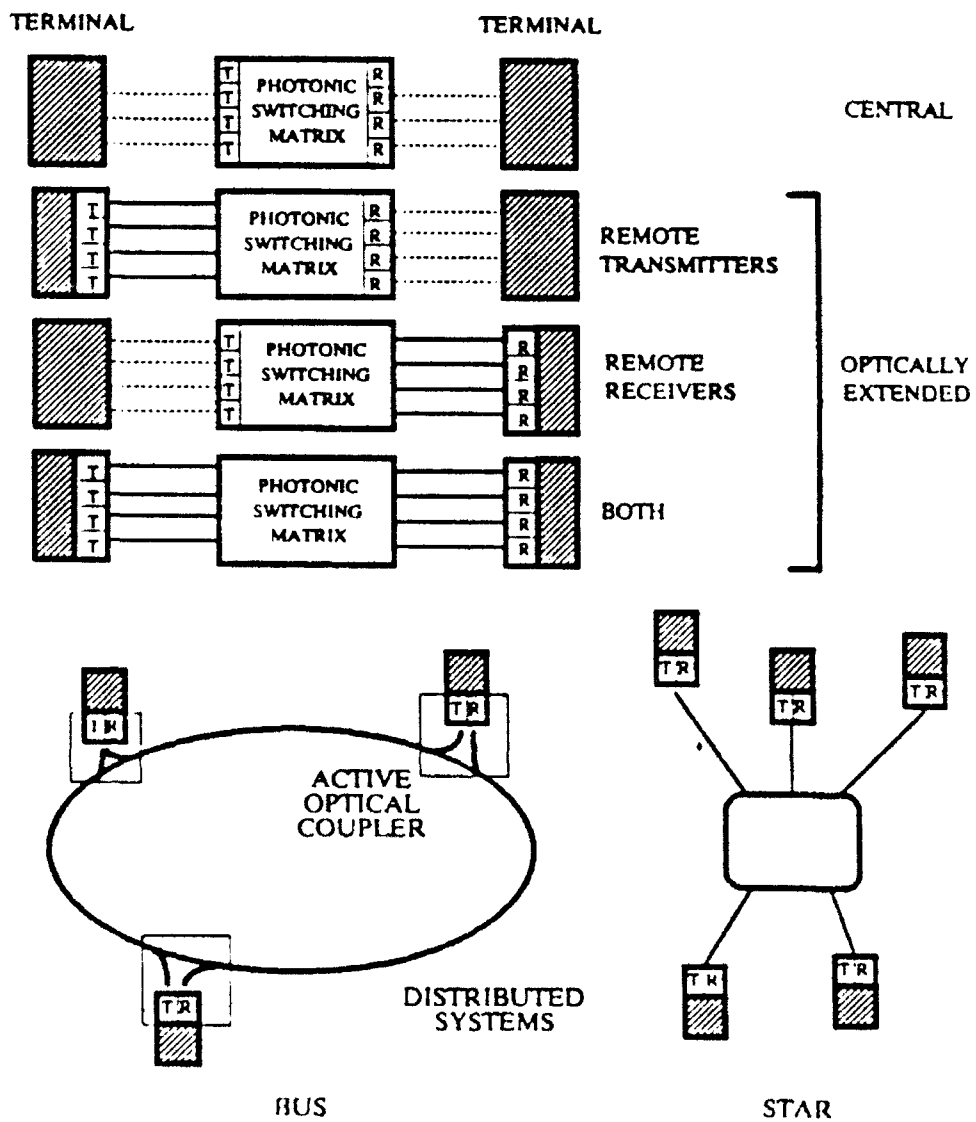


Figure 3.11 Optical System Configuration.

4. DESIGN AND ANALYSIS OF AN OPTIMP

4.1 INTRODUCTION

The current trend in local area networks is toward higher communications bandwidth as we progress from Ethernet networks that operate at 10 Mbit/sec to higher speed optical networks that will soon operate at Gigabit/sec rate. The design of such high speed optical networks will eventually be limited by the processing capabilities of the nodes that perform the required routing and switching functions in the electronics domain. Furthermore, the low-transmission bandwidth of the electronic switches, and the (O/E) and (E/O) conversions present an obstacle to fully exploit the large bandwidth offered by fiber optics.

Currently, intensive research is focused on removing the Optical-to-Electrical (O/E) and Electrical-to-Optical (E/O) conversion bottleneck by proposing design alternatives to achieve transmission as well as switching in optical technology.

Optical technology is still in its infancy and its capability to perform complex routing and switching functions lags behind what can be done using electrical technology. This has led to designing of hybrid networks in which the routing and switching functions are performed using electrical devices while the transmission function is carried out using fiber-optics as in the Overlay Network [1]. Other optics networks use time-division and wavelength-division multiplexing to design photonic switches to route optical signals from their input ports to their corresponding output ports [2, 3, 4]. Self-routing photonic switching with optically processed control is proposed in reference [5], where packet headers are encoded with packet destination addresses using either optical code-division

or time-division encoding techniques.

The design approaches discussed above implement the routing and switching functions using either electronic devices or analog devices such as filters, optical summing circuit, and optical receivers. The *former approach* suffers from the **conversion bottlenecks** while the main limitation of the *later approach* is its **sensitivity** to any small change in the characteristics of its analog devices.

We emphasize that the designs of systems, switches and networks that are based on electronics technology may not be feasible and/or efficient when optical technology is used; the same design is used by replacing electronic devices by equivalent optics devices. Thus, we investigate alternative designs which fully exploit the inherent parallelism and multidimensionality offered by optics. In OPTIMP, the routing function is deterministic and all source-destination pairs are stored in a look-up table as well as the control signals needed to configure the interconnection network. The table is searched in parallel to find the column that has all the control signals needed to route an incoming packet/message to its destination. This design is similar to the design of the microprogrammed control unit of a processor where the microinstruction code corresponds to the source-destination code in OPTIMP.

The rest of this chapter is organized as follows. Section 2 presents our design approach. A functional description of OPTIMP architecture is presented in Section 3. Section 4 briefly describes the power requirements as well as presents analytical performance results for OPTIMP based on the current technology. Finally, conclusions, current status and future research is outlined in Section 5.

4.2 DESIGN APPROACH

The microprogrammed concept that is widely used to design computer's control units has been adopted to design *OPTIMP* because it simplifies the routing and switching functions. In *OPTIMP*, all source-destination (SD) pairs are stored in a look-up table. For each SD code, the table indicates the outgoing channel to be used in routing the incoming packet to its destination. The contents of this routing table can be stored on an optical mask (e.g., holograms, spatial light modulators, etc.). Most of the time, the topology of a network is fixed. However, infrequent changes can be made in the routing table which may be required due to congestion or link failures. This design takes advantage of the capability of optics to perform parallel search (single step search) on a two-dimensional optical array (routing table) as well as the high density storage capability of optics. In addition to storing the SD pairs, this table stores the control signals required to setup the optical switching devices. Consequently, this will simplify the generation of control signals in real-time needed to route an incoming packet to the appropriate output port.

Figure 4.1 shows an example of a communication network connecting several high performance computers. Consider the path to be used to transport one packet (or a message) from computer HPC-1 to HPC-2. The routing table associated with an Interface Message Processor IMP_1 routes every incoming packet with $SD=HPC-1:HPC-2$ to link L_3 , while IMP_2 routes that packet to link L_4 , and so on until IMP_6 that delivers it to the destination computer HPC-2 through L_{10} . The routing table information may need to be modified infrequently to reflect the new status of the communication subnet. For example, if L_8 fails, the routing table of IMP_4 should be updated to route a packet with

SD=HPC-1:HPC-2 to L_7 instead of L_8 . Furthermore, the routing table of IMP_5 should also be modified to route that packet to L_9 where it is delivered to HPC-2 through L_{10} .

The routing function of the OPTIMP can be implemented using either a centralized or distributed scheme as shown in Figures 4.2 and 4.3, respectively. Figure 4.2 shows a block diagram of an OPTIMP with m incoming fiber-in ports and n outgoing fiber-out ports. The unit functions on a first come first serve base. When a packet is received at one of the input ports as a sequence of optical pulses, the other input channels are temporally disconnected until the routing of the first come signal is complete. The optical power divider routes one copy of this packet to the Time-Space Converter (TSC) unit and another one to the Delay Line Unit. The TSC extracts only the source-destination SD information from the packet header and stores it on a one-dimensional S-SEED array-based optical shift register. This process converts the incoming sequential SD code from time domain to spatial domain, such that the SD code can be read out in a parallel manner. Now, a parallel search on all the columns of the routing table in the Optical Microprogrammed Routing Unit (OMRU) is performed to select the column corresponding to the given SD code. The selected column triggers an image pattern required to configure the Optical Switching Network (OSN) so that the incoming packet can be routed to the proper fiber-out port. The function of the delay line unit is to delay connecting the incoming packet to the OSN until the OMRU has configured the OSN.

Conflicts can occur when an incoming packet can not be routed to its output ports without interrupting the existing connections in the switching network. When an incoming packet is selected, its control signals needed to route it to its destination are read out from

the routing table. These control signals are then compared with those that are currently configuring the OSN. An incoming packet is routed to its output port if and only if the superimposition of its control signals with those that are currently active do not lead to a conflict in setting the OSN and/or the output port is busy. If there is a conflict, the packet can be either delayed or discarded.

Figure 4.3 shows a block diagram of OPTIMP implemented based on a distributed routing scheme. In this approach, there is one OMRU to each output port. The OMRU design is simplified because of limiting its switching capability to only decide whether or not the selected packet can reach its destination through the output port controlled by this OMRU. However, since the beam splitters distributed each incoming packet to all ISUs, this rejected packet will be routed through another OMRU. Therefore, a packet will be delayed or rejected only if all the ISUs are busy simultaneously and if the selected output port is busy.

4.3 ARCHITECTURE

As we discussed in the previous section, the operation of the OPTIMP consists of several steps: time domain to spatial domain conversion, parallel routing table look-up and control pattern generation, and configuration of optically controlled interconnection network. To achieve a non-blocking operation, a delay of the input data stream is also needed. In the following, we will discuss the optical implementation of each of the functional unit. For simplicity, most of the light guiding elements, such as mirrors, cylindrical lenses, and beam splitters are omitted. Also, only the main functional modules of OPTIMP are shown and details are omitted.

4.3.1 Time Domain to Space Domain Conversion of SD Code

The input source and destination (SD) code from the incoming fiber is first converted from time domain to spatial domain (for the SD code only). The purpose of time to spatial domain conversion is that we can then use the parallel processing advantage of optics to achieve real-time and high-speed routing table search.

As shown in Figure 4.4, the Trigger pulse in the input packet activates the Optical/Electronic Converter and Clock Trigger, which starts and synchronizes operation of the unit. The SD code (header) is separated from the input data packet by a time domain AND gate and stored in an S-SEED array-based optical shift register [6], which is composed of k -number of S-SEED's connected in tandem. The high-speed (on the order of ps) and low energy (on the order of fJ) symmetric self electro-optic device (S-SEED) [7] has drawn a great deal of attention because of its advantages for optical computing. Each of the S-SEED in the array functions as an optically addressed set-reset flip-flop. The intensity ratio between SET and RESET determines the state of the flip-flop. Because of this property, the register is not susceptible to light intensity fluctuations of the system. The time domain input SD code from fiber-in port shines on the input port. With the synchronization of the clock pulses, the SD code will propagate through the shift register and thus be stored on it. The bit length of the register (k) is determined by the bit length of the SD code. Notice that since each of the S-SEED based flip-flop produces dual outputs, both the SD code and its complement code \overline{SD} are stored on the shift register simultaneously. After the SD and \overline{SD} have been stored on the shift register, a

fine-tuned polarization-sensitive imaging system will be able to read out the SD and \overline{SD} codes in a parallel manner and display the codes separately on spatial domain. This completes the time domain to spatial domain conversion. One of the important properties of the shift register is its time sequential gain. In other words, after the SD and \overline{SD} codes are stored, they can be read out by strong beams of light in a parallel manner. Therefore, the output of the time domain to spatial domain converter can provide enough power for the following operations. Since the S-SEED can operate at a rate above Gigabits/s [7], the above discussed domain conversion for each bit of the SD and \overline{SD} code can also be in the range of Gigabits/s, which is the current data rate for fiber communications.

4.3.2 Parallel Routing Table Search

The optical implementation of the optical microprogrammed routing unit (OMRU) is shown in Figure 4.5. The SD code and its complement \overline{SD} are displayed in spatial domain on the outputs of the one dimensional shift register as SD and \overline{SD} , respectively. Here, we use positive logic (i.e, a binary one is represented by high intensity and a binary zero is represented by low intensity). The routing table (RT) and its complement (\overline{RT}) are displayed by two binary-type programmable spatial light modulators (SLMs), respectively. According to the predetermined routing table, a pixel on a SLM is transparent (if it is a binary one) or opaque (if it is a binary zero). Each SD code of the routing table is designated by a column of pixels on the RT. In other words, a k by n pixel RT can represent n sets of SD codes with the length of each one

being k . Although the achievable frame rate (to update the routing table) of SLM is in the order of microseconds, we stress that during normal routing operations, the patterns displayed on the SLMs (routing table entries) do not need to be changed. To read these patterns by light beams takes less than a nanosecond (10^{-9} sec. for light to travel a few centimeters). Therefore, the relative slow writing speed of the SLM does not limit the performance of the system in normal operation.

The parallel routing table look-up is based on a vector-matrix multiplication scheme. The cylindrical optical system (not shown in the figure) spreads each bit on the S-SEED array-based shift register into a horizontal row that illuminates a corresponding row in one of the SLMs. In this manner, the input SD and its complement codes represented by two columns of intensity distributions are simultaneously multiplied by each column in the routing table RT and its complement \overline{RT} , respectively. A beam combiner (symbolically shown in the figure) combines the results of the two sets of bit multiplications. The following cylindrical lens (not shown in the figure) focuses each column of the bit-by-bit multiplication results onto a pixel in the one-dimensional thresholding device TH. In terms of linear algebra, the total light intensity behind each column in the routing table RT is the inner-product between input SD code and a routing code, and the intensity behind each column in \overline{RT} is the inner-product between the corresponding complement codes. After beam combination and then focusing in the column direction, the intensity on the corresponding pixel of the one-dimensional thresholding device is expressed by Boolean function:

$$\sum_{i=1}^k (SD)_i \cdot (RT)_{ij} + (\overline{SD})_i \cdot (\overline{RT})_{ij} = \text{Equivalence}; j=1,2,\dots,n$$

where $(SD)_i$ is the i th bit of the SD code and $(RT)_{ij}$ is the corresponding element in the routing table RT.

The maximum of the Equivalence function determines the best match between the input SD code and one of the columns on the routing table. To be specific, if the input SD code matches the first column in the routing table, the total light energy passing the first column on the RT and \overline{RT} will both be a maximum (i.e., $j=1$). Upon adding them together by the beam combiner and cylindrical lens, the total energy on the first pixel of the one-dimensional thresholding device TH that corresponds to these two columns is its maximum possible value.

4.3.3 Control Pattern Generation and Signal Delay

The intensity thresholding behavior of the TH is properly set such that a pixel transmits light through it only if the total intensity impinging on it is above a predetermined value. Hence, there will be only one pixel on the device to be transparent. This pixel indicates the result of the parallel table search (destination search). A number of nonlinear thresholding etalons are available [8]. Since the process is based on energy operation (i.e., incoherent optical operation), it has no requirement for the wavefront quality and phase relationship for the clock pulse laser source. This results in a design with better flexibility and lower cost.

To insure accurate table search, the SD codes and the routing codes have to be properly designed. Each column in the routing table must be able to transmit equal

amounts of light intensity, and the added results on the one-dimensional thresholding device TH must be sufficiently different so that the TH can make a correct decision. The cylindrical optical system (not shown in the figure) behind TH, expands the light transmitted through the pixel, which provides Destination Estimate, in column direction to illuminate a corresponding column in the control table CT. This selected column is imaged onto the output plane to provide a binary control pattern for the optically controlled OSN.

To achieve non-blocking real-time routing, the input data needs to be delayed until the control signals are generated and the optical switches are set appropriately. Since the routing table look-up and switching unit configuration only need the time on the order of nanoseconds, the delay lines in OPTIMP can be realized by means of optical fibers of finite length.

4.3.4 Switching Network

The last functional module in the OPTIMP is the optically controlled optical switching network. Figure 4.6, shows a light controlled S-SEED array-based OSN. As we have discussed above, an S-SEED device can function as an optically controlled light switch that changes the intensity reflectance of the pair of the connected SEED's according to the intensity ratio of the two impinging control (binary) beams. For simplicity, let's consider a two by two switching system. If the control pattern intensity on SEED number one is high and on SEED number 2 is low, the number 1 will have high absorption (i.e., "off" state) and the number two will have very low absorption (i.e., "on" state); therefore, the input data from BS1 will be directed to output port 2. On the

other hand, if the control pattern intensity is low on SEED number 1 and high on SEED number 2, the input data from BS1 will be routed to output port 1. The same applies to the other pair of SEED's (number 3 and 4) and BS2 in Figure 4.6. Based on the same principle, if the control pattern has more pixels, more S-SEED elements can be controlled in the switching network. In other words, each of the elements in the array is individually switched "on" (high reflection) or "off" (low reflection). By doing so, any input port can be connected to any of the output ports. Since S-SEED fabrication is based on molecular beam epitaxy (MBE), the number of S-SEED elements on a chip can be, in theory, very large. The control patterns can be imaged onto the S-SEED array by a refined optical imaging system. Thus a very high density high speed crossbar or multistage network can be achieved.

4.4 PERFORMANCE ANALYSIS

4.4.1 Energy Requirements

The parallel routing table look up is essentially a vector-matrix multiplication. If there are n output addresses on the routing table, each bit of the input SD code will be divided into n parts in order to perform parallel search. Therefore, the energy efficiency can reach $1/n$ in the best case. This energy is further divided by n^2 to set an $n \times n$ S-SEED array of the optical switching network (OSN). However, since the S-SEED can provide time-sequential gain, the energy loss can be compensated by a stronger reading light pulse after the S-SEED array shift register is set by the time domain input SD pulses. In other words, given the power requirements for the control beams to set the S-SEED array based OSN, one can calculate the requirement of the reading pulse intensity

for the S-SEED based shift register. For example, if each element in the OSN SEED array needs 10 fJ per nanosecond, the power required for each of the elements is 10^{-5} W. An n by n element OSN will need $n^2 \times 10^{-5}$ W. To achieve this required power out of the OMRU unit that has an efficiency of $1/n$, the total illumination power for the OPTIMP unit should be $n^3 \times 10^{-5}$ W. Therefore, for a 100 output OPTIMP, regardless of the number of input ports, the total illumination power is $100^3 \times 10^{-5} = 10$ W in pulsed mode. This is not difficult to achieve. With the improvement of pulsed laser source, the number of interconnections can be further increased. We emphasize that the time sequential gain of the S-SEED device is fully exploited to provide the required optical illumination power. That is, when the S-SEED based shift register has stored the input SD code, the illumination laser emits a strong reading pulse to read out the SD and \overline{sd} codes simultaneously, to perform parallel search, and to set the S-SEED array based OSN. Subsequently, the input data is routed through the unit to the required output port.

4.4.2 Static Response Time of OPTIMP

The processing time (response time), the delay in recognizing the SD code and setting a switch under no conflicts, of OPTIMP is the sum of the time needed in each functional component. If the time required for setting S-SEED element is τ_s (normally can be smaller than 1 ns), then the time for time domain to spatial domain conversion for a k bit SD code is $k \times \tau_s$. If the entire system (OPTIMP) is 30 cm. long, the time for parallel search and control pattern generation is $\tau_p = 30/c = 1$ ns, where c is the speed of light. The time response of the threshold nonlinear etalon can be smaller than 4 ps [8]

and thus can be neglected in our current system. Finally, the time to set the S-SEED OSN is less than 1 ns. Hence, to route an input data packet with SD code k -bit long, the total set-up time is $(k + 1) \tau_s + \tau_r$. For example, for $k = 8$ (representing total 256 outputs), the total response time to set-up the switch is about 10 ns. This assumes that S-SEED's response time is 1 ns. In practice it can be smaller than 1 ns.

4.4.3 Analysis of Packet Transmission Time

In this section, we analyze the packet transmission time (T_{trans}) between two consecutive OPTIMPs. If we know the average number of hops needed for a message or a packet to move from one source computer to a destination computer, the total end-to-end delay can be easily evaluated by multiplying the number of hops by the packet transmission time evaluated here. We will analyze the performance of OPTIMP design with distributed routing shown in Figure 4.3. and for three different transmission rates (10, 100, and 1000 Mbps). In this design, the newly arriving packet (message) is distributed to all the m inputs of OPTIMP. For each output port, there is only one *OMRU* responsible for routing packets through that port. Each *OMRU* periodically examines the packet at the top of the input queue for each input to see if that packet can be routed through its output port. If the packet can not be routed, it is discarded. However, since this packet has been routed to all the inputs, one *OMRU* will eventually route that packet through its output port. We refer to this time as (t_p) and it denotes OPTIMP response time. In the previous subsection, we discussed OPTIMP response time and was shown to be around 10 ns. In this design, an Optical Shift Register is used to periodically select one packet available at each input. Consequently, a newly arriving packet has to wait until its

turn comes to be examined by OPTIMP (packet access delay) before it can be transmitted through an output port. Hence, T_{trans} can be evaluated as the summation of the packet access delay t_{acc} and the packet transfer time t_{pkt} , i.e., $T_{trans} = t_{acc} + t_{pkt}$

Figure 4.7 shows a queueing model for the operation of an $m \times n$ OPTIMP. In this model λ_i denotes the packet arrival rate at input i , and μ denotes the service rate of OPTIMP to route a packet to its output. The output port access mechanism in OPTIMP is similar to that of the roll-call polling technique discussed in [9]. If we assume identical Poisson arrival rates at each input, the same packet-length statistics, and identical probability for routing a packet through an output port, then t_{acc} can be evaluated as

$$t_{acc} = \frac{1}{3} \frac{m \times t_p}{1 - \lambda \times t_{pkt}} (1 - \lambda \times t_{pkt}) + \frac{m \lambda \times \overline{t_{pkt}^2}}{2(1 - m \times \lambda \times t_{pkt})}$$

Here $\overline{t_{pkt}^2}$ is the second moment of the packet length, in (sec²). The first term in the above equation denotes the delay incurred by a packet until its input is selected. The second term denotes the time needed to transfer all the packets in front of the newly arriving packet in the queue. This term is the same as the waiting time in an M/G/1 queue. If we assume a fixed length packet, t_{acc} is given by

$$t_{acc} = \frac{1}{2} \frac{m \times t_p}{1 - \lambda \times t_{pkt}} (1 - \lambda \times t_{pkt}) + \frac{m \times \lambda \times t_{pkt}}{(1 - m \times \lambda \times t_{pkt})}$$

Since the input queue buffer (N) is finite, the packets could be rejected whenever the input buffer is full. To calculate the probability of blocking P_B , we note that packets transferred to the next OPTIMP node may in turn be blocked with the same probability

P_B (homogeneous network). This corresponds to requiring each packet an average $\frac{1}{1-P_B}$

retries before finally being transmitted successfully [9]. If we use the results of finite M/M/1 queue, the probability of blocking can be computed as

$$P_B = \frac{p'^N (1-p')}{(1-p'^{N+1})},$$

$$p' = \lambda \overline{t_{pkt}},$$

$$\overline{t_{pkt}} = \frac{t_{pkt}}{1-P_B}$$

The effective access delay and packet transfer time can be computed using the above equations by replacing t_{pkt} by $\overline{t_{pkt}}$.

Figures 4.8, 4.9 and 4.10 show the packet transmission times versus the average arrival rates of packets (of 16 Kbytes each) for 10, 100, and 1000 Mbit/sec medium data rates, respectively. In these figures we assume the size of the switch to be 256 x 256. From Figure 4.10, each input port of OPTIMP can process and route on the average 6000 packets/sec in less than 0.2 ms. The 256 x 256 OPTIMP switch can sustain a throughput of $256 \times 6000 \times 16 = 24.5$ Gbytes/Sec, with an average packet delay of approximately 0.2 ms.

The average transmission time does not change significantly when the size of the switch increases from 32 x 32 to 256 x 256 as shown in Table 4.1. This is because of the low processing overhead of OPTIMP (in order of nanoseconds) as compared to the transmission time of a packet for a given medium speed.

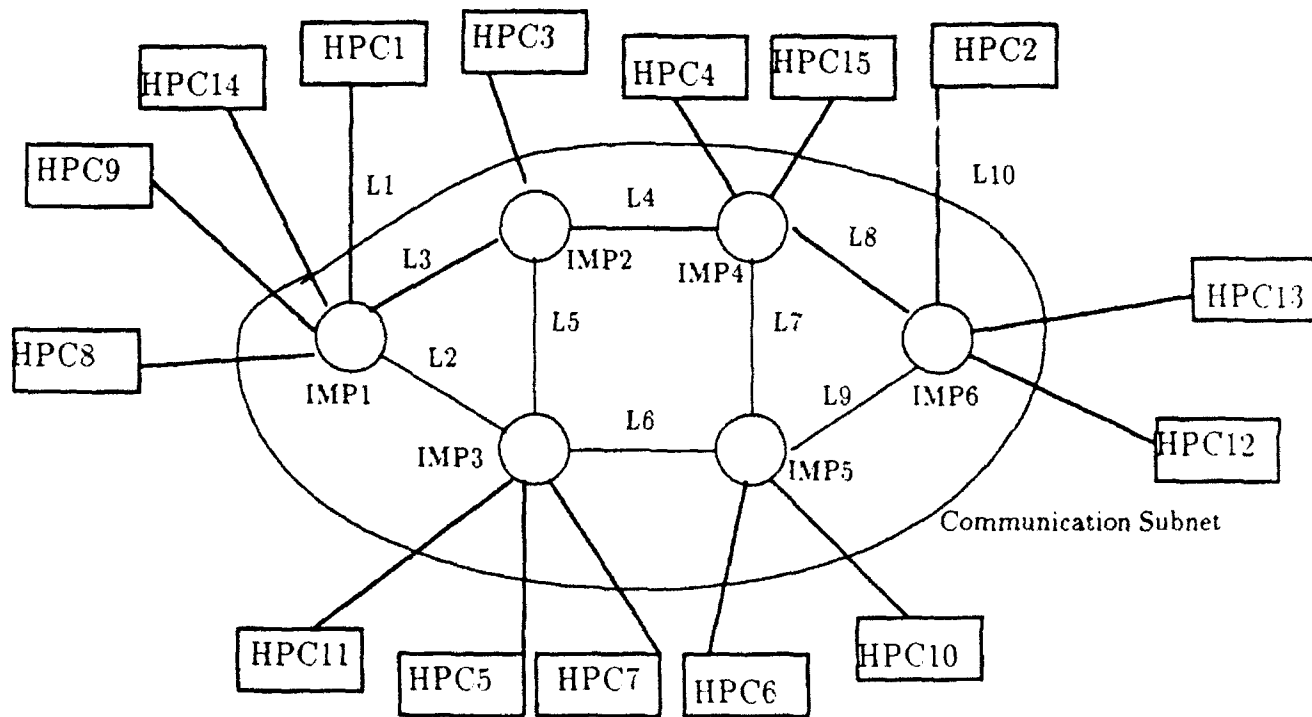
Pkt Arrival Rate (pkts/s.)	Trans. Time (ms.) 32 × 32	Trans. time (ms.) 256 × 256
781	0.1294	0.1306
1562	0.1328	0.1342
2343	0.1384	0.1400
3125	0.1467	0.1487
3906	0.1586	0.1616
4687	0.1764	0.1827

4.5 SUMMARY

In this chapter, we have presented a preliminary design for an Optical Interface Message Processor (OPTIMP) that exploits high-bandwidth, parallelism, multi-dimensional capability, and high storage density offered by optics. The most time consuming operations in communication networks, such as source-destination table search and switching, are implemented fully in optical domain. In addition, since the switching network is all-optical, the system offers a high bandwidth. Our design does not suffer from the optical/electrical conversion bottlenecks and can perform switching and routing in the range of Gigabits/s. This design is for fixed-length packet switching can be adapted for interconnection networks for massively parallel computers. The system protocol and experimental demonstration of the proposed scheme is under way.

REFERENCES

- [1] A.S. Acampora, and M.J. Karol, "An Overview of Lightwave Packet Networks," *IEEE Network*, January 1989, pp.29-41.
- [2] A. Djupsjobacka, "Time Division Multiplexing Using Optical Switches," *IEEE Journal on Selected Areas in Communications*, vol.6, no.7, August 1988, pp.1141-1151.
- [3] R. Ian Macdonald, "Terminology for Photonic Matrix Switches," *IEEE Journal on Selected Areas in Communications*, vol.6, no.7, August 1988, pp.1227-1231.
- [4] Kay Y. Eng, "A Photonic Knockout Switch for High-Speed Packet Networks," *IEEE Journal on Selected Areas in Communications*, vol.6, no.7, August 1988, pp.1107-1116.
- [5] Paul R. Prucnal, and Philipp: A. Perrier, "Self-Routing Photonic Switching with Optically Processed Control," *Optical Engineering*, vol.29, no.3, March 1990, pp.170-182.
- [6] F.B. McCormick et al., "All-Optical Shift Register Using Symmetric Self-Electro-Optical Effect Devices," Topical meeting on photonic switching, paper Thc5, Washington DC, 1989.
- [7] D. Miller, "Optoelectronic Applications of Quantum Wells," *Optics and Electronics News*, February 1990.
- [8] S.D. Smith, "Optical Bistability, Photonic Logic, and Optical Computing," *Appl. Opt.*
- [9] M. Schwartz, "Telecommunication Networks: Protocols, Modeling and Analysis," *Addison-Wesley*, 1987.



HPC : High-Performance Computer (or collection of such)

Figure 4.1 An Example of a Computer Network

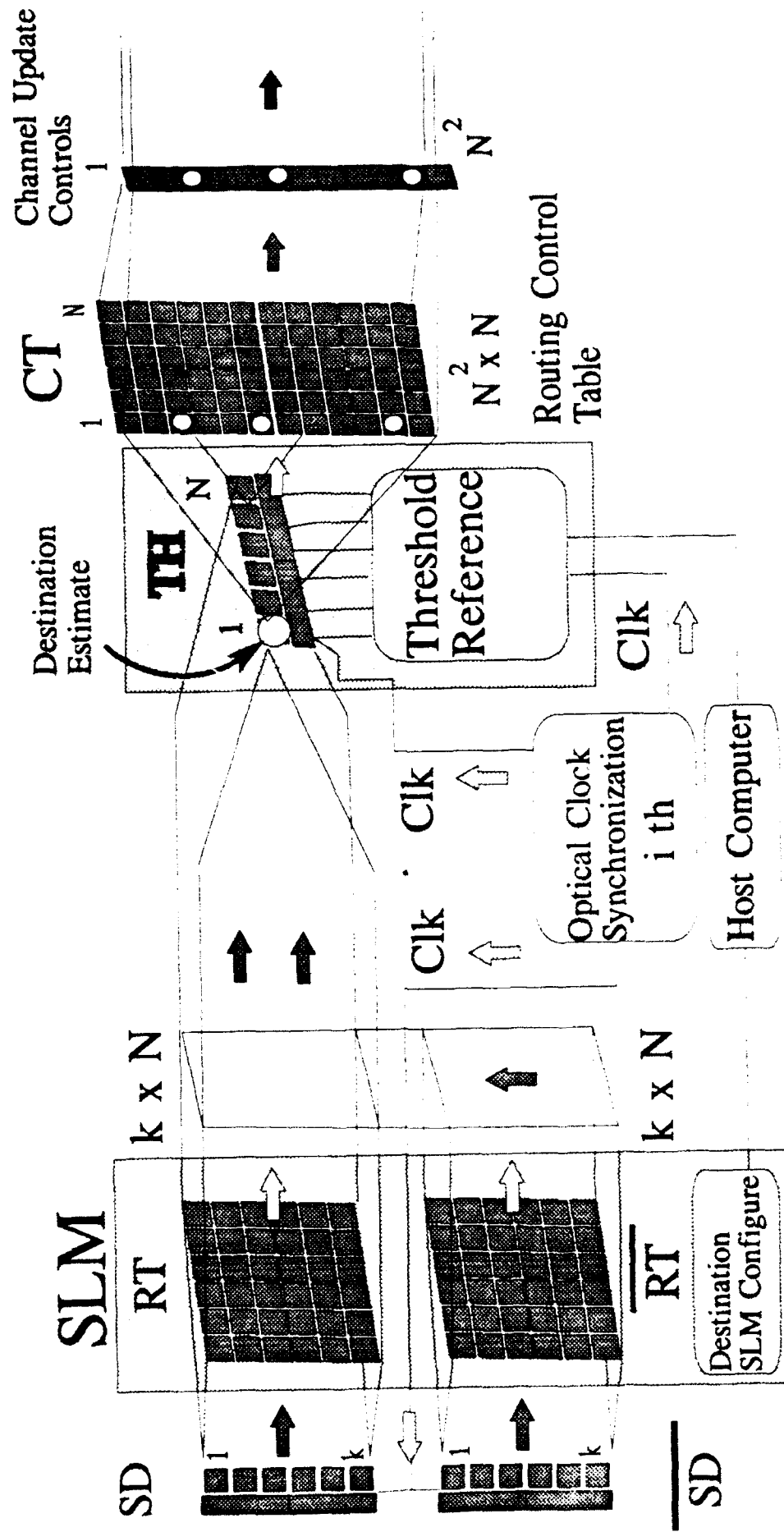


Figure 4.2: OPTIMP with Centralized Routing

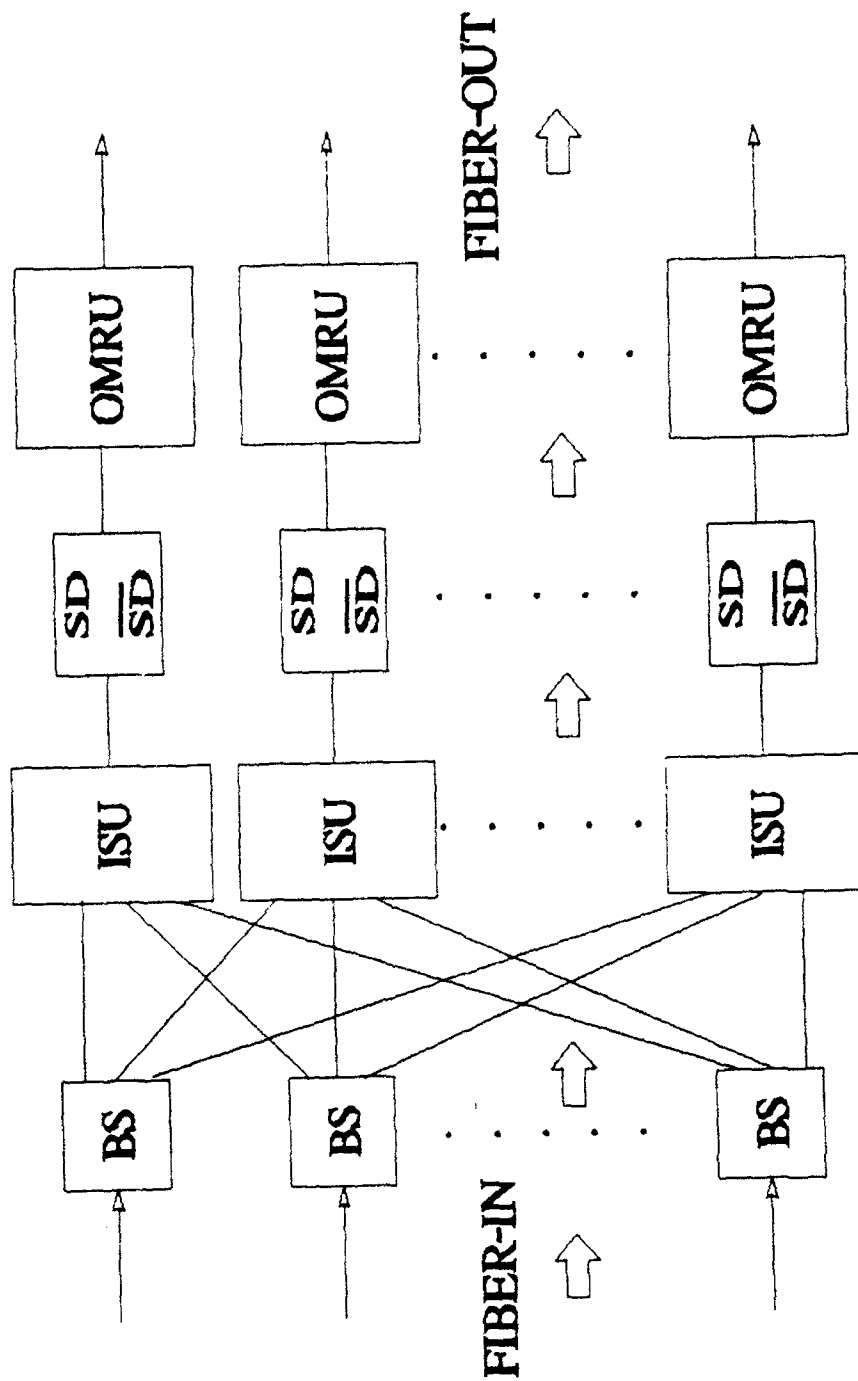


Figure 4.3: OPTIMP with Distributed Routing

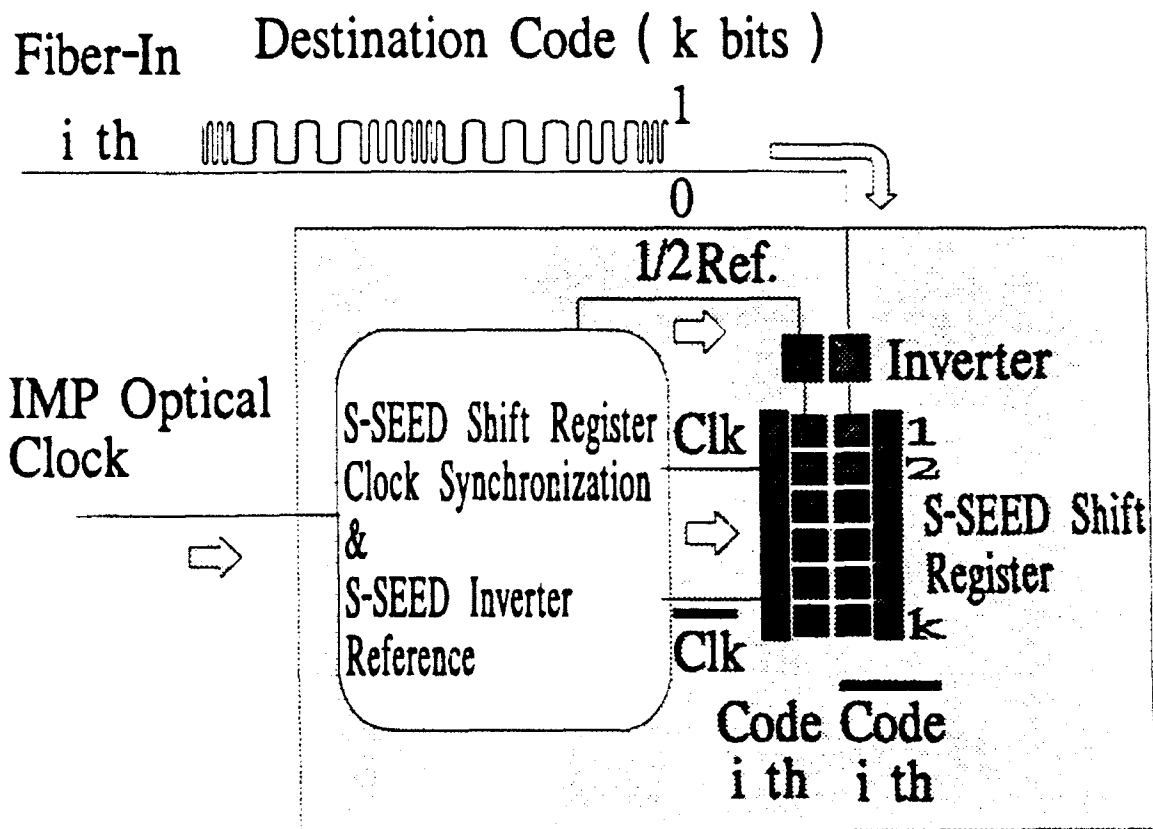


Figure 4.4 Time Domain to Space Somain Conversion

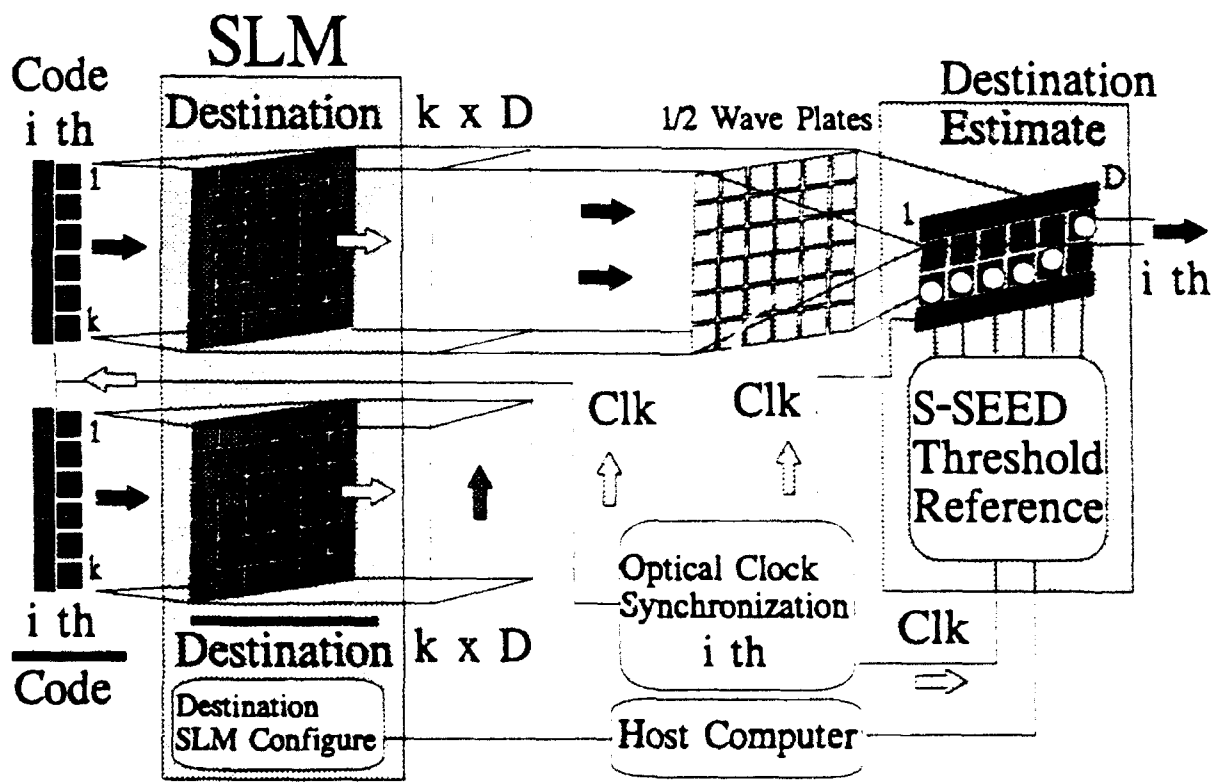


Figure 4.5 Parallel Routing Table Search

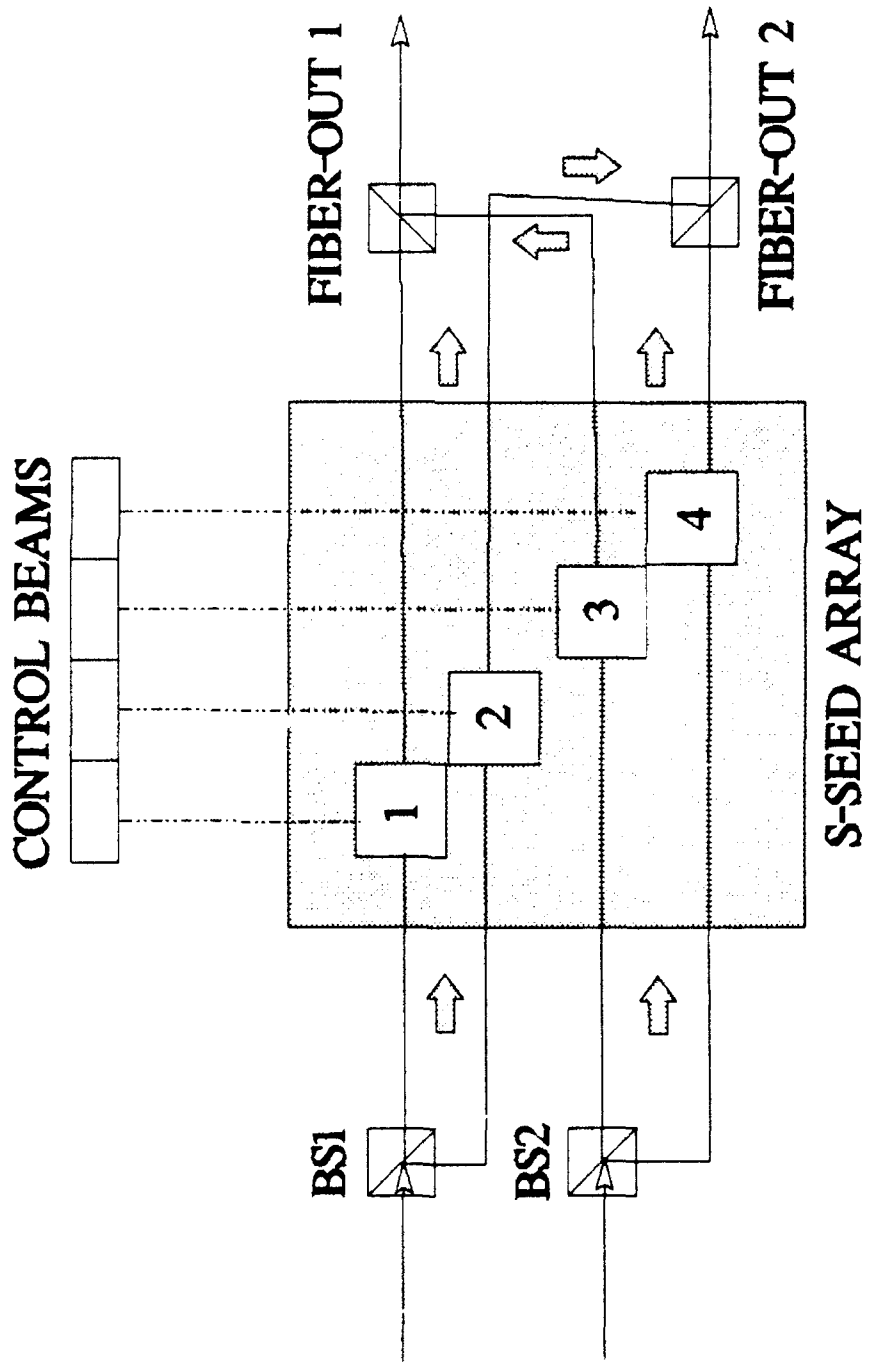


Figure 4.6: Optical Switching Network

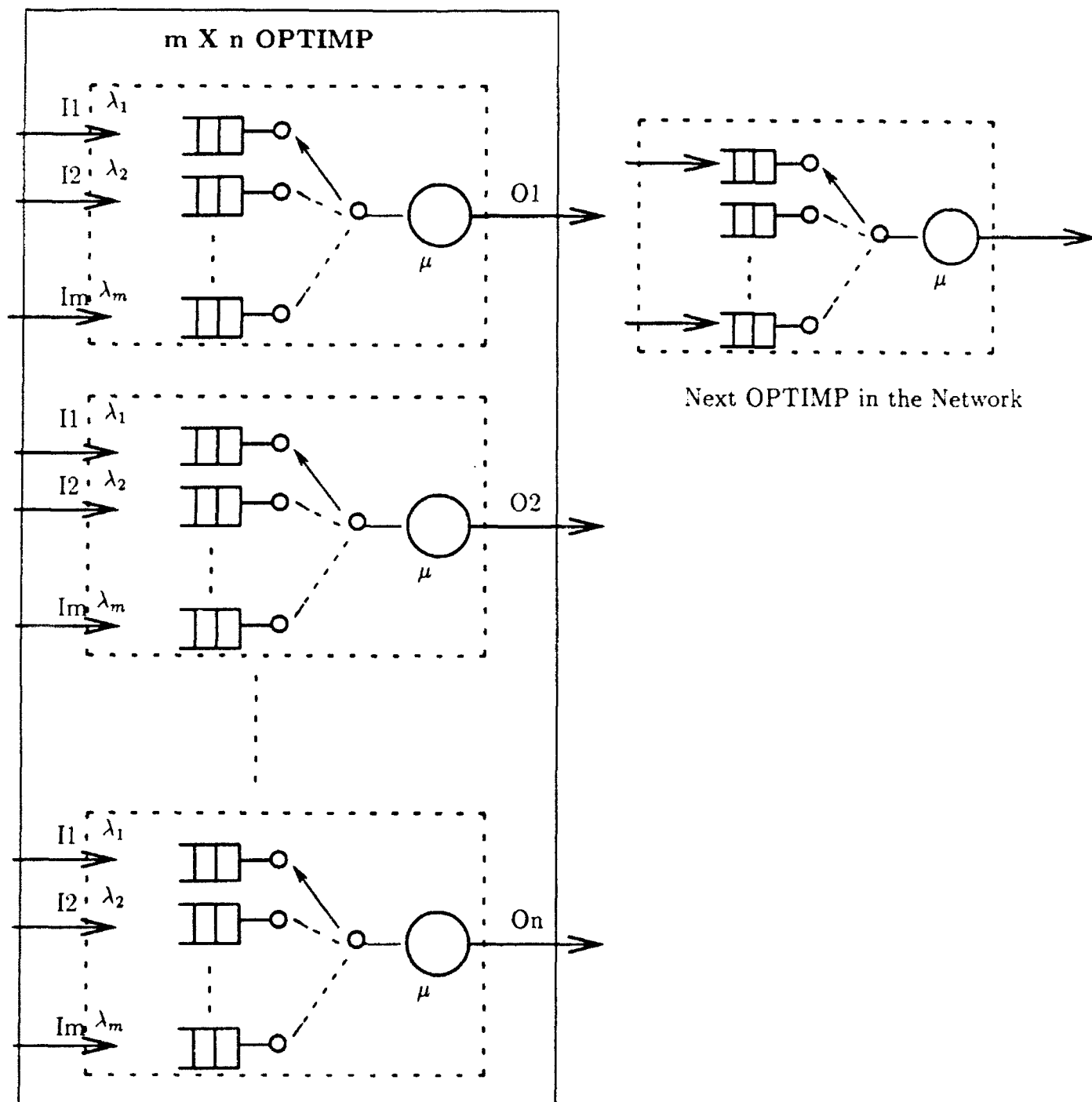


Figure 4.7 A Queueing Model for OPTIMP with Distributed Routing

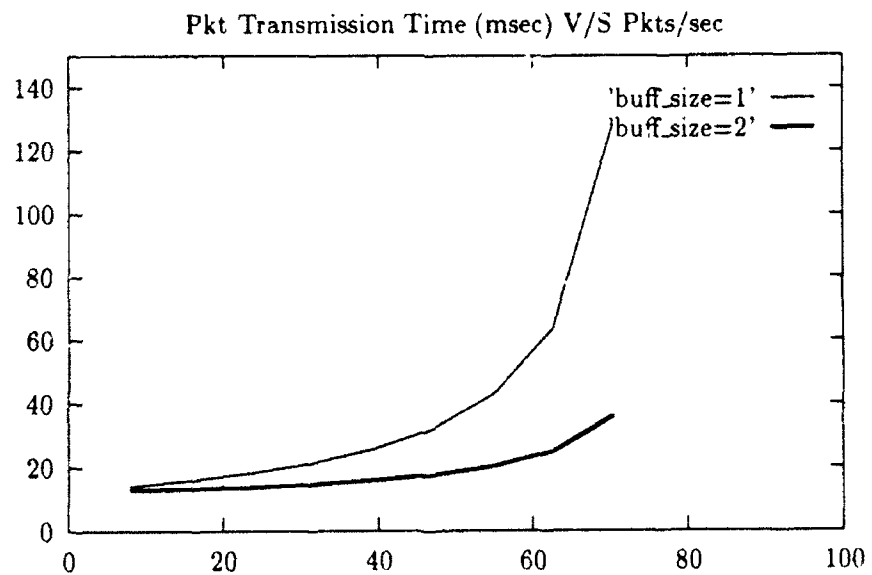


Figure 4.8: Packet Transmission Time vs. Packet Arrival Rate (Medium Speed = 10 Mbps, Packet Length 16 Kbytes)

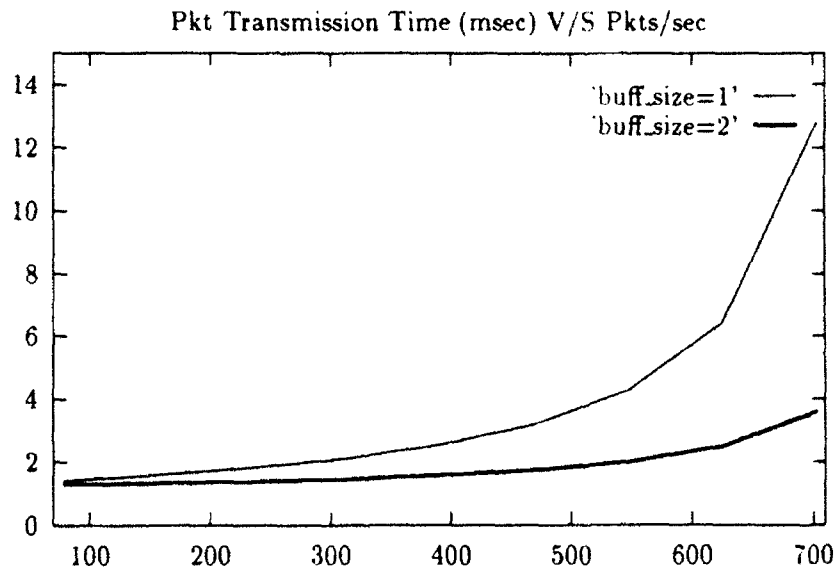


Figure 4.9 Packet Transmission Time vs. Packet Arrival Rate (Medium Speed=100 Mbps, Packet Length 16 Kbytes)

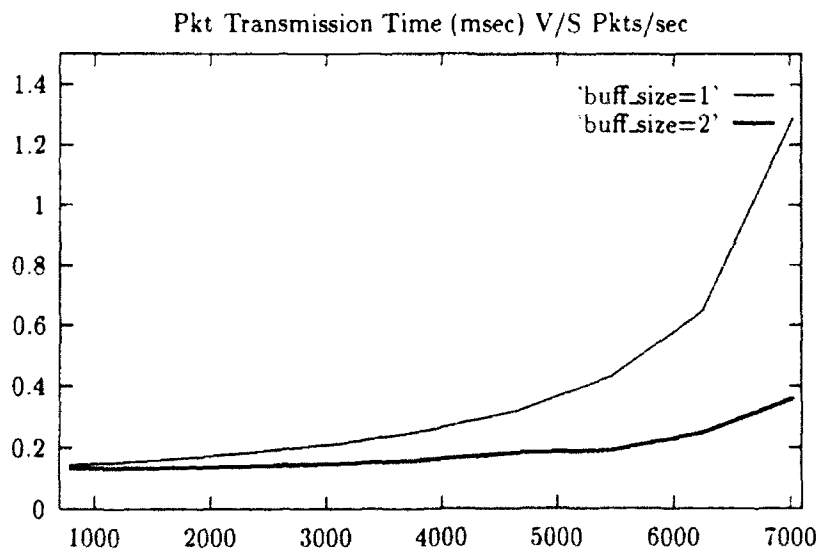


Figure 4.10 Packet Transmission Time vs. Packet Arrival Rate (Medium Speed=1000 Mbps, Packet Length 16 Kbytes)

5. OPTICAL SWITCHING AND TRUTH TABLE LOOK UP USING PHOTOREFRACTIVE CRYSTALS

The design and analysis of the OPTIMP are detailed in the last chapter. The experimental demonstration of the design requires the SEED devices. Unfortunately, to buy the SEED is beyond the budget of this contract. So we concentrated our efforts on an alternative approach based on the photorefractive crystals. This chapter reports some of the results.

There are basically three aspects of photorefractive (PR) crystal that are related to OPTIMP. They are **optical switching for the switching network, optical matrix vector multiplication for the truth table look up, and the noise properties during the operations of the photorefractive crystal based devices.** In this chapter, we first describe how the PR crystal can be used for binary optical switching. The technique can be used in the switching network of the OPTIMP. Then we discuss a pinhole hologram based matrix vector multiplication method that can be used for the truth table look up in the OPTIMP. Finally, we analyze the noise performance during the read out of PR crystal based devices.

5.1 BINARY OPTICAL SWITCHING WITH PHOTOREFRACTIVE POLARIZATION HOLOGRAMS

In this section, we investigate the effect of polarization sensitivity on the intensity and resolution of the diffracted beams from a birefringent photorefractive hologram. In addition, we demonstrate an optical switching technique based on the sensitivity. The method is capable of implementing a large number of 2x2 switching channels with only

four holograms. The on/off ratio of the switches can easily reach 100:1. This switching methodology is applicable to either synchronous or asynchronous interconnection with a variety of photorefractive materials. The combination of the switching can, in theory, form many types of interconnection networks that can be used in OPTIMP.

5.1.1. Background and Motivation

Real-time, dynamic photorefractive crystal holograms have a tremendous potential in their applications to optical computing and signal processing¹⁻³. Some of their advantages are high diffraction efficiency and large information density. One of the unique properties of the photorefractive holograms is that they are usually birefringent. Thus the holograms are usually sensitive to the polarization of the reading beam. The result of this is that the diffracted beam is often degraded in intensity and resolution. The effects in turn limit the performance of the whole optical system, in which the hologram is a component.

We study the polarization sensitivity of photorefractive holograms recorded in a negative uniaxial crystal. Transmission holograms are used in the analysis. However, the method and principle also apply to positive uniaxial crystal and reflective holograms. The analysis shows that certain holographic grating vectors are more sensitive to the polarization change than others. They should be avoided in general imaging applications.

Based on the analysis, we present an optical switching technique that utilizes the polarization sensitivity of birefringent hologram to our advantage. The method, which can implement a large number of 2x2 switches in a single crystal, is based on the polarization sensitivity of the birefringent crystal holograms. The major advantages of polarization

switches are their symmetry with respect to binary logic, theoretical cascadability, and energy conservation^{4,5}. The large bandwidth of free-space optics and the simplicity of the architecture make it viable to a number of applications.

In what follows, we first discuss the diffraction properties of birefringent holograms. Then we analyze the degradation of the output light due to birefringent diffraction. Finally we describe a technique utilizing the polarization sensitivity to implement 2x2 optical switching. Experimental measurements will be presented to prove the proposed switching technique.

5.1.2. Diffraction Properties of Birefringent Holograms

For transmission holograms, two writing beams, R (reference beam) and S (signal beam), enter a negative uniaxial photorefractive crystal as shown in Fig.5.1.1. These two vertically polarized beams (ordinary light), represented by their wave vector K_1 and K_2 respectively, interfere within the photorefractive crystal. A volume hologram represented by the wave vector K_3 is generated.

In the reading process, if we read the hologram with K_1 then the beam represented by the wave vector K_2 is reconstructed. However, if the polarization of the reading beam is changed to the horizontal direction (extraordinary light), the corresponding wave vector inside the crystal will be K_1' . The k_1' beam reads the hologram K_3 . Bragg condition requires that the diffracted wave vector K_2' form a closed triangle with K_1' and K_3 (i.e. momentum conservation). However, the normal surface of the crystal prohibits K_2' . This mismatch ΔK as indicated in Fig. 5.1.1, results in a decrease in diffraction efficiency. Referring to the coupled-wave theory derived by Kogelnik⁶, the dephasing measurement

ϑ for a volume hologram is given as

$$\vartheta = K_3 \cos(\phi - \theta_s) - \frac{K_3^2}{4\pi n_s} \lambda = K_3 \cos(\phi - \theta_s) - \frac{K_3^2}{2K_2'} \quad (1)$$

where ϕ is the angle between grating K_3 and the propagation direction (y axis in Fig.5.1.1), θ_s is the angle between the signal beam and the propagation axis, K_2' is the diffracted wave vector in Fig.5.1.1. Note that when the Bragg condition is satisfied, ϑ equals zero. when the Bragg condition is not met, we can expand ϑ in a Taylor expansion to the first order. Therefore, ϑ in the above case can be approximated as

$$\vartheta = \frac{K_3^2}{2k_2'^2} \Delta K \quad (2)$$

Let's further assume that the multiple diffraction process can be neglected for a multi-exposure hologram. Under weak coupling approximation, the normalized diffraction efficiency for transmission holograms can be expressed as⁶

$$\eta = v^2 \text{sinc}^2 \zeta \quad (3)$$

where $v = \pi n_1 d / \lambda (\cos \theta_s \cos \theta_r)^{1/2}$, $\zeta = K_3^2 d \Delta K / 4K_2'^2 \cos \theta_s$, n_1 is the amplitude of the spatial modulation of the refraction index, λ is the wavelength, θ_r and θ_s are the angles between propagation direction and reference and signal beams respectively, d is the thickness of crystal. The ΔK for a transmission hologram can be calculated as following.

Referring to Fig.5.1.1, we can calculate the z and y component (K_z , K_y) for grating K_3 by

$$(K_x, K_y) = \frac{2\pi}{\lambda} (\sin\alpha_s + \sin\alpha_R, \sqrt{n_0^2 - \sin^2\alpha_s} - \sqrt{n_0^2 - \sin^2\alpha_R}), \quad (4)$$

where λ is the free-space wavelength of the light beam. Let the z and y component of the desired vector K_2' be (P_z, P_y) , using vector algebra we find (P_z, P_y) as

$$(P_x, P_y) = K_1' + K_3 = \frac{2\pi}{\lambda} [\sin\alpha_s, \sqrt{n_0^2 - \sin^2\alpha_s} + (\frac{n_e}{n_o} - 1)\sqrt{n_0^2 - \sin^2\alpha_R}], \quad (5.a)$$

where $n_e(\theta_R)$ is the index of refraction along K_1' (referring to Fig.5.1.1). The OP line is

$$P_y Z - P_x Y = 0 \quad (5.b)$$

However, the normal surface of the refractive index ellipse allows only the wave vector OB. The index ellipse in this $x=0$ plane is given as^[7]

$$\frac{Z^2}{n_o^2} + \frac{Y^2}{n_e^2} = 1. \quad (6)$$

Solving the equations (5.b) and (6), we can find out the values of |OB| and |OP|. The mismatch ΔK is expressed as

$$|\Delta K| = |OB| - |OP| = \sqrt{P_x^2 + P_y^2} \left[\sqrt{\frac{n_e^2 n_o^2}{n_e^2 P_x^2 + n_o^2 P_y^2}} - 1 \right]. \quad (7)$$

As we have shown above, when the reading beam is not ideally polarized in the direction of the recording beam, the orthogonal polarization component will encounter a wave vector mismatch ΔK . As a result, the overall diffraction efficiency will decrease. In addition, the diffracted beam in the orthogonal polarization will propagate in a slightly

different direction. The combination of the two components will smear the diffracted pattern. In what follows, we study the degradation of the diffracted beam (pattern) due to the two effects. Then we will discuss the applications of the effects to optical beam directional coupling.

5.1.3. Output Degradation Due to Birefringent Diffraction

Suppose a perfect volume hologram is recorded in a negative uniaxial photorefractive crystal LiNbO_3 using vertical polarization (ordinary light), as described in last section. Assume that in readout process the reading beam is not in perfectly vertical polarization due to misalignment or system disturbance. But it is still a linearly polarized light with an inclination angle β to the vertical polarization. We can thus decompose the reading light into vertical (ordinary light) and parallel (extraordinary light) polarization. The total output intensity from this unity reading beam is

$$I_{out} = \eta_{\parallel} \sin^2 \beta + \eta_{\perp} \cos^2 \beta, \quad (8)$$

where η_{\parallel} and η_{\perp} are the diffracted efficiency of parallel and vertical polarization, respectively. Since the two orthogonal components of the diffracted beam will travel in slightly different directions, the output pattern will be smeared. In addition, one of the components does not meet the Bragg condition, the mismatch ΔK will result in a decrease in diffraction efficiency. We now discuss these effects separately.

In the first case, let's assume the hologram is used only to direct the reading beam to an optical receiver and the detector of the receiver is large enough so that both of the two orthogonal output components are incident on the detector. Therefore, the only effect of the non-ideal polarization is to decrease the output intensity. The relative decrease can

be calculated by

$$S = \frac{\Delta I}{I} = \left(1 - \frac{\eta_{\parallel}}{\eta_{\perp}}\right) \sin^2 \beta. \quad (9)$$

Since the optical system is designed for perfect readout, it is reasonable to assume the polarization inclination angle β to be small. If β is taken to be $\pm 10^\circ$, it can be shown that for all possible holographic grating vectors, the maximum S is 0.029 when $\eta_{\parallel}=0$; similarly, the minimum value is zero when $\eta_{\parallel}=\eta_{\perp}$. In other words, the total output intensity does not change significantly if the detector window is large enough.

Now let's analyze the effect that in general the two orthogonal components of the diffracted light travel in different directions. This effect results in a blurring on the output plane. If the hologram is used for imaging, the blurring degrades the resolution of the system. If the hologram is used for optical interconnection, the blurring will limit the number of signal channels or interconnection density of the system. To define a meaningful measure of the blurring, we observe that there is no blurring if the two orthogonally polarized diffracted beams travel in the same direction or one of them has a very weak intensity. So the index of the blurring can be defined as

$$B = \frac{I_{\min}}{I_{\max}} \gamma, \quad (10)$$

where I_{\min} is the weak intensity component of the two orthogonal diffracted components, and the I_{\max} is the stronger one, γ is the separation angle between them. It can be shown that the output intensities depend on the magnitude and the angle of the grating vector written inside the photorefractive materials as well as the polarization inclination angle

β introduced by the imperfectly polarized reading beam. The separation angle γ is a function of the incident angle α_S, α_R . The relation between γ and α_S, α_R can be given as

$$\gamma = |\alpha_S - \sin^{-1} \left[\frac{n_e n_o}{\sqrt{n_e^2 + n_o^2 \left(\frac{\sqrt{n_o^2 - \sin^2 \alpha_S} + \left(\frac{n_e}{n_o} - 1\right) \sqrt{n_o^2 - \sin^2 \alpha_R}}{\sin \alpha_S} \right)^2}} \right]|. \quad (11)$$

Referring to Fig.5.1.1, α_S and α_R can be written as a function of the magnitude of grating vector K_3 and the angle of the grating vector δ as below,

$$\alpha_S = \sin^{-1} \left[\frac{k_3 \lambda}{4\pi} \cos \delta + \sin \delta \sqrt{n_o^2 - \left(\frac{k_3 \lambda}{4\pi}\right)^2} \right], \quad (12)$$

$$\alpha_R = \sin^{-1} \left[\frac{k_3 \lambda}{4\pi} \cos \delta - \sin \delta \sqrt{n_o^2 - \left(\frac{k_3 \lambda}{4\pi}\right)^2} \right]. \quad (13)$$

By substituting Eq.12,13 into Eq.11, we can express γ as a function of the grating vector K_3 . Because K_3 gives more physical insight than α_S, α_R and K_3 affects both γ and I_{\min}/I_{\max} , so it is used as a parameter, instead of γ , in the discussion of B. These dependence imply that the index of blurring is a function of the grating inside the photorefractive material and the polarization inclination angle of the reading beam.

The following discussion is devoted to the effects of the polarization inclination angle and the grating vector on the index of blurring. Computer simulation is used to calculate their relationship and the results are shown in Fig.5.1.2 through Fig.5.1.6. For simplicity, the normalized grating vector, *i.e.* the grating vector divided by $2\pi/\lambda$, where

λ is the wavelength of the optical beam, is used in the plots. In following discussion, \mathbf{B} , K_3 , δ , β , γ , η_V/η_\perp , and ΔK represent the index of blurring, the magnitude of the normalized grating vector, the angle of the normalized grating vector (referring to Fig.5.1.1), the polarization inclination angle, the separation angle, the diffraction efficiency ratio, and the magnitude of wave vector mismatch (referring to Fig.5.1.1), respectively. As mentioned before, β can easily be adjusted to be within 10° and its influence on \mathbf{B} is small. However, in some cases such as application of double grating in neural network^[8] or direction coupling switch to be discussed later, the consideration of large β must be included. The purpose of the following discussion is to provide a general description of \mathbf{B} . Since \mathbf{B} is very small when β is between 0° and 40° , the plots only show the most significant range of β which is between 40° and 90° . Figure 5.1.2 depicts γ as a function of K_3 for a fixed δ . Generally speaking, for fixed δ , γ is a monotonously increasing function of K_3 . For a fixed K_3 , the larger the δ , the larger the γ . In the range $0 < K_3 < 1.0$, computer simulation shows that the max $\gamma=3.6^\circ$ when $K_3=0.988$ and $\delta=13.35^\circ$, which corresponds to $\alpha_s=-85^\circ$, $\alpha_r=2^\circ$ (α_s and α_r are in the same side of Y axis in Fig.5.1.1). The larger γ should be avoided in general imaging applications.

Figure 5.1.3 shows \mathbf{B} as a function of K_3 for a fixed β with δ as a parameter. According to Eq.10, \mathbf{B} is the product of η_V/η_\perp and γ . Referring to Eq.3 and Eq.14, η_V/η_\perp is a sinc function of ζ which is proportional to K_3 square and other parameters, and η_V/η_\perp is a monotonously decreasing function of K_3 in $0 < K_3 < 0.5$. On the other hand, for fixed δ , γ is a monotonously increasing function of K_3 . Therefore, \mathbf{B} is the product of a

monotonously decreasing function $\eta_{\perp}/\eta_{\parallel}$ and a monotonously increasing function γ . The product gives a peak of **B**. From this plot we see that for equal K_3 , a large δ will result in a large **B**. That is because a large δ produces a large γ , which in term gives a large **B**.

Figure 5.1.4 depicts **B** as a function of K_3 for fixed δ with β as a parameter. In these curves, the horizontal polarization component of the reading beam is smaller than vertical polarization component, *i.e.* $I_{\max}=\eta_{\perp}\cos^2\beta$ and $I_{\min}=\eta_{\parallel}\sin^2\beta$. According to Eq.10, **B** is the product of I_{\min}/I_{\max} and γ . At fixed values of K_3 and δ , γ is a constant. So the difference of **B** is determined by $\tan^2\beta$ only. The reasons that cause the peak of curves in Fig.5.1.4 are the same as in Fig.5.1.3.

Figure 5.1.5 shows **B** versus β for fixed δ with K_3 as a parameter. At small β , $I_{\max}=\eta_{\perp}\cos^2\beta$ and $I_{\min}=\eta_{\parallel}\sin^2\beta$, so that I_{\min}/I_{\max} is a monotonously increasing function of β . As β approaches 90° , $\eta_{\perp}\cos^2\beta$ is smaller than $\eta_{\parallel}\sin^2\beta$, and I_{\min}/I_{\max} becomes a monotonous decreasing function of β . Therefore, in $0^\circ<\beta<90^\circ$, **B** has a peak value which equals γ , when $\eta_{\perp}\cos^2\beta$ equals $\eta_{\parallel}\sin^2\beta$. Usually for fixed δ , a large K_3 results in a large γ which equals the peak value of **B**. That explains why a large K_3 in Fig.5.1.5 has a large peak value of **B**.

Figure 5.1.6 shows **B** versus β for a fixed K_3 with δ as a parameter. The reasons for having a peak point in curves of Fig.5.1.6 are the same as in Fig.5.1.5. For fixed K_3 , a large δ usually results in a large γ and **B** equals γ at peak point. That is why a curve in Fig.5.1.6 with a large δ has a large peak value **B**.

As we have shown above, the birefringent of the photorefractive crystal usually degrades the diffracted light in intensity and resolution when the reading beam is not

perfectly polarized. For certain amplitude and angle of a grating vector in a given crystal, the influence of the imperfect polarization of reading light is more obvious. For example in LiNbO_3 at $K_3=0.269$, $\delta=13.3^\circ$, when β changes from 0° to 44° the index of blurring B switches from 0 to 0.0366° . Thus, they should be avoided for imaging applications. However, the polarization sensitivity can be utilized in implementing polarization optical switches, as will be shown in the next section.

5.1.4. Two by Two Optical Directional Coupling Switch

The polarization sensitivity is ideal to implement binary logic. The principle of a 2×2 optical polarization switch using holograms is illustrated in Fig.5.1.7. The grating vector **AP** and **BQ** are written in the photorefractive crystal with vertical and horizontal polarizations, respectively. When the grating **AP** is read out with R_1 using vertical polarization, the diffracted beam is denoted by its wave vector **C**. This vertically polarized reading beam contributes almost no light in the **D** direction, because the mismatch ΔK is so designed that the diffraction efficiency in the **D** direction is virtually zero. Similarly, if the grating **BQ** is read out with the same reference beam R_1 but in the horizontal polarization, the wave vector inside the crystal is **OB** and the corresponding diffracted wave vector is changed to **D**. Thus, by changing the polarization of the reading beam, we can read different gratings inside the crystal. Since different gratings result in diffracted beams in different directions, an optical directional coupling switch can be realized in this simple fashion. Notice that in the above process, the polarization of the reading beam is changed while the direction of the reading beam before entering the crystal is unchanged. Currently, there exist a number of spatial light modulators available to achieve this end,

such as electrically addressed magneto-optical devices, liquid-crystal televisions, and optical addressed liquid-crystal light valves and microchannel spatial light modulators. We have expanded the above concept to record four such gratings in the crystal. They are designed in such a way that by changing the polarization of reading beam R_1 , the diffracted beam goes in either C or D direction. Similarly, by changing the polarization reading beam R_2 , the diffracted beam also goes to either C or D direction. Therefore, by changing the polarization of a single beam, we can switch (or direct) it to either one of the two predetermined directions, as shown in Fig.5.1.6. In other words, the crystal holograms function as 2x2 switch, or a 4-port device, that can connect any one of the two inputs to any one of the two outputs.

The total number of switch channels that can be handled by the crystal hologram is basically limited by the number of resolvable spots of the diffracted beams. According to the Rayleigh criterion^[9], the minimum angle, α_{\min} , between two resolvable beams is $1.22\lambda/d$, where λ is the wavelength, and d is the diameter of the diffracted beam. Consider two parallel circular optical beams that are incident on a crystal surface. Assume that the output beams emerging from the other side of the crystal are also parallel. If an observation plane is placed in a direction z from the back plane of the crystal then the minimum separation between these two circular beams is given by $\delta_{\min}=1.22\lambda z/d$. The number of optical channels is determined by the diameter of the optical beam, the size of the crystal, the distance between the crystal, the observation plane, and the wavelength. For example, if we require the observation plane to be 5 mm away from the crystal, the resolution on the plane to be $\delta_{\min}=0.03$ mm, and use a He-Ne ($\lambda=633$ nm) the diameter

of the signal beams would be $d=0.128$ mm. Therefore, for a crystal of area 1.5 cm x 1.5 cm about 10^4 signal channels can be achieved. Further, the number of channels could be dramatically increase by using a larger crystal.

Because of the storage capacity and resolution of a crystal hologram, a great number of switches can be built on a small crystal. These switches can be addressed either synchronously by a thick beam of light, or asynchronously through spatial light modulators. The former method has the advantage of massive parallelism while the latter is more flexible.

5.1.5. Experimental Measurement for Optical Switching

To illustrate the feasibility of the above discussed polarization switching concept, we measured the switching behavior of the crystal hologram using the experimental setup as shown in Fig.5.1.8. The laser beam is divided into two parts by a polarizing beam splitter. Two half-wave plates were placed at the two outputs of the beam splitter to rotate the polarization of the optical beams. In the recording process, the polarization of both reference and signal beams are the same. In the reading process, we first blocked out the signal beam; then, we measured the diffracted light from the reference beam in vertical and horizontal polarizations, respectively. A piece of LiNbO_3 crystal (1 cm³) was used as the recording medium. To simplify the experiment, two parameters were used to describe the incident beams instead of α_s and α_r in Fig.5.1.1. One is the write-in angle which is the angle between the reference beam R and the signal beam S (2α in Fig.5.1.8). The other is the ρ angle which is the angle between the crystal surface and the line that bisects R and S (ρ in Fig.5.1.8).

The write-in angle was confined at between 18.4° and 23.2°. This angle limitation is due to the diameter of the laser beam (0.5 cm) and the size of the crystal (1 cm³). For each of the write-in angle given above, seven measurements were conducted by rotating the crystal at 2° steps. The wavelength was 633 nm (He-Ne Laser). The intensity of diffracted beam was measured by a power detector.

Figure 5.1.9 shows the theoretical and experimental diffraction efficiency ratio of vertical polarization over horizontal polarization .vs. angle ρ . Equation 3 is modified by the transmittance behavior at the two boundary planes to provide the theoretical prediction as given by

$$\frac{\eta_{\parallel}}{\eta_{\perp}} = \frac{T_{air \rightarrow n_c} \times T_{n_c \rightarrow air} \times v_{\parallel}^2 \text{ sinc}^2 \zeta}{T_{air \rightarrow n_c} \times T_{n_c \rightarrow air} \times v_{\perp}^2}, \quad (14)$$

where $T_{air \rightarrow n_c}$ is the transmittance for a vertical polarized reference beam from air to crystal and $T_{n_c \rightarrow air}$ is the from crystal to air. $T_{air \rightarrow n_c}$ is the transmittance for a horizontal polarized reference beam from air to crystal and $T_{n_c \rightarrow air}$ is the from crystal to air. Referring to Fig.5.1.1, these values can be obtained as follows:

$$T_{air \rightarrow n_c} = \frac{\sin 2\alpha_R \times \sin 2\theta_R}{\sin^2(\alpha_R + \theta_R)}$$

$$T_{n_c \rightarrow air} = \frac{\sin 2\alpha_S \times \sin 2\theta_S}{\sin^2(\alpha_S + \theta_S)}$$

The optimum performance for switching is achieved by finding the minimum of the above equations. For clarity and due to the window size of the crystal only two sets of data are

$$T_{air \rightarrow R} = \frac{\sin 2\alpha_R \times \sin 2\theta_R}{\sin^2(\alpha_R + \theta_R) \times \cos^2(\alpha_R - \theta_R)}$$

$$T_{R \rightarrow air} = \frac{\sin 2\alpha_S \times \sin 2\theta_S}{\sin^2(\alpha_S + \theta_S) \times \cos^2(\alpha_S - \theta_S)}$$

presented in Fig.5.1.9, $2\alpha=18.4^\circ$ and $2\alpha=23.2^\circ$. The two curves in Fig.5.1.9 follow essentially the sinc function. As can be seen from Eq.14, the diffraction efficiency ratio is about one when ρ is 90° and it decreases rapidly to zero when ρ approaches 105° . The theory and experimental data have very good match for $2\alpha=23.2^\circ$, but not for $2\alpha=18.4^\circ$. The reason is under investigation. Our preliminary analysis is that besides the measurement error, the discrepancy may also be due to assumptions made in the associated coupling wave theory. The assumption is that there is small absorption loss and a slow energy interchange between the coupled waves (R and S) and the theory does not consider the second order term in the wave equations (R" and S"). Furthermore the laser beam is Gaussian; whereas, the coupled wave theory assumes plane waves. The absolute diffraction efficiency is about 30%. This can be improved by putting antireflection coatings on both sides of the crystal and using better quality laser beams.

The interesting role of ΔK is worth discussion. As expressed by Eq.3, the switching behavior is roughly a sinc function of ζ which is proportional to ΔK . Within the main lobe of the sinc function, larger ΔK results in a smaller diffraction efficiency ratio. In this polarization optical switch, a small efficiency ratio results in a large signal to noise ratio, that is a large distinction between signal "on" and noise "off". In practice, the choice is limited by the configuration of the optical system and the size of the crystal.

As demonstrated in our experiment for a 1 cm^3 LiNbO₃ crystal, an efficiency ratio of less than 0.01 (i.e, the "on" and "off" ratio larger than 100) can be easily achieved. This is adequate for many binary operations.

5.1.6. Conclusion on Photorefractive Binary Switching

The polarization sensitivity of birefringent photorefractive volume hologram has been investigated. Generally speaking, the birefringent will degrade the diffracted beam in both diffraction efficiency and resolution. For a given crystal, a grating vector is sensitive to polarization change if its diffraction efficiency ratio almost equals zero. This should usually be avoided for imaging applications. The technique of using polarization sensitive holograms to implement a large number of 2x2 optical switches on a single crystal has also been described. The method has several positive attributes. First, polarization optical switching provides theoretical cascability and energy conservation. Second, the free space optics offers a very large bandwidth. Finally, the design requires only four holograms which can yield high photorefractive efficiency. The development of better and larger photorefractive crystal may further improve the technique. The volume holographic method has the advantage of high resolution when compared with other polarizing (spatial light modulator) technique.

REFERENCES FOR 5.1

1. P. Gunter and J.P. Huignard, Photorefractive Materials and Their Applications 1,2, (Springer-Verlag, New York, 1989), vol.61,62.
2. S. Martellucci and A.N. Chester, Nonlinear Optics and Optical Computing, (Plenum Press, New York, 1990).
3. Dror G. Feitelson, Optical Computing, (MIT Press 1988).
4. Shudong Wu, Q.Wang Song, Andy Mayers, Don A. Gregory and Francis T.S. Yu, "Reconfigurable Interconnections Using Photorefractive Holograms," *Appl. Opt.*, vol.29, pp.1118, 1990.
5. Q.W. Song, M.C. Lee, P.J. Talbot, and E. Tam, "Optical Switching with Photorefractive Polarization Holograms," *Opt. Lett.*, vol.16, no.16, pp.1228-1230, 1990.
6. Herwig Kogelnik, "Coupled Wave Theory for Thick Hologram Gratings." *The Bell System Technical Journal*, pp.2909-2947, 1969.
7. Pochi Yeh and Amnon Yariv, Optical Waves in Crystals, (Wiely, New York, 1984).
8. Hsin-Yu and Demetri Psaltis, "Double Grating Formation in Anisotropic Photorefractive Crystals," *J. Appl. Phys.*71 (3), pp.1394-1400, 1992.
9. P.P. Banerjee and T.C. Poon, Principles of Applied Optics, (Richard Irwin, New York,1991).

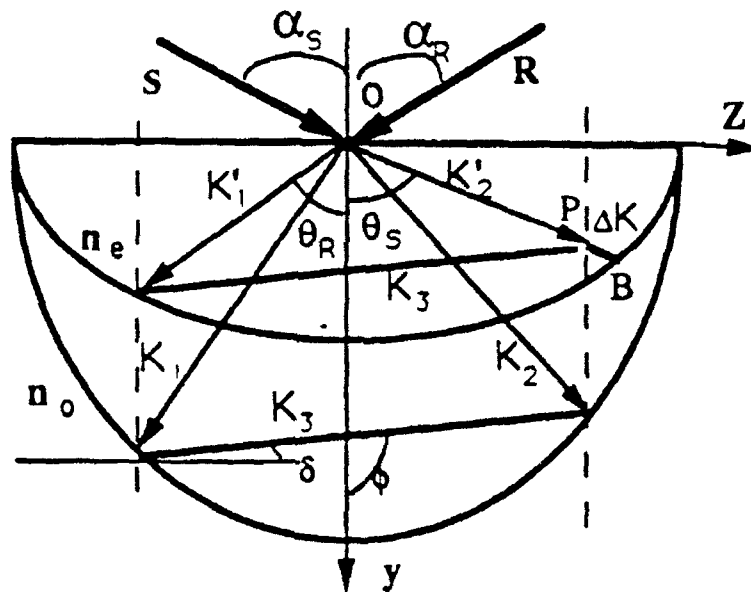


Figure 5.1.1 Wave Vector Diagram of a Transmission Volume Hologram.

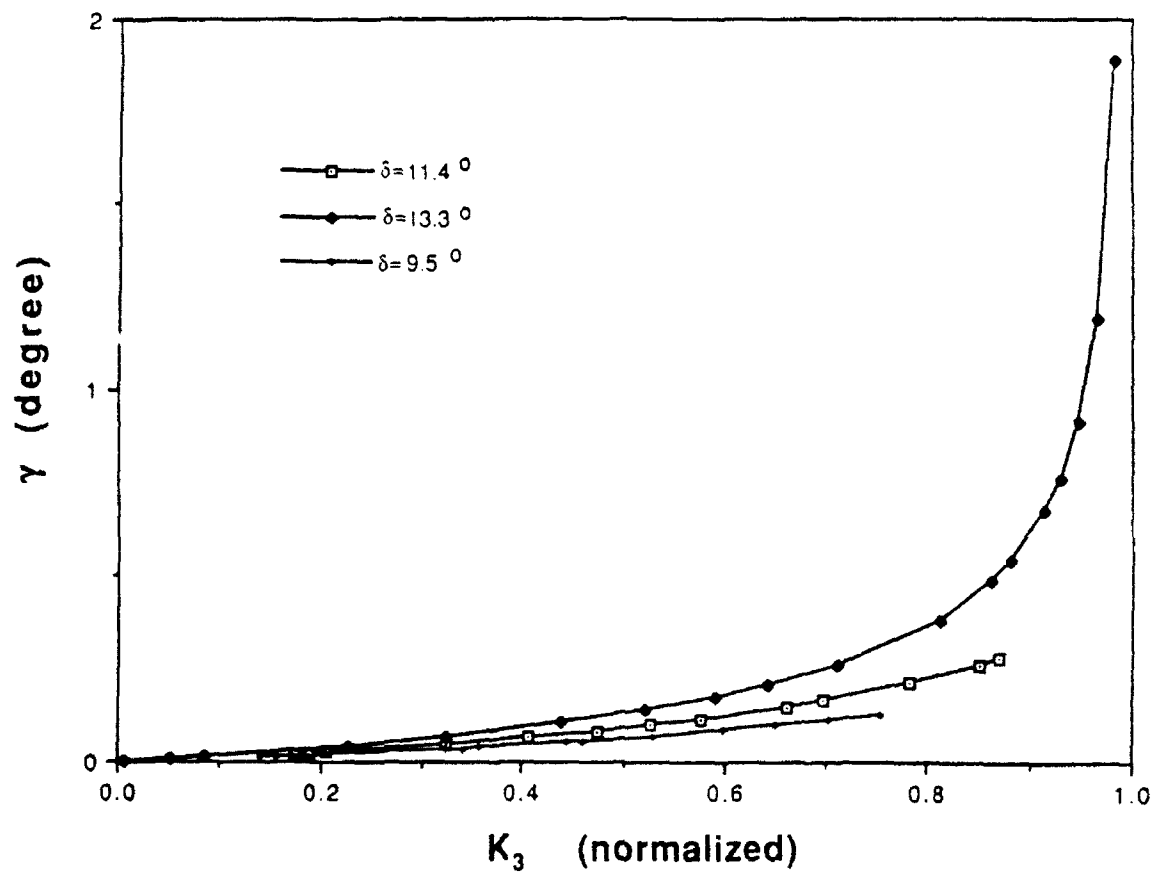


Figure 5.1.2 Separation Angle Versus the Magnitude of Grating Vector for a Fixed Grating Angle.

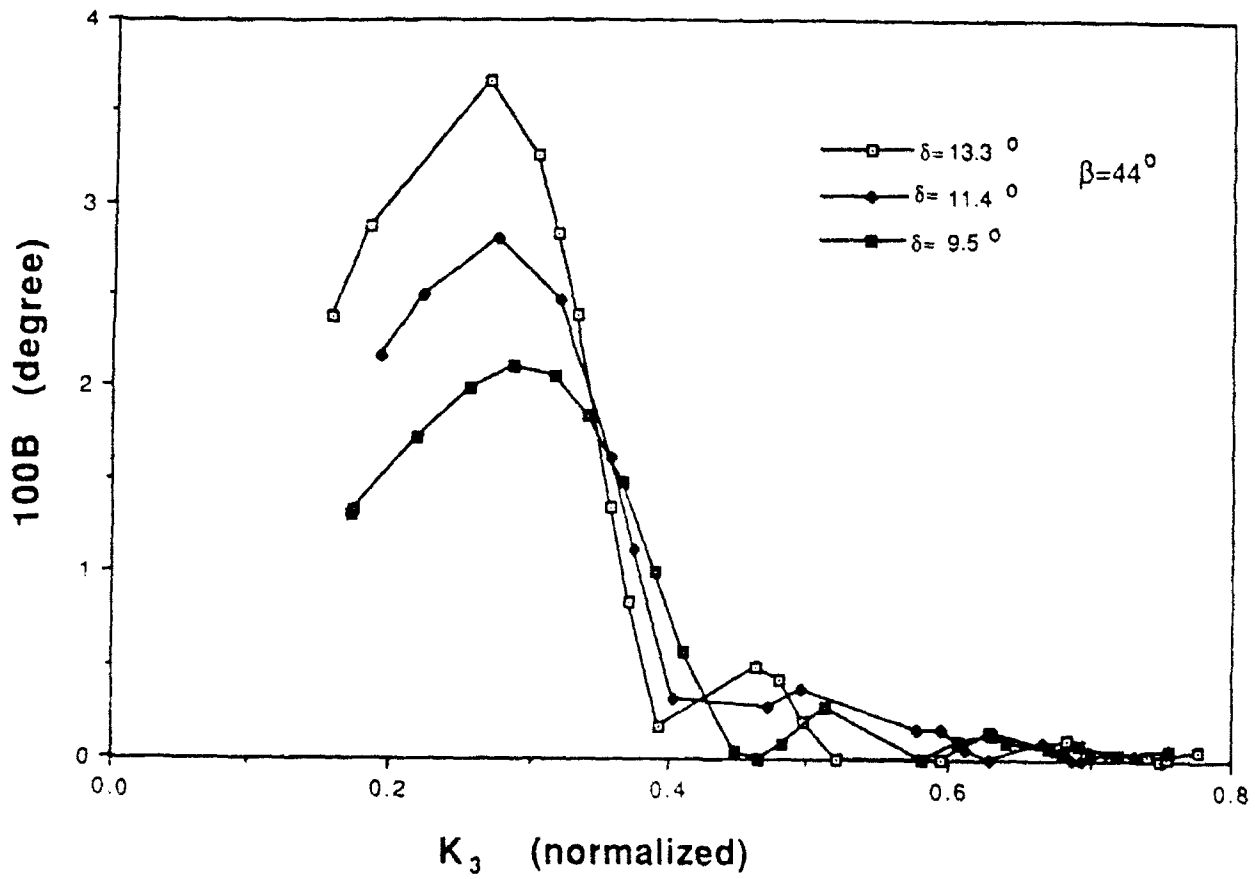


Figure 5.1.3 Index of Blurring Versus the Magnitude of Grating for a Fixed Polarization Inclination Angle.

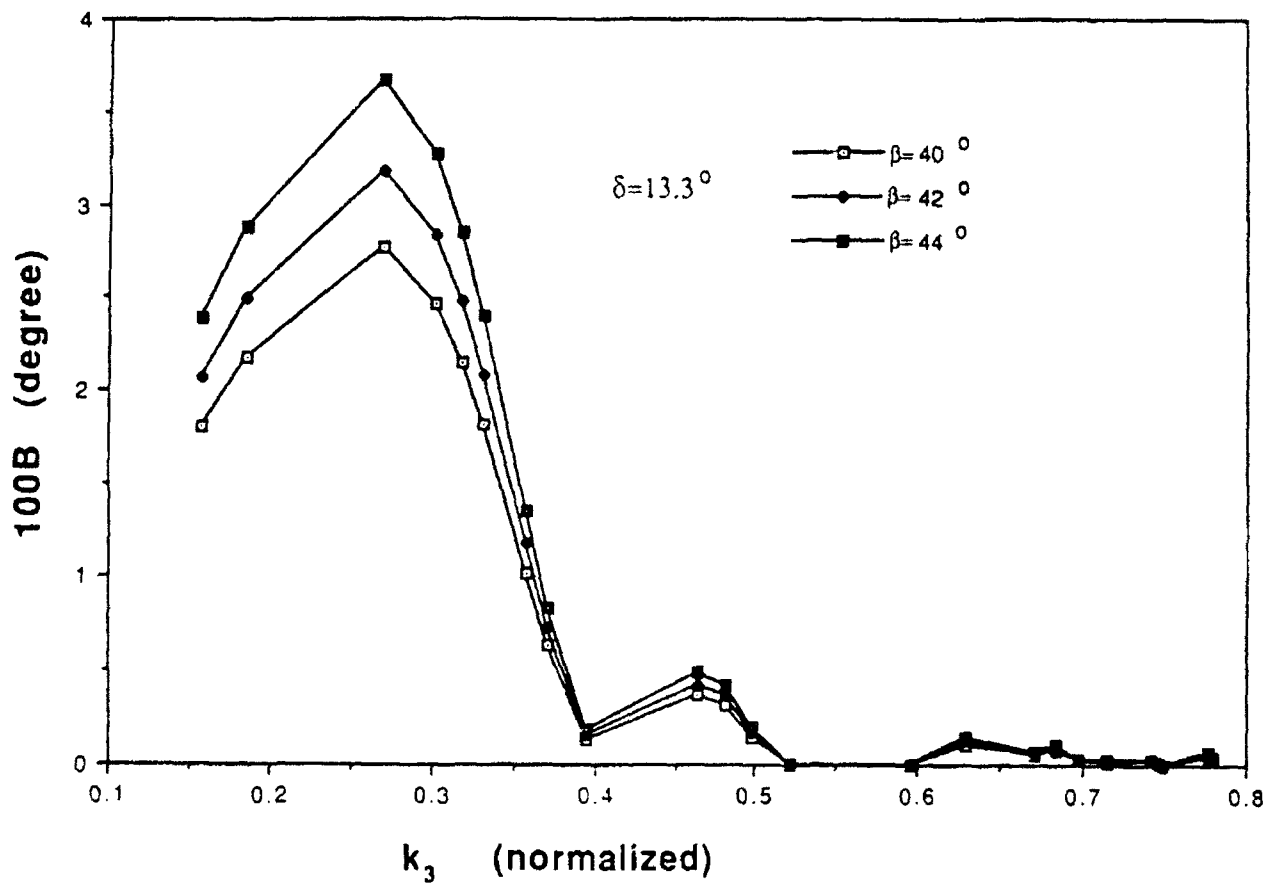


Figure 5.1.4 Index of Blurring Versus the Magnitude of Grating for a Fixed Grating Angle.

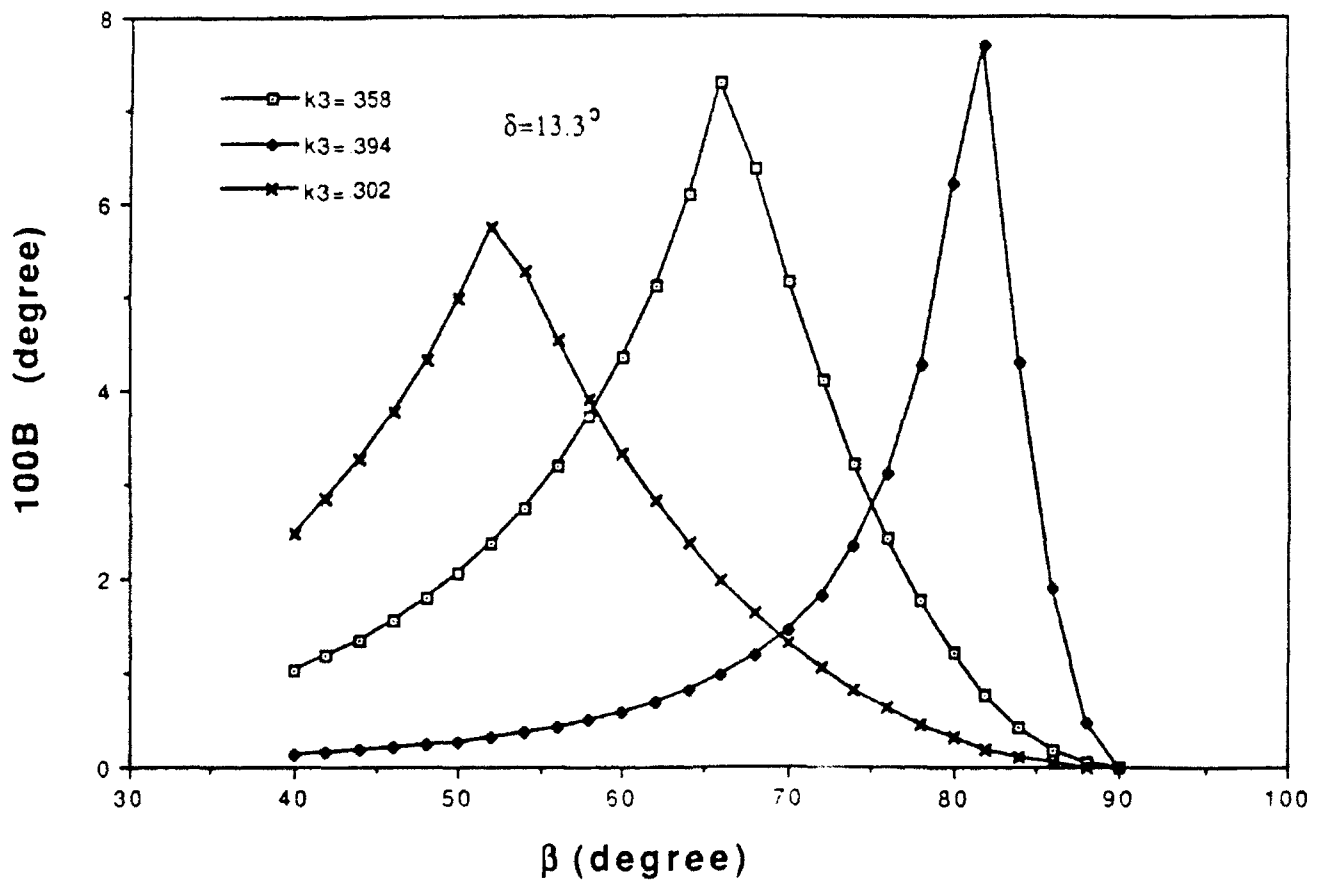


Figure 5.1.5 Index of Blurring Versus the Polarization Inclination Angle for a Fixed Grating Angle.

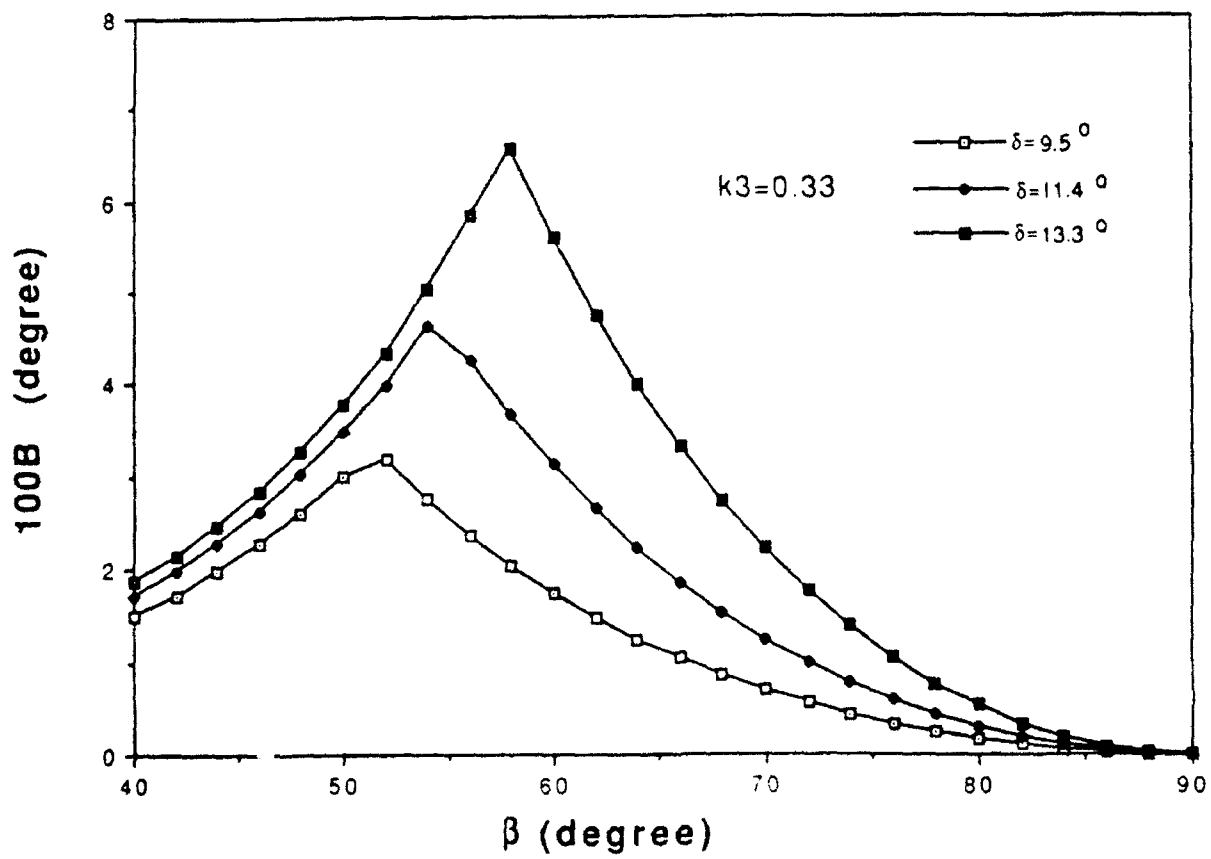


Figure 5.1.6 Index of Blurring versus Polarization Inclination Angle for a Fixed Grating Magnitude.

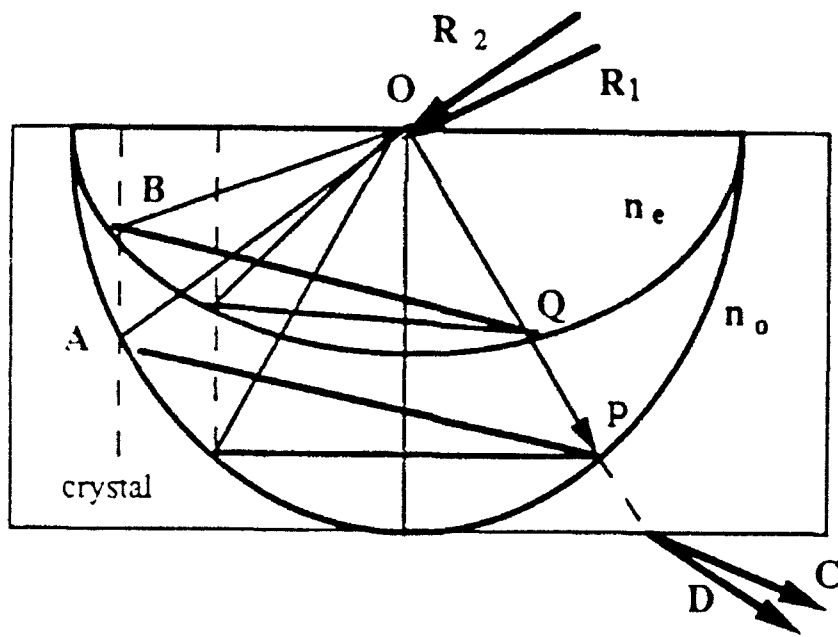


Figure 5.1.7 Optical Coupling 2x2 Switch Wave Vector Configuration.

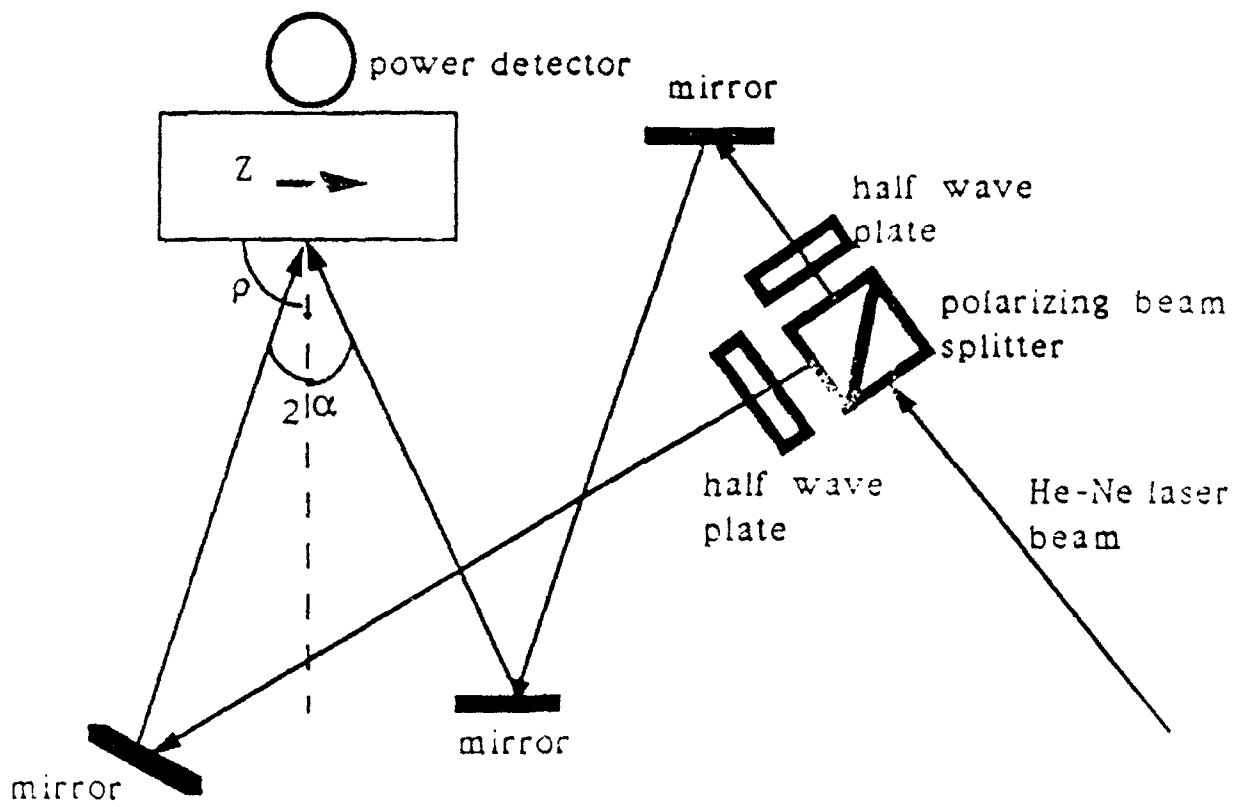


Figure 5.1.8 Experimental Setup for Measuring Diffraction Efficiency Ratio.

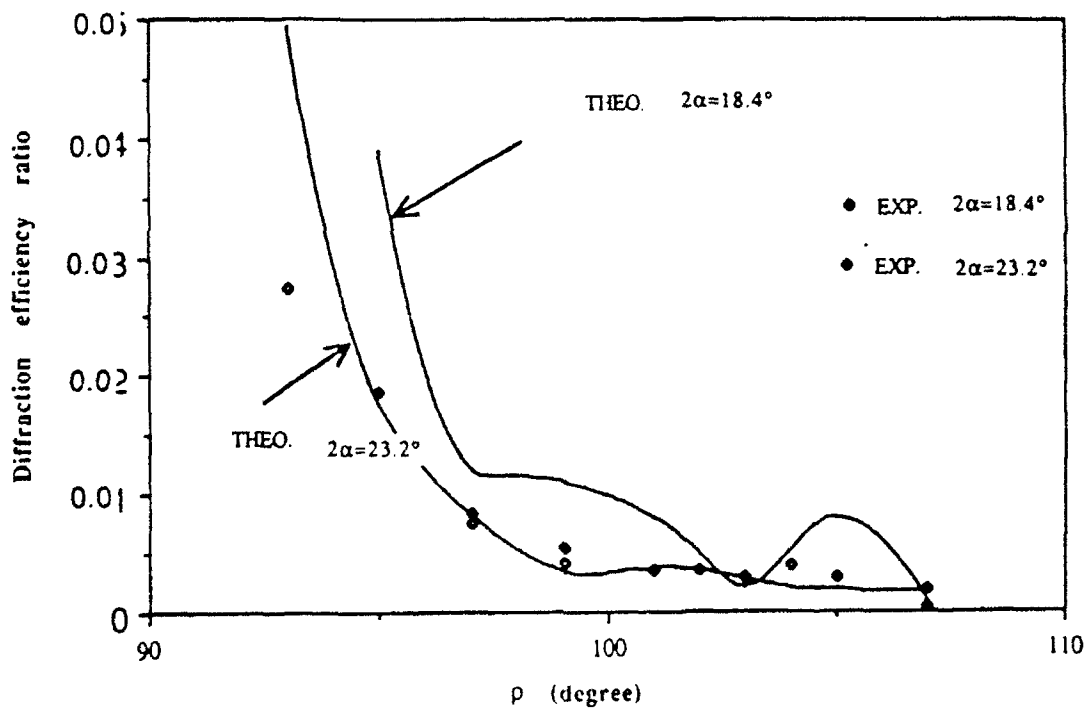


Figure 5.1.9 Diffraction Efficiency Ratio of Vertical Polarization Over Horizontal Polarization. Solid Curves, Theoretical Prediction; Points, Experimental Results.

2 OPTICAL TABLE LOOK UP BASED ON MATRIX VECTOR MULTIPLICATION

The optical table look up is basically a vector(input source and destination header) and matrix (routing table) multiplication process. On a broader sense, Matrix-vector multiplication (MVM) is one of the most basic operations in linear algebra, which has a lot of applications in fields like signal processing and artificial intelligence. Optics is suitable for the MVM because of its inherent advantages of parallelism and high speed. Many works for optical MVM have been reported^{1,2,3}. Most of them use a programmable spatial light modulator (SLM) to display the matrix to be multiplied. However, the slower frame rate and the number of pixels of currently available SLMs limit the capabilities of optical MVM. The limitation is especially severe when the large sized matrix needs to be updated rapidly as required in many applications. In other words, the bottleneck of optical MVM is the speed to input a large 2-D matrix into the optical processor. Photorefractive holograms have high storage density, and pinhole holograms⁴ have the potential for high-speed retrieval programmability. They can be combined to offer great improvement in the capabilities of optical MVM in some of the applications.

In this section, we demonstrate a novel method for performing binary MVM using photorefractive pinhole holograms. The goal is to fast display a required matrix from a pre-fabricated memory system. The matrices are recorded and fixed, as volume holograms, in a LiNbO₃ crystal. The storage density of the crystal provides a large amount of data that can be fast retrieved as page oriented holograms. Therefore, the

technique is suitable for some expert systems, in which only finite numbers (for example, less than 500) of predetermined large sized matrices, which can be the routing table, are needed for MVM.

5.2.1. System Description

In the proposed method, transparent and opaque squares represent the binary values 1 and 0 on the matrix, respectively. The recording process of phase-conjugate reconstruction pinhole hologram is shown in Fig.5.2.1(a). An $M \times N$ matrix, which is to be multiplied by an $N \times 1$ vector in MVM, is illuminated by a plane wave. This spatially modulated wave is then focused by a lens to serve as an input signal beam A. This signal beam A interacts with a reference beam α to form a hologram, which contains the information of the $M \times N$ matrix. The hologram is recorded inside a photorefractive crystal positioned a short distance away from the back focal plane. Therefore, the holograms are not strictly Fourier transform holograms. The reason for this off focus recording is that we can later use a programmable pinhole array on the focal (Fourier) plane to select the matrix to be retrieved.

In reconstruction, a phase-conjugate of the recording reference beam α^* is used to read the stored hologram as shown in Fig.5.2.1(b). The output, which contains the information of the recorded matrix, is a phase conjugate beam of the recording signal beam A*. A pinhole selective mask placed in the focal plane of lens L is used to select this A* which is then inversely transformed by the lens L to reconstruct the previously recorded matrix. The pinhole is used here to block the unwanted light. To multiply this retrieved matrix with an $N \times 1$ vector, the vector mask, having the same size as the

recorded matrix, is inserted into the plane of the reconstructed matrix. Therefore, the light intensity immediately to the left of the vector mask is the overlapping of the matrix and vector. This light distribution is focused by a cylindrical lens to form an $M \times 1$ vector which is the product of the $M \times N$ matrix and the $N \times 1$ vector. An array of optical detectors is put in the focal plane of the cylindrical lens to measure the intensities of the resultant $M \times 1$ vector. The range of the readout intensities is from 0 to N . That is because both $M \times N$ matrix and $N \times 1$ vector are binary.

Now, we describe how a large number of matrices can be stored in and quickly retrieved from the photorefractive crystal. The recording process is depicted by Fig.5.2.2(a). For reference beam α , we record a number of matrices each with a different illumination beam A, B, C and so on. Then we change to reference beam β and repeat the process to record another group of matrices. Therefore, if there are P illumination beams and Q reference beams, a total of $P \times Q$ matrices can be stored permanently in the crystal. Reference 5 detailed a method of recording about 500 high resolution holograms of equal efficiency in LiNbO_3 . After the recording, the holograms can be thermally fixed by heating the crystal to about 160°C , then cooling it down to room temperature and finally illuminating the crystal with incoherent light. Details can be found in Ref. 6. Now the crystal can be viewed as a read-only memory system in which about 500 large sized matrices are stored. The memory can be totally erased by a heating process⁶. In reconstruction, there are Q reading beams available. They can be from a one-dimensional (1-D) laser diode array. Each reading beam is a conjugate of one of the original reference beams. Each of the reading beams reads out P holograms. As shown in Fig.5.2.2(b), α^* ,

for instance, reconstructs P matrices. But a programmable pinhole mask is used to block $P-1$ unwanted reconstructed matrices and let the selected one pass.

The large storage density and high-speed programmability of the method is obvious from the above discussion. The matrices are stored in holograms, which can have very good resolution. As a result, large sized matrices, for example 1000×1000 which corresponds to a $20 \text{ mm} \times 20 \text{ mm}$ window with 50 pl/mm resolution, can be stored. This is an improvement over those spatial light modulator (SLM) based methods, in which the size of the matrix is limited by the number of pixels of the SLM, which is currently in the order of 128×128 . In addition, if 1000 such hologram matrices are stored (see the discussion later), the total storage capacity is the order of 1000^3 bits which is enough for quite a number of applications. The high-speed programmability is because, after the matrices are permanently stored, we just need to open one pinhole on the selective mask and to shine one reading beam to retrieve a required matrix. In practice, the reading beams can be from a one-dimensional laser diode array and the selecting mask is an electrically addressed SLM. It is of course much faster to turn on one pixel and one of the laser diodes to select a matrix than to write a matrix on a two-dimensional SLM. The speed advantage is more obvious when the size of the matrix is very large.

To illustrate the speed advantage of the method, let us assume that the time to turn on each pixel on a 2-D SLM is one nanosecond and to turn on a laser diode on a 1-D laser diode array is also one nanosecond. It takes $M \times N$ nanosecond, which is the time needed to display an $M \times N$ matrix and an input $N \times 1$ vector, for an SLM based MVM. To perform the same MVM using the proposed pinhole hologram method, the time to

display both the matrix and the vector is only N nanosecond, which is the time to display the $N \times 1$ vector. For a $M \times N$ matrix, the speed improvement factor is M . For example for a 1000×1000 matrix the pinhole method offers a speed improvement of three numerical orders.

5.2.2. Experimental Demonstration and Discussion

The experimental setup to demonstrate MVM using phase-conjugate reconstruction pinhole holograms is shown in Fig.5.2.3. The laser used was an Argon laser (Spectra-Physics) at a wavelength of 514.4 nm. The Fe: LiNbO₃ crystal used has dimensions of $10 \times 10 \times 10$ mm³ with the c axis parallel to incident plane. The laser beam from the argon laser was split by a beam splitter (BSP1), into two beams, one used as an illumination beam, the other used as a reference beam. For demonstration of concept and simplicity, the matrix pattern used is a 8×8 matrix made by plastic transparencies and has a size of 1×1 cm². Emerging from BSP1 and reflected by mirror, the reference beam was split into two beams by another beam splitter (BSP2) before going into the crystal. One serving as a writing beam which was blocked in the reconstruction process, the other serving as a reading beam which was blocked in recording process.

In recording, after storing one hologram, we first changed the matrix pattern then rotated the illumination beam to store another hologram with the same reference beam. After a set of matrices had been recorded with a reference beam, we rotated the reference beam to store another set of holograms using the same set of signal beams. In locating the new reference beam position we made sure to avoid the Bragg angle of the previous stored holograms. In our experiment, the measured angular separation between successive

reference beam is about 0.1° and the range of the reference beam is 25° , if 4 pinhole holograms are recorded with each reference beam, $250 \times 4 = 1000$ holograms can be stored.

In reconstruction, the reading beam was the phase conjugate of the writing reference beam. The reconstructed matrix pattern illuminated a vector pattern ($1 \times 1 \text{ cm}^2$ with 8×1 elements) and resulted in a pattern which comprised the matrix vector multiplication. This pattern was imaged onto a camera to take a picture. Then we moved the camera and used a cylindrical lens to converge the matrix pattern to a focused line. The intensity distribution along the line represents the resultant vector of the matrix-vector multiplication. A power meter (Newport 815) was used to measure intensity distribution along the focused line. To demonstrate the feasibility of this method, we made 16 holograms only, formed by 4 signal and 4 reference beams. Figure 5.2.4 shows some of the resulting pictures and plots of MVM. Figure 4(a) is the reconstructed matrices, Fig. 5.2.4(b) is the vector masks, Fig. 5.2.4(c) is the result of Fig. 5.2.4(b) illuminated by Fig. 5.2.4(a), and Fig. 5.2.4(d) is the measured intensity plots of the focused line of Fig. 5.2.4(c), i.e., the result of MVM. In Fig.5.2.4, transparent (bright) and opaque (dark) stripes represent 1 and 0 respectively. For example, the MVM of the first row in Fig. 5.2.4 is

$$\begin{bmatrix} 1 & 1 & 0 & 1 & 1 & 1 & 0 & 0 \\ 1 & 0 & 1 & 1 & 0 & 1 & 1 & 0 \\ 1 & 1 & 0 & 1 & 1 & 1 & 0 & 0 \\ 0 & 1 & 1 & 1 & 1 & 1 & 1 & 0 \\ 1 & 1 & 0 & 1 & 0 & 1 & 1 & 0 \\ 1 & 0 & 0 & 1 & 1 & 1 & 1 & 1 \\ 1 & 1 & 1 & 0 & 1 & 1 & 0 & 1 \\ 1 & 1 & 1 & 1 & 1 & 1 & 1 & 0 \end{bmatrix} \begin{bmatrix} 1 \\ 0 \\ 0 \\ 1 \\ 1 \\ 0 \\ 0 \\ 1 \end{bmatrix} = \begin{bmatrix} 3 \\ 2 \\ 3 \\ 2 \\ 2 \\ 4 \\ 3 \\ 3 \end{bmatrix} \quad (1)$$

The pinhole selective mask used in these experiments is manually operated; however, it can be replaced by a spatial light modulator to become a programmable real time process. The capacity of the proposed method arises from the angular multiplexing method of the reference beam. If for each object illumination beam, five hundred reference illuminations can be achieved as shown in Ref. 5, and for each reference illumination we record four pinhole holograms as demonstrated in our experiment, a total of $P \times Q = 2000$ matrices could be stored by this technique. Assuming the matrices are 1000×1000 in size, which corresponds to $20 \text{ mm} \times 20 \text{ mm}$ window with 50 pl/mm resolution, the system is capable of storing and fast displaying 2×10^9 bits. Therefore, the matrix memory system is capable for a number of expert system applications. Moreover, the proposed method has the capability of simultaneously displaying any combination of holograms recorded with a reference beam by opening the selected pinholes at the same time or even different reference beams by shining more than one reading beam. Consequently, the presented method can also quickly retrieve combinations of the stored matrices for possibly even ternary operations.

5.2.3. Crosstalk Considerations

Since there are several holograms stored with a reference beam, crosstalk exists. It can be remedied by a pre-distortion method, in which the last hologram read out by a reference beam has the highest diffraction efficiency and the first hologram read out by the same reference beam has the lowest efficiency. Therefore, by proper recording exposures, each of the reconstructed holograms from a given reference beam has the same overall light intensity. Thus, crosstalk due to a reference beam losing energy to each hologram is greatly alleviated. Furthermore, for more stringent requirements, crosstalk can be lowered by using a high reference to signal intensity ratio. We note that this type of crosstalk has no significant effect on the MVM because the operation is binary. No obvious crosstalk was observed in our experiment.

Another source of crosstalk is from the finite pinhole size. Since binary matrix has infinite bandwidth, the pinhole has to be large enough to let the main frequency components go through. This will also let the high frequency components of other matrices go through thus causing crosstalk. This crosstalk among the reconstructed (read-out) matrices in the apparatus can be evaluated in a way as follows. The intensity contour $I(x,y)$ of the reconstructed wave field of a certain matrix M_0 in the pinhole plane is the diffraction pattern produced by a square aperture, namely an element cell of the matrix:

$$I(x',y') = \text{sinc}^2(x') \text{sinc}^2(y'), \quad (2)$$

where x' and y' are the normalized coordinates in the pinhole plane. The side lobes of this 2-D contour are centered at

1. on X' axis $x'=\pm(u+\frac{1}{2})\pi$, $y'=0$

with peak values

$$I_{u,0} = \frac{1}{\pi^2} \frac{1}{(u+\frac{1}{2})^2}, \quad (3)$$

2. on Y' axis $x'=0$, $y'=\pm(v+\frac{1}{2})\pi$

with peak values

$$I_{0,v} = \frac{1}{\pi^2} \frac{1}{(v+\frac{1}{2})^2}, \quad (4)$$

3. off-axis $x'=\pm(u+\frac{1}{2})\pi$, $y'=\pm(v+\frac{1}{2})\pi$

with peak values

$$I_{u,v} = \frac{1}{\pi^4} \frac{1}{(u+\frac{1}{2})^2 (v+\frac{1}{2})^2}, \quad (5)$$

where $u, v=0, 1, 2, \dots$. We see that the off-axis terms are two numerical orders smaller than the on-axis terms, and hereforth are neglected. The central spot and side lobes along the X' axis are shown in Fig. 5.2.5.

Let the diameter of the pinhole (or the side length of a square hole) be 4π in the x' scale. This means that the central spot and four first side lobes of the sinc function are allowed to pass through. And let the interval of pinhole positions be 10π as shown in Fig. 5.2.5. We define the energy of a spot or lobe to be its maximum peak value times its area; and a square $\pi \times \pi$ in x' scale to be a unit area. Then, the light energy of M_0 encircled in the pinhole can be estimated as

$$E_0 = 4 + 4 \left(\frac{1}{1.5\pi} \right)^2 = 4.18 \quad (6)$$

of M_0 in the hole should be

$$I_0 = \frac{1}{8} E_0 = 0.5525 \quad (7)$$

At the same time, each of the two nearest axial neighbors of M_0 will contribute its 8th, 9th, 10th and 11th side lobes (which are encircled in the hole $H_1^{(1)}$, see Fig. 5.2.5) to the central area of M_0 . The total energy of the mentioned four side lobes is

$$E_1 = \frac{1}{\pi^2} \left[\left(\frac{1}{8.5} \right)^2 + \left(\frac{1}{9.5} \right)^2 + \left(\frac{1}{10.5} \right)^2 + \left(\frac{1}{11.5} \right)^2 \right]. \quad (8)$$

Since M_0 has a pair of nearest axial neighbors ($H_1^{(1)}$ and $H_2^{(1)}$ in Fig. 5.2.5), the total contribution of these neighbors is $2E_1$, and the average intensity is

$$I_1 = \frac{1}{4} 2E_1 = \frac{1}{2} E_1. \quad (9)$$

Similarly, the contribution to the central spot of M_0 from its two second nearest axial neighbors is

$$\begin{aligned} I_2 &= \frac{1}{2} E_2 \\ &= \frac{1}{2\pi^2} \left[\left(\frac{1}{18.5} \right)^2 + \left(\frac{1}{19.5} \right)^2 + \left(\frac{1}{20.5} \right)^2 + \left(\frac{1}{21.5} \right)^2 \right]. \end{aligned} \quad (10)$$

and so forth. Thus the contribution by all the axially shifted matrices is

$$\begin{aligned}
I &= I_1 + I_2 + \dots \\
&= \frac{1}{2\pi^2} \sum_{k=1}^{\infty} \left[\left(\frac{1}{10k-1.5} \right)^2 + \left(\frac{1}{10k-0.5} \right)^2 + \left(\frac{1}{10k+0.5} \right)^2 + \left(\frac{1}{10k+1.5} \right)^2 \right] \\
&= 0.0034 .
\end{aligned} \tag{11}$$

This value can be taken as the (crosstalk) noise in a statistical meaning; while I_0 in Eq. (7) is the signal. Hence the relative noise or crosstalk level is -24.7dB.

$$\Delta N = \frac{I}{I_0} = 0.006 = 0.6\% . \tag{12}$$

This appears to be a very tolerable number.

Now let us estimate how many hole positions can be averaged in the experiment. Suppose that the diameter of lens L (Fig. 5.2.1) is $D=30$ mm, and its focal length $f=300$ mm; and the wavelength of the light used is $\lambda=0.5 \times 10^{-3}$ mm. Then a normalized length π in the pinhole plane corresponds to

$$\Delta = 0.61 \frac{\lambda f}{D} = 0.003 \text{ mm} . \tag{13}$$

Thus the diameter of the pinhole in mm should be $\delta = 4\Delta = 0.012$ mm, and the distance between the successive hole centers is $d = 10\Delta = 0.03$ mm.

Suppose that the size of the Fe: LiNbO₃ is 10 mm, and the pinhole positions are arranged in a region corresponding to one third of the crystal surface size. Then there are

$$m = \left(\frac{10}{3} \right) / 0.03 = 100 \tag{14}$$

pinhole positions that can be arranged. This is enough for our requirement.

5.2.4. Concluding Remarks on MVM

We have experimentally demonstrated a new pinhole hologram method for performing MVM. Although the preliminary demonstration uses small sized matrix and vector, large sized MVM can be achieved if the detecting electronics is good. Furthermore, this method not only has the advantage of high holographic storage capacity but also shows potential for high-speed programmable, parallel, and real-time binary MVM when finite number of matrices, for instance less than 500, are needed. The experimental implementation of large sized MVM using electrically addressed SLMs to replace the pinhole selecting mask and the input vector is underway.

REFERENCES FOR 5.2

1. P. Yeh and A. E. T. Chiou, *Opt. Lett.* **12**, 138, 1987.
2. J. W. Goodman, A. R. Dias, and L. M. Woody, *Opt. Lett.* **2**, 1, 1978.
3. M. A. Monaharr, K. Bromley, and R. P. Bocker, *Proc. IEEE* **65**, 121, 1977.
4. S. Xu, G. Mendes, S. Hart, and J. C. Dainty, *Opt. Lett.* **14**, 107, 1989.
5. F. H. Mok, M. C. Tackitt, and H. M. Stoll, *Opt. Lett.* **16**, 8, 1991.
6. D. Staebler, W.J. Burke, W. Phillips, J. Amodie, *Appl. Phy. Lett.* **18**, 540, 1971.

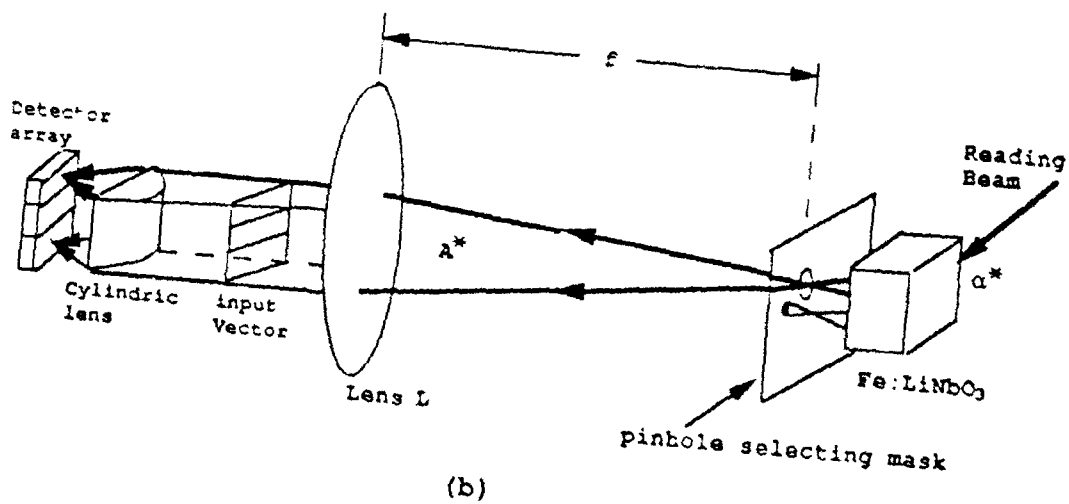
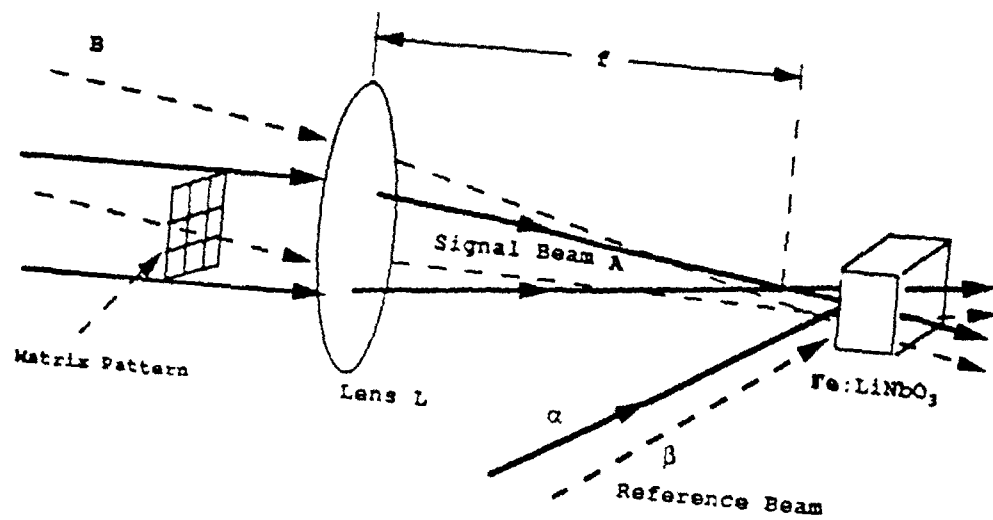


Fig. 5.2.1. Schematic diagram of a pinhole hologram: (a) recording process; (b) Phase-Conjugate reconstruction process.

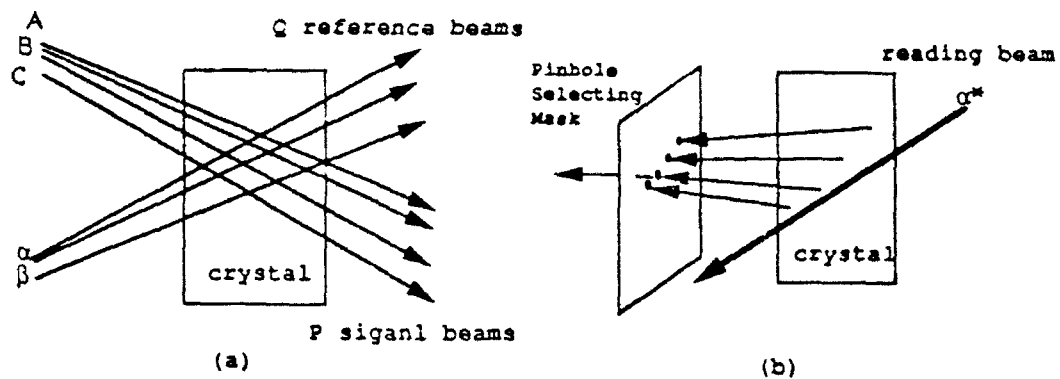


Fig. 5.2.2. The principle diagram of recording and reconstructing multiple pinhole holograms: (a) Recording arrangement in a photorefractive crystal; (b) Using pinhole selective mask to choose the desired reconstructed beam.

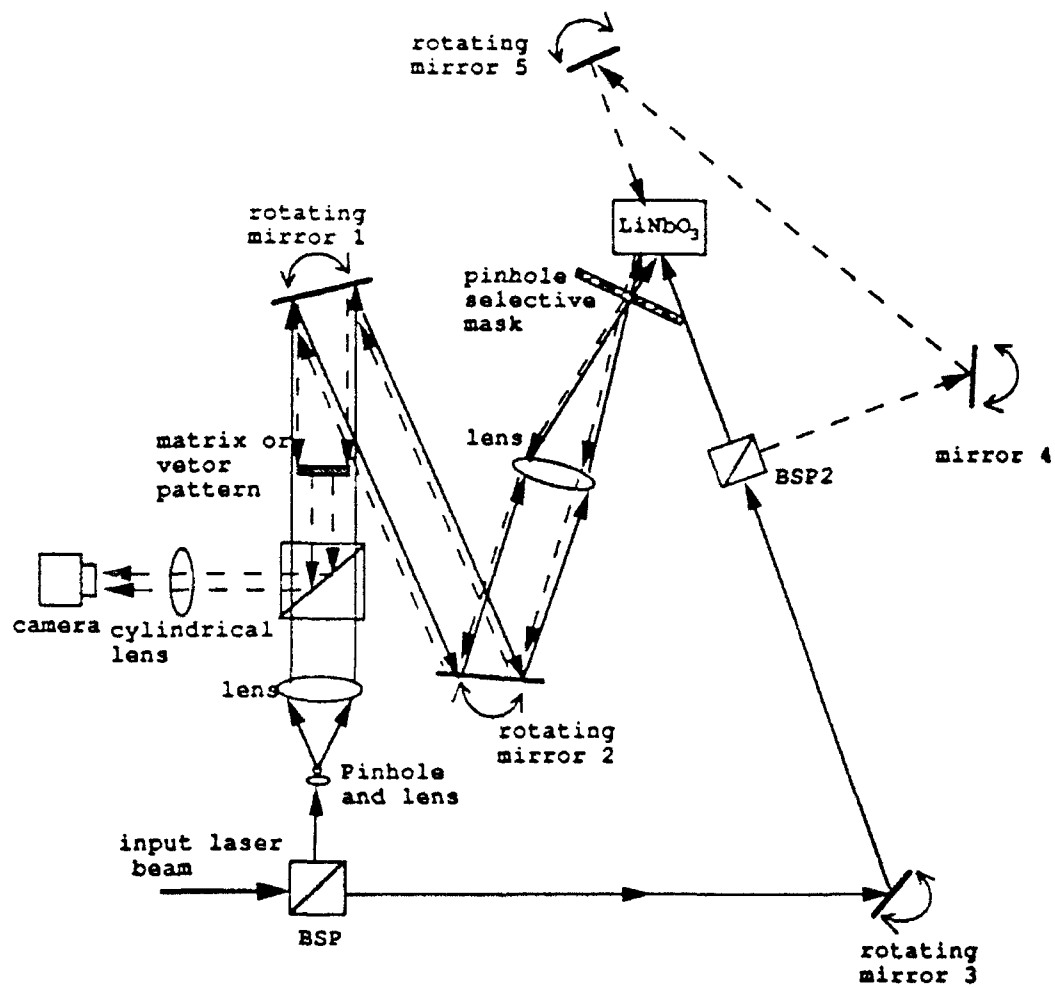


Fig. 5.2.3. Experimental setup of a Phase-Conjugate pinhole hologram: solid lines represent beams in recording process; dash lines represent beams in reconstruction process.

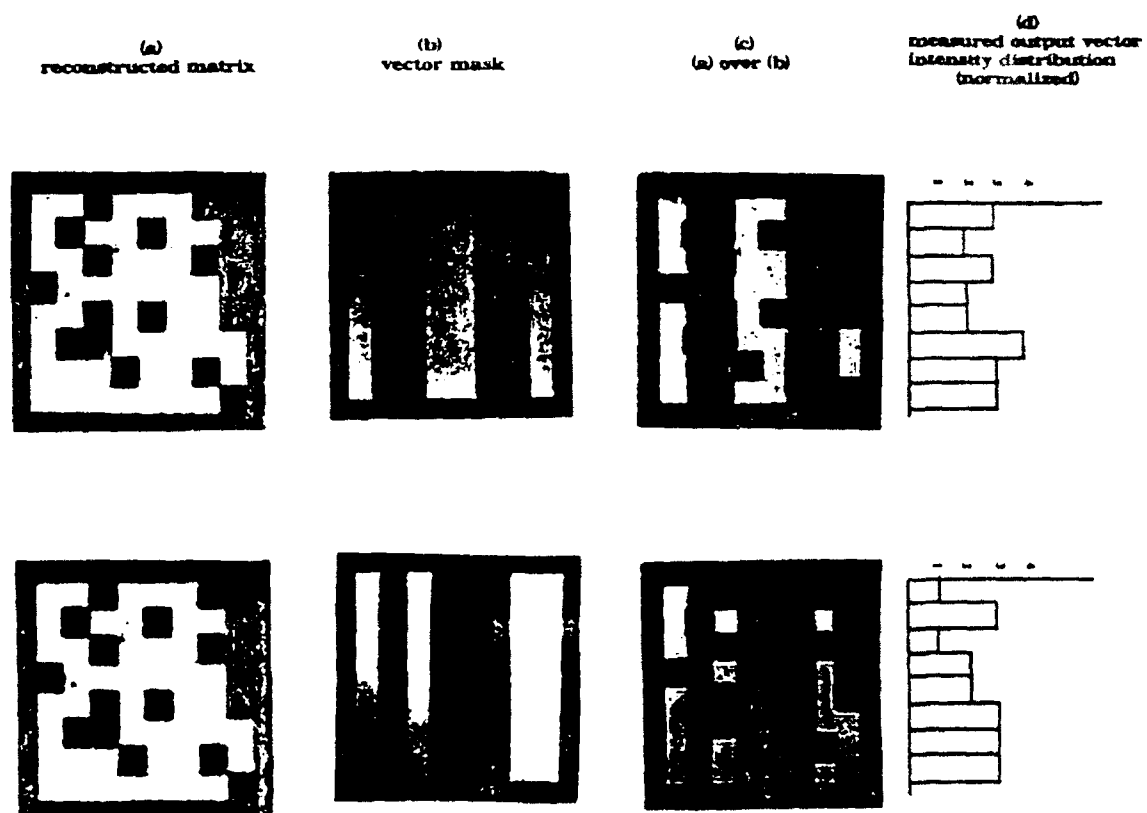


Fig. 5.2.4. Photographs showing the matrix and vector for demonstration MVM: (a) reconstruction matrix; (b) input vector, expanded into a matrix ; (c) result matrix of (b) illuminated by (a); (d) measured intensity plots of (c) focused by a cylindrical lens.

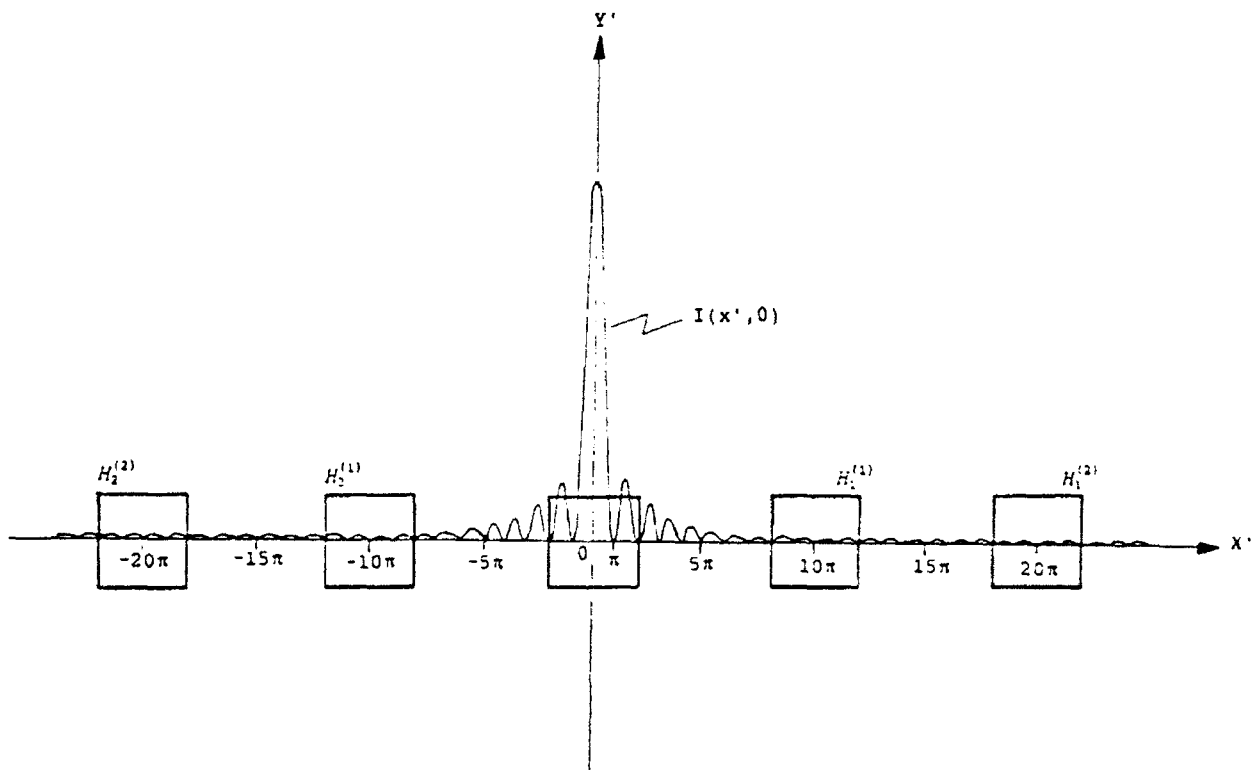


Fig. 5.2.5. Pinhole (drawn in square) size and locations on normalized X' and Y' axis. The intensity of diffraction pattern along X' axis, $I(x', 0)$, is shown schematically.

5.3 NOISE PERFORMANCE OF PHOTOREFRACTIVE HOLOGRAMS

So far in this chapter, we have demonstrated how the photorefractive crystals can be used to implement binary switching and MVM for the proposed OPTIMP. Basically, they are based on the diffraction of the holograms stored in the crystals. When used in a network, these holograms direct or distribute the input light beams to the required destinations. Therefore, the quality of the diffracted beams puts an important limit to the overall performance of the whole system.

In this section, we analyze the temporal and spatial nature of the diffracted light from an ideally recorded photorefractive volume hologram under the influence of electronic noise in the material by using a novel transfer function approach recently derived to study beam propagation through a volume hologram. Because of the noise, the holographic grating within the crystal has random fluctuations in both amplitude and period, which, in turn, is responsible for the degradation in the diffracted light. Since no well established theory on the origin of noise in photorefractive crystal exists, we assume, in this paper, that the noise is essentially thermal when no voltage is applied to the crystal. Our approach can be readily extended to accommodate other sources of noise, e.g., shot noise, or noise from the random space-charge field in photorefractive crystals

3. Gaussian beam illumination at the nominal Bragg angle is assumed so that we can evaluate not only the temporal statistics in the diffracted light, but also its spatial randomness. This quantitative evaluation is achieved by defining a system transfer function which relates the output diffracted light to the input in the spatial frequency

domain. Estimation of spatial randomness is not possible to calculate with plane wave illumination since one cannot monitor transverse fluctuations along its wavefront.

In what follows, we describe the system transfer function of the crystal hologram in Section 5.3.1 and decompose it into a determinate part and a random part, where the latter describes the effect of noise on the output diffracted profile. We then use these transfer functions to compute the output intensity. As shown in Section 5.3.2, the output intensity comprises a coherent part and an incoherent part, the latter resulting from noise in the hologram. The numerical simulation results are presented in Section 5.3.3, and preliminary conclusions are given in Section 5.3.4.

5.3.1. The System Transfer Function of a Hologram

In the analysis of light diffraction from a volume grating, one can relate the spectrum of the diffracted light to that of the incident field via an interaction transfer function. For light nominally incident at the Bragg angle, this transfer function may be derived by Fourier-transforming the paraxial wave equation in the presence of interaction terms. These terms account for the interaction between a diffracted order and the modulation of the refractive index profile. Details can be found in Ref. 4. Conventionally, the transfer function reads

$$H(k_x) = -j \frac{\alpha}{2} e^{jk_x^2 L/2k_0 + jk_x Q \Lambda/4\pi} \text{sinc}[(k_x Q \Lambda/4\pi)^2 + (\alpha/2)^2]^{1/2} \quad (1)$$

where $\text{sinc}(x) \triangleq \sin x/x$ and

Λ = spatial period of the grating,

L = effective thickness of the hologram,

$$Q = 2\pi\lambda L/\Lambda^2,$$

$$\lambda = 2\pi/k_0 = \text{light wavelength in the hologram},$$

$$\alpha = \pi(\Delta n)_m L/\lambda,$$

$(\Delta n)_m$ = peak modulation of the refractive index.

In (1), k_x is a spatial frequency variable. The output (diffracted) light spectrum $\Psi_{\text{out}}(k_x)$ is thus related to the input spectrum $\Psi_{\text{in}}(k_x)$ through the relation

$$\Psi_{\text{out}}(k_x) = H(k_x)\Psi_{\text{in}}(k_x) \quad (2)$$

where

$$\Psi_{\text{in(out)}}(k_x) = F_x\{\Psi_{\text{in(out)}}(x)\} = \int_{-\infty}^{\infty} \Psi_{\text{in(out)}}(x)e^{jk_x x} dx. \quad (3)$$

The first and second exponentials in (1) represent the effects of propagational (Fresnel) diffraction and a spatial shift in the output profile, respectively. If we assume that L is much smaller than the Rayleigh length, the first exponential term can be neglected. Also since we are interested in the spatial fluctuations about the center of the diffracted beam, the second exponential is inconsequential. Hence, instead of (1), we will use the following expression as our starting point:

$$H(k_x) = -j \frac{\alpha}{2} \text{sinc}[(k_x Q \Lambda / 4\pi)^2 + (\alpha/2)^2]^{1/2}. \quad (4)$$

Observe that when $\Psi_{\text{in}}(x)$ is a constant (i.e., a plane wave), Eqs. (2)-(4) readily yield $\Psi_{\text{out}}(x)$ as being proportional to $-j \sin \alpha/2$, in agreement with the results from Chu and Tamir⁵.

To investigate the effect of photorefractive noise for profiled beam illumination,

we first expand (4) assuming $k_x Q \Lambda / 2\pi \alpha \ll 1$. This translates to the requirement that the width of the beam should be much larger than the wavelength, which is true for most practical cases. Eq. (4) then becomes

$$H(k_x) \approx -j \left[\sin \frac{\alpha}{2} + \frac{\alpha}{4} \left(\frac{k_x Q \Lambda}{2\pi \alpha} \right)^2 \cos \frac{\alpha}{2} \right] \left[1 - \frac{1}{2} \left(\frac{k_x Q \Lambda}{2\pi \alpha} \right)^2 \right]. \quad (5)$$

Notice that α really comprises a deterministic part α_0 due to the presence of the light induced holographic grating and a much smaller random part α_R due to electronic noise.

Thus, setting $\alpha = \alpha_0 + \alpha_R$, with $\alpha_R \ll \alpha_0$ in (5), we get

$$H(k_x) = H_D(k_x) + \alpha_R H_R(k_x), \quad (6a)$$

$$H_D(k_x) \approx -j \left[\sin \frac{\alpha_0}{2} + \frac{1}{4\alpha_0} \left(\frac{k_x Q \Lambda}{2\pi} \right)^2 \cos \frac{\alpha_0}{2} - \frac{1}{2\alpha_0^2} \left(\frac{k_x Q \Lambda}{2\pi} \right)^2 \sin \frac{\alpha_0}{2} \right], \quad (6b)$$

$$H_R(k_x) \approx -j \left[\frac{1}{2} \cos \frac{\alpha_0}{2} - \frac{1}{8\alpha_0} \left(\frac{k_x Q \Lambda}{2\pi} \right)^2 \sin \frac{\alpha_0}{2} - \frac{1}{2\alpha_0^2} \left(\frac{k_x Q \Lambda}{2\pi} \right)^2 \cos \frac{\alpha_0}{2} + \frac{1}{\alpha_0^3} \left(\frac{k_x Q \Lambda}{2\pi} \right)^2 \sin \frac{\alpha_0}{2} \right], \quad (6c)$$

where we have neglected all higher order terms in k_x^2 and α_R . Note that in (6), $\alpha_0 = \pi(\Delta n)_m L / \lambda$, which is the value of α when $\alpha_R = 0$. The physical meaning of Eqs. 6(a)-(c) is as follows. Under the influence of noise, the system transfer function is decomposed into two parts. The first part (Eq. 6b) represents the deterministic grating of the hologram. The second part, which is much smaller than the first part because it has a α_R factor, represents the effect of system noise to be added to the output. The first term in $H_R(k_x)$, which is predominant, reminds us that the noise in the grating essentially redirects some

of the undiffracted light in the direction of the diffracted order.

5.3.2. Output Intensities

Our goal in this paper is to find the diffracted light intensities due to the deterministic and random parts of the grating for a given input (Gaussian) profile. To this end, we take the inverse transform of (6a) to write the spatial impulse response as $h(x) = h_D(x) + \alpha_R h_R(x)$, where α_R is, strictly speaking, a random function of x and t with a zero time average due to the nature of electronic noise in the hologram. We can now express the output intensity, by the conventional definition, as

$$\begin{aligned}
 I_{\text{out}}(x) &= \left\langle \int_{-\infty}^{\infty} \int_{-\infty}^{\infty} h(x-x',t) \psi_{\text{in}}(x') h^*(x-x'',t) \psi_{\text{in}}^*(x'') dx' dx'' \right\rangle \\
 &= \int_{-\infty}^{\infty} \int_{-\infty}^{\infty} h_D(x-x') h_D^*(x-x'') \psi_{\text{in}}(x') \psi_{\text{in}}^*(x'') dx' dx'' \\
 &\quad + \int_{-\infty}^{\infty} \int_{-\infty}^{\infty} (\alpha_R(x-x',t) \alpha_R^*(x-x'',t)) h_R(x-x') h_R^*(x-x'') \psi_{\text{in}}(x') \psi_{\text{in}}^*(x'') dx' dx'',
 \end{aligned} \tag{7}$$

where the symbol $\langle \rangle$ denotes time average. The cross terms are zero because α_R has zero time average and $h_D(x)$ is independent of time. The above equation can be further simplified if we take

$$\langle \alpha_R(x',t) \alpha_R^*(x'',t) \rangle = \delta(x' - x'') \beta^2, \tag{8}$$

where β^2 is the temporal mean-squared value of α_R at each point. The physical meaning of Eq. (8) is that at any given time, the noise across the hologram varies in a statistically

independent fashion. Only when the two points x' and x'' overlap, the LHS of Eq. (8) equals the temporal mean squared value of the noise at that point. Now, we can reexpress the output intensity $I_{out}(x)$, as

$$I_{out}(x) = |h_D * \Psi_{in}|^2 + \beta^2 [|h_R|^2 * |\Psi_{in}|^2], \quad (9)$$

where $*$ denotes convolution. Eq. (9) indicates that the deterministic part of the output intensity, which we call the "signal", is spatially coherent, while the random part, which is the noise, is spatially incoherent. The output noise is the convolution of the input intensity and a noise term generated within the system.

To facilitate the calculation of I_{out} , we start from the system transfer functions H_D and H_R . For the coherent part, the Fourier transform of the input field is multiplied with H_D to give the Fourier transform of the output field. The squared magnitude of the inverse transform is the deterministic part of the output diffracted intensity. For the random part, we autocorrelate H_R to find the optical transfer function (OTF) and multiply this with the Fourier transform of the input intensity to eventually find output diffracted intensity due to noise. While the first part is straightforward, one would need some caution in determining the OTF. This is because H_R is a power series expansion in terms of k_x ; thus H_R needs to be truncated for purposes of autocorrelation. This truncation in k_x has to be chosen such that it is well beyond the spectral width of the input Gaussian beam. In our simulation, we chose to truncate H_R at $\pm 10/w$, where w is the spatial width of the input Gaussian.

5.3.3. Figures of Merits and Numerical Simulations

In what follows, we evaluate the noise performance of the system during readout

as a function of various system and input parameters, including temperature, fringe-spacing, and reading beam intensity. Two figures of merit are defined as follows:

(a) the output temporal signal-to-noise ratio (S/N), determined by integrating, over space, the signal and noise profiles, respectively and then taking their ratio. The results are converted into the conventional decibel notation. This serves as an effective indicator of the overall amount of temporal fluctuations in the output;

(b) the spatial fidelity (SF) of the output, determined by finding the time-averaged half power widths of the output intensity profiles without and with noise, w_{without} and w_{with} , respectively. We next calculate $w_{\text{without}} |w_{\text{with}} - w_{\text{without}}|$. This provides us with the information about the average jitter in the width of the diffracted output. Once again we express the result in conventional decibel notation for power, since the power in a Gaussian in one transverse dimension, namely x , is proportional to its width.

To calculate the above two figures of merit, one needs to know β^2 , which represents the mean square value of the fluctuation of α_R and, hence, $(\Delta n)_m$. Now $(\Delta n)_m$ can be related to the peak modulation E_1 of the perturbed electric field in the photorefractive material through the electrooptic coefficient². Thus, β^2 is linearly proportional to the mean square value of the (perturbed) random electric field in the hologram. As stated in the Introduction, we assume, in this paper, that the noise is predominantly thermal in origin. This is because during readout, without external bias voltage, no steady flow of current occurs, and the fluctuations in the random E field are caused mainly by the thermal motion of the charge carriers. Now the stationary white noise power spectrum for the noise voltage is $4k_B TR\Delta f$, where k_B is Boltzmann constant,

T is the temperature, R is the resistance and Δf denotes the temporal bandwidth⁶. Again, $R = \ell/\sigma A$, where σ is the conductivity found using the relation $\sigma = \sigma_0 + \sigma_2 I_0$, with I_0 being the incident intensity and σ_0, σ_2 being constants⁷. The constant A is the cross-sectional area perpendicular to the holographic grating. We take ℓ to be equal to the grating period Λ . Also, we assume that Δf is approximately the reciprocal of the recombination time $\tau_r = (\gamma_r N_D)^{-1}$, where γ_r is the carrier recombination rate and N_D is the donor concentration of the material.

In what follows, we plot (S/N) as a function of input beam intensity, temperature and fringe spacing at the beginning of the readout process. All the material parameters for BSO, for which we plot the results, have been taken from Ref. 2. We also take, from Ref. 7, $A = 1\text{cm}^2$, $\sigma_0 = 1.6 \times 10^{-13} \Omega^{-1} \text{m}^{-1}$; $\sigma_2 = 7.3 \times 10^{-10} \Omega^{-1} \text{m/W}$. The width w of the input Gaussian beam is 3 mm.

Figure 5.3.1 shows the signal to noise ratio (S/N) as a function of reading light intensity, with temperature as a parameter, $K_x = 2\pi/\Lambda = 1.5 \times 10^6/\text{m}$, and $\alpha_0 = 4.2$. The S/N is defined as $S/N = 10 \log$ (signal power/noise power) where

$$\text{signal power} = \int_{-\infty}^{\infty} |h_D * \psi_{in}|^2 dx \quad (10a)$$

$$\text{noise power} = \beta^2 \int_{-\infty}^{\infty} [|h_R|^2 * |\psi_{in}|^2] dx. \quad (10b)$$

As the reading light intensity increases, the relative influence of the noise decreases, thus the S/N increases. For the same reason, with a fixed reading intensity, the S/N improves as the temperature decreases.

Figure 5.3.2 depicts the S/N as a function of temperature, with reading intensity as a parameter, and with $K_x = 1.5 \times 10^6/\text{m}$, and $\alpha_o = 4.2$. One can find the same relationship and physical explanation as that of Fig. 5.3.1. The influence of noise is apparent in this figure. As the temperature rises, the S/N dramatically degrades. At room temperature, the S/N is about 49 dB.

Figure 5.3.3 describes the S/N as a function of the wave vector of the hologram, with reading light intensity as a parameter, and with temperature = 500°K and $\alpha_o = 4.2$. As the value of wave vector becomes larger (denser fringes) and reading light weaker, the relative random fluctuation of refractive index due to noise becomes more significant. Thus the S/N degrades.

We have also simulated the spatial fidelity (SF) of the output for the same variables and parameters as in the above three cases. The results are almost identical to the above figures, respectively. The reason for this close similarity is because of our definition of SF and energy conservation. When the SNR is high, most of the input light will be diffracted by the deterministic grating. Therefore, $|w_{\text{with}} - w_{\text{without}}|$ will be small. As a result, $w_{\text{with}}/|w_{\text{with}} - w_{\text{without}}|$ will be large. Thus the SNR and SF are correlated. In other words, when SNR is high, so is the SF, and hence the average jitter in the width of the diffracted light is small.

5.3.4 Conclusions on Photorefractive Noise

A preliminary study on the noise performance of photorefractive holograms under Gaussian beam illumination is presented. Generally speaking, for stronger reading intensity, lower temperature, and larger fringe spacing, the better the noise performance.

The study will provide guidance for potential applications in interconnections and in optical computing/signal processing. The study of noise performance with other sources of noise, viz., the random space-charge field, using the transfer function approach, and the experimental verification of the concepts developed are currently under way.

REFERENCES FOR 5.3

- [1] See for example: Special issue on "Photorefractive Materials, Effects, and Devices," J. Opt. Soc. Amer., vol.B7, pp.2245-2392, 1990.
- [2] P.P. Banerjee, Q.W. Song and J.J. Liu, "Perturbation Analysis of Transient Diffraction Efficiency of Photorefractive Materials," Optics Comm., vol.83, pp.195-202, 1991.
- [3] C. Gu and P. Yeh, "Scattering Due to Randomly Distributed Charge Particles in Photorefractive Crystals," Opt.Lett., vol.16, pp.1572-1574, 1991.
- [4] P.P. Banerjee and C.W. Tarn, "A Fourier-Transform Approach to Acoustoptic Interaction in the Presence of Propagational Diffraction," Acustica, vol.74, pp.181-191, 1991.
- [5] R-S. Chu, and T. Tamir, "Diffraction of Gaussian Beams by Periodically Modulated Media for Incidence Close to a Bragg Angle," J. Opt. Soc. Amer., vol.66, pp.1438-1440, 1976.
- [6] A. Yariv, *Optical Electronics*, 4th Ed., Holt, Rinehart and Winston: Philadelphia, 1991.
- [7] J.P. Huignard and F. Micheron, "High-Sensitivity Read-Write Volume Holographic Storage in $\text{Bi}_{12}\text{SiO}_{20}$ and $\text{Bi}_{12}\text{GeO}_{20}$ Crystal," Appl. Phys. Lett., vol.29, pp.591-593, 1976.

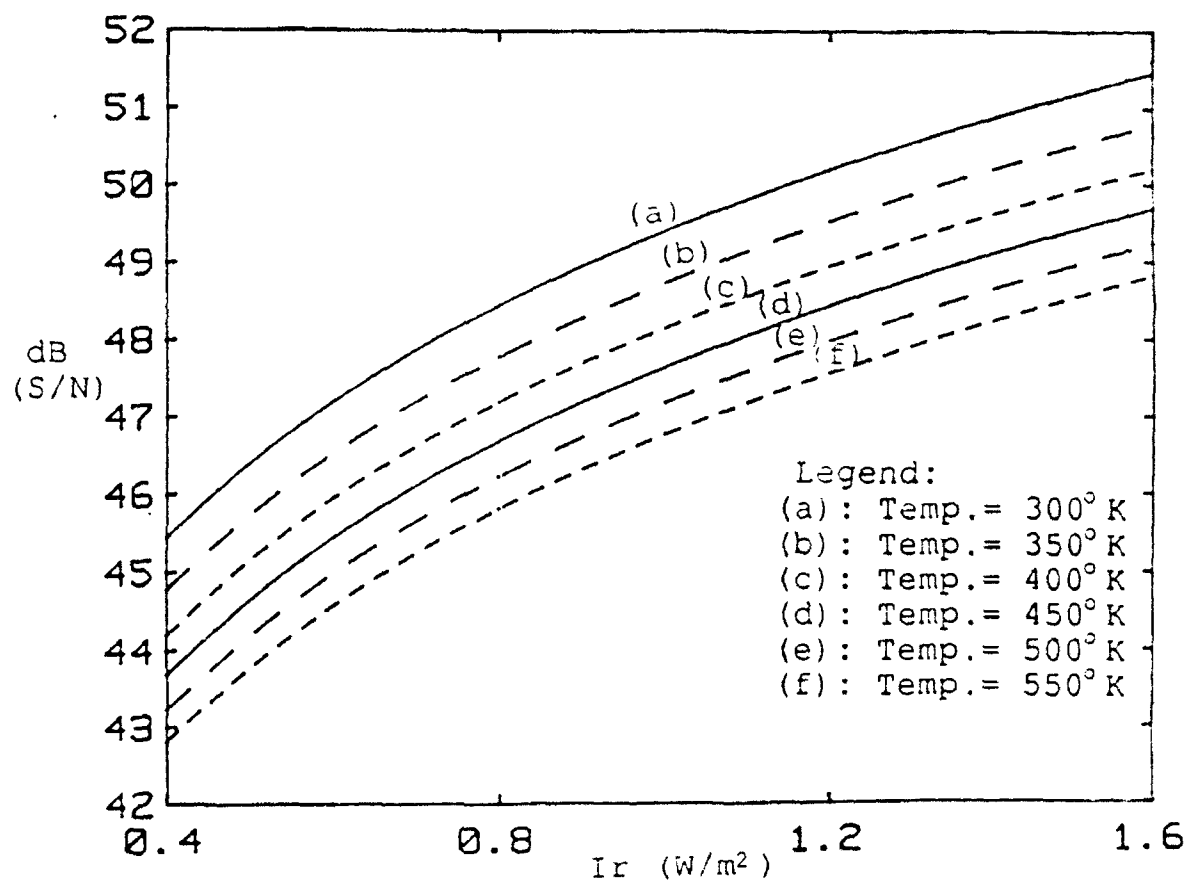


Fig. 5.3.1. Temporal S/N as a function of reading light intensity. $K_x = 1.5 \times 10^6 \text{m}$, $\alpha_0 = 4.2$.

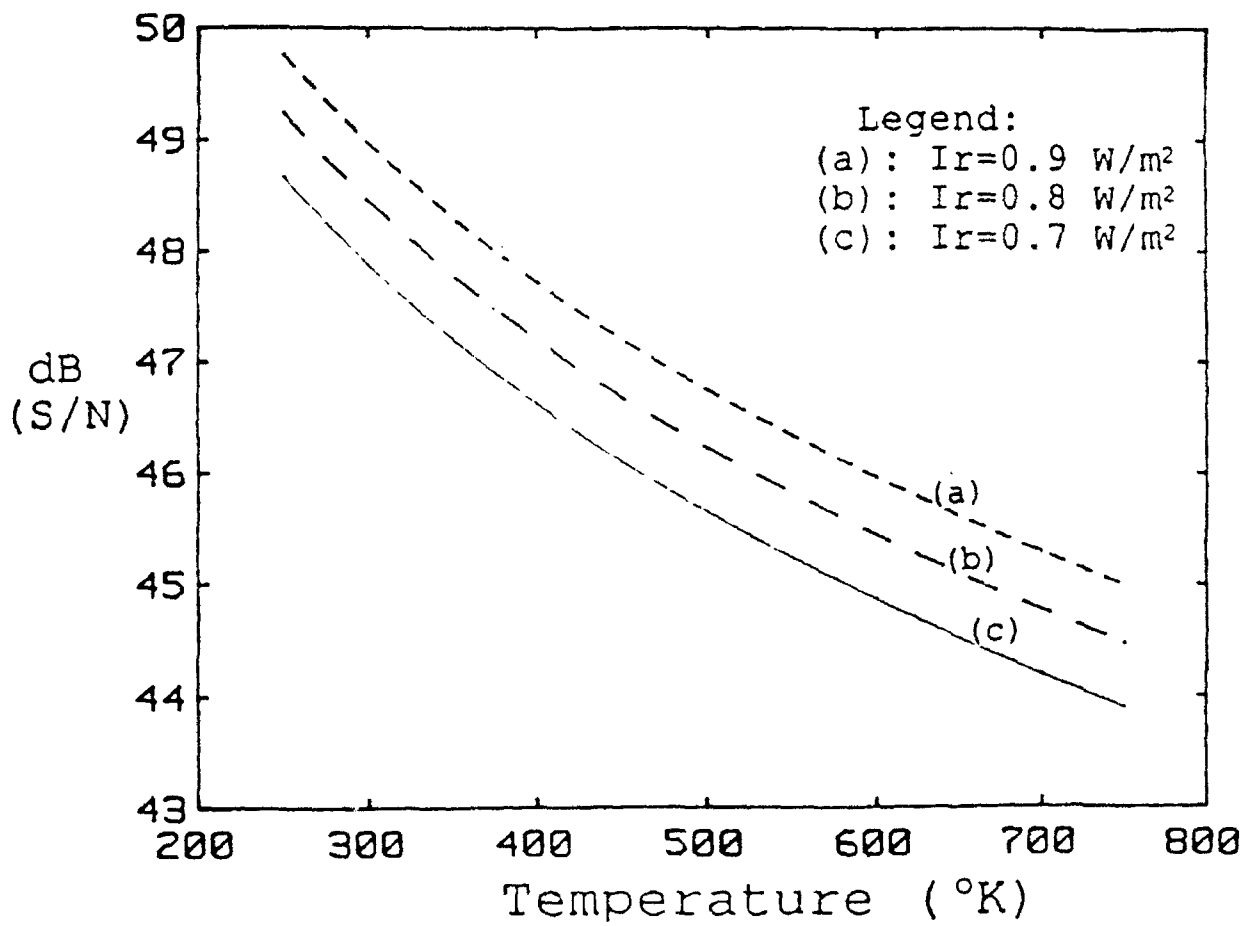


Fig. 5.3.2. Temporal S/N as a function of temperature. $K_x = 1.5 \times 10^6/\text{m}$, $\alpha_o = 4.2$.

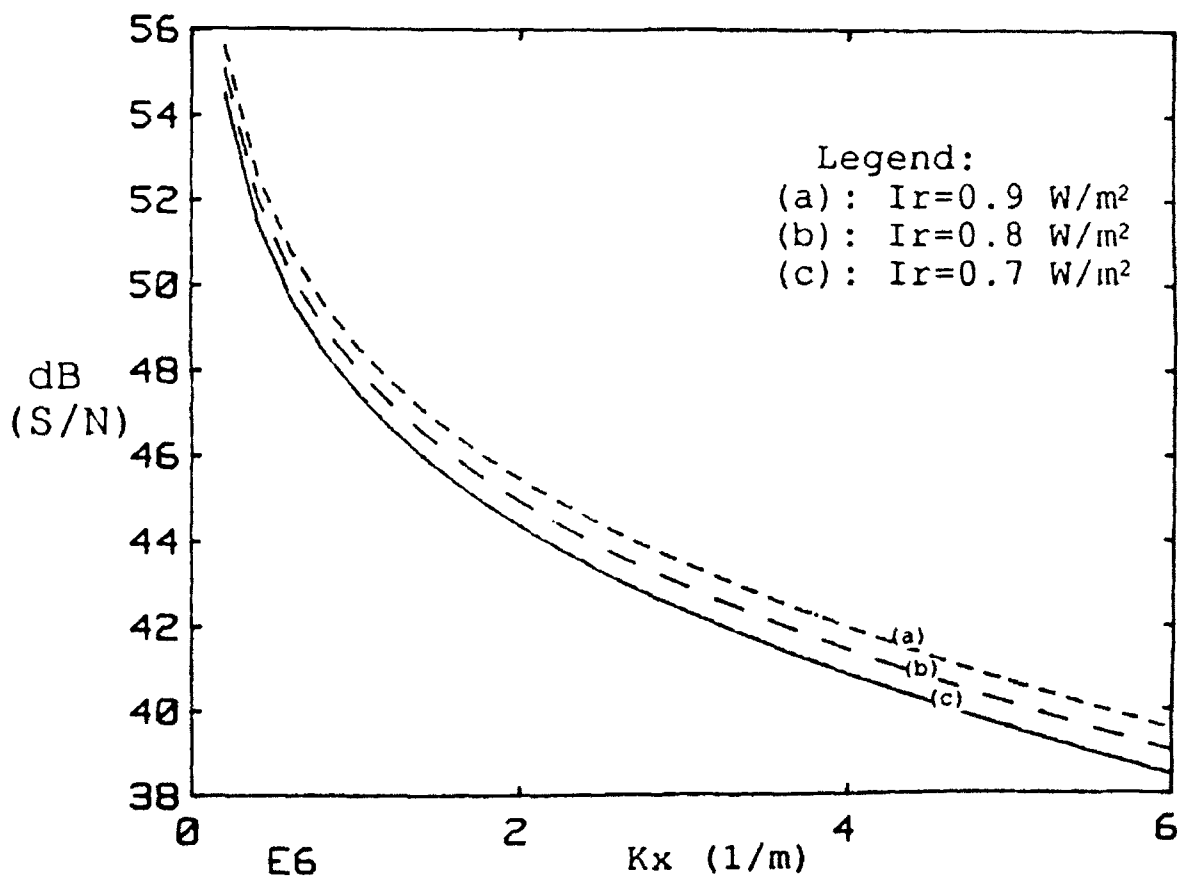


Fig. 5.3.3. Temporal S/N as a function of the wave vector of the hologram. $T = 500^\circ\text{K}$, $\alpha_0 = 4.2$.

6. CONCLUSIONS

All-optical high performance interconnection networks would greatly increase the capabilities of modern communications and parallel computing. The bottleneck of the current optical fiber networks is the slow speed and low bandwidth of the switching electronics which switch and route the data at each node in the network. In addition, the electrical to optical and optical to electrical conversions at these nodes also introduce the conversion errors together with the low efficiency and complexity of the network.

The purpose of this project is to design and analyze a novel optical interface message processor (OPTIMP) that can alleviate the above mentioned bottlenecks. The OPTIMP exploits the inherent advantages of optics to offer high bandwidth and parallelism in routing and switching in a fixed-length packet switching environment. There are four tasks in this project. They are (1) survey of the relevant optical devices; (2) survey of relevant communication networks; (3) design and analysis of an optical interface message processor; (4) experimental demonstration of some of the optical functional modules to be used in the OPTIMP. All the tasks are successfully completed.

The original contribution of this research is the development of a novel optical interface message processor. It explores the high-bandwidth, parallelism, and two-dimensional processing capabilities offered by optics. The most time consuming operations in communication networks such as source-destination table search and data switching are implemented in optical domain. In particular, the table search is achieved by a simple truth-table look up that greatly simplifies the complicated computation process. The switching network is an optically controlled SEED array that can be quickly

reconfigured by the optical output pattern of the table look up processor. As a result, the design does not suffer from the optical to electrical and electrical to optical conversion bottleneck and can perform data routing and switching in the range of Gigabits/sec. Our preliminary analysis and computer simulation proved this.

In addition, The use of photorefractive crystal for optical switching in the OPTIMP is considered. To be specific, we demonstrated how the polarization sensitivity of birefringent photorefractive volume holograms can be used for binary switching. The two-by-two switching unit demonstrated here can be a basic building block for quite a number of complicated switching networks. The advantage of the method is its architectural simplicity, massive parallelism, theoretical cascadability and energy efficiency.

A novel pinhole hologram-based matrix-vector multiplication system that can be used for the truth table look up in OPTIMP is also demonstrated. All the contents of the routing table are stored as pinhole holograms in the crystal. Each table (matrix) corresponds to a pinhole hologram. The unique property of this technique is its fast update capability for reconfiguration of the routing table.

The noise performance of the photorefractive holograms is studied using the Kuktarev equations. The signal-to-noise ratio and distortion index as a function of temperature, spatial frequency, and read out light intensity are investigated. The result may offer some general guidance for the applications of the photorefractive holograms.

To conclude the report, it is worthwhile pointing out that we have demonstrated a novel design of optical interface message processor that can improve the current optical communication network. Unfortunately, the key device, SEED, is not available within the

budget to experimentally demonstrate the prototype of OPTIMP. As the material and device development of SEED progresses, the technique described in the report may lead to high performance optical communication networks in modern communication and parallel computing.

**MISSION
OF
ROME LABORATORY**

Rome Laboratory plans and executes an interdisciplinary program in research, development, test, and technology transition in support of Air Force Command, Control, Communications and Intelligence (C³I) activities for all Air Force platforms. It also executes selected acquisition programs in several areas of expertise. Technical and engineering support within areas of competence is provided to ESD Program Offices (POs) and other ESD elements to perform effective acquisition of C³I systems. In addition, Rome Laboratory's technology supports other AFSC Product Divisions, the Air Force user community, and other DOD and non-DOD agencies. Rome Laboratory maintains technical competence and research programs in areas including, but not limited to, communications, command and control, battle management, intelligence information processing, computational sciences and software producibility, wide area surveillance/sensors, signal processing, solid state sciences, photonics, electromagnetic technology, superconductivity, and electronic reliability/maintainability and testability.